

CZECH TECHNICAL UNIVERSITY IN PRAGUE
Faculty of Electrical Engineering

ONDREJ KRIVOSUDSKÝ ~ *Doctoral Thesis*

January 2019

THE CZECH ACADEMY OF SCIENCES
Institute of Photonics and Electronics ~ Bioelectrodynamics

CZECH TECHNICAL UNIVERSITY IN PRAGUE
Faculty of Electrical Engineering ~ Department of Electromagnetic Field



RADIOFREQUENCY AND MICROWAVE PROPERTIES OF PROTEIN STRUCTURES

Doctoral Thesis

ONDREJ KRIVOSUDSKÝ

Prague, January 2019

*Ph.D. Programme: Electrical Engineering and Information Technology
Branch of Study: Radioelectronics*

*Supervisor: Ing. Michal Cifra, Ph.D.
Supervisor specialist: Prof. Ing. Jan Vrba, CSc.*



Research papers presented in this thesis are protected by copyrights listed below. They are presented and reprinted in accordance with the copyright agreements with the respective publishers. Further copying or reprinting can be done exclusively with the permission of the respective publishers.

- © 2014-2019 Ondrej Krivosudský *All rights reserved.*
- © 2016, 2017 IOP Publishing *All rights reserved.*
- © 2018 Elsevier B.V. *All rights reserved.*
- © 2012 Brett L. Mellor *All Rights Reserved*

CONTENTS

Declaration of originality	iii
Acknowledgements	iv
Abstract	v
1 INTRODUCTION	1
2 STATE OF THE ART	3
2.1 Microtubules – natural nanostructures	3
2.2 Dielectric spectroscopy – proteins	5
3 GOALS OF THE THESIS	9
4 MICROWAVE ABSORPTION BY NANORESONATOR VIBRATIONS TUNED WITH SURFACE MODIFICATION	11
5 RESOLVING CONTROVERSY OF UNUSUALLY HIGH REFRACTIVE INDEX OF TUBULIN	19
6 ON-CHIP MICROWAVE SENSING OF TUBULIN AND ITS POLYMER	25
7 RESULTS	47
8 CONCLUSIONS	49
8.1 Contribution of the dissertation	49
8.2 Future directions	49
BIBLIOGRAPHY	50
LIST OF AUTHOR’S PUBLICATIONS RELATED TO THE DOCTORAL THESIS	57
APPENDIX	59
A RATIONAL DESIGN OF SENSOR FOR BROADBAND DIELECTRIC SPECTROSCOPY OF BIOMOLECULES	61
B SUPPLEMENTARY DATA OF SECTION 4	71
C SUPPLEMENTARY DATA OF SECTION 5	79
D SUPPLEMENTARY DATA OF SECTION 6	85
E SUPPLEMENTARY DATA OF ARTICLE [A4]	95
CURRICULUM VITAE	108

DECLARATION OF ORIGINALITY

I, the undersigned, hereby declare that this doctoral thesis is the result of my research in our research team and my contribution corresponds to that specified at the beginning of each research chapter. The thesis was written under the professional supervision of Dr. Michal Cifra and Dr. Daniel Havelka, using the literature and resources listed in the Bibliography and References.

In Prague, 28. January 2019

.....

ING. ONDREJ KRIVOSUDSKÝ

ACKNOWLEDGEMENTS

Special thanks to:

Dr. Michal Cifra, Dr. Daniel Havelka, Dr. Ondřej Kučera, Dr. Djamel Eddine Chafai, and other colleagues from the Institute of Photonics and Electronics of the Czech Academy of Sciences.

Dr. Vratislav Sokol, Dr. Milan Přihoda, and Dr. Jan Eichler from CST GmbH company.

Dr. Martin Kempa, Doc. Viktor Bovtun, and other colleagues from the Institute of Physics of the Czech Academy of Sciences.

Deepest thanks to:

My mother, father and also my girlfriend Ivana.

Research presented in this thesis was supported by:

Grant No. GA15-17102S, Czech Science Foundation - GACR, 2015-2017.

Grant No. GA17-11898S, Czech Science Foundation - GACR, 2017-2019.

Grant No. GA18-23597S, Czech Science Foundation - GACR, 2018-2020.

ABSTRACT

MOTIVATION

Electromagnetic characterization of biomolecular nanostructures is providing deeper understanding of the interaction of electromagnetic waves with polar and structurally complex biological matter. It is also opening a new way for possible probing of these structures by electromagnetic field, to enhance or change their function and to explore novel paths to future electrodynamic and electronic therapeutic and diagnostic methods in biotechnology and medicine.

AIM

The study had ambitions to (i) develop a model describing the electromagnetic field coupling to "biological-like" nanostructures, (ii) design and develop appropriate tools for investigation of biomolecules, and (iii) apply these tools to evaluate the dielectric response of tubulin and microtubule solution in the broad frequency range.

METHODS

The presented results of electromagnetic and biophysical properties of biomolecules are based on (i) theoretical modeling of nanostructures and their interaction with electromagnetic radiation, (ii) measuring and calculation of the high-frequency dielectric response of tubulin and microtubule, and (iii) investigation of the broadband dielectric response of tubulin and microtubule solution.

RESULTS AND CONCLUSIONS

The coupling of the external electromagnetic field to vibrations of nanobjects is significant only when vibrations are sufficiently underdamped. The high-frequency permittivity i.e. refractive index together with polarizability of tubulin was obtained from experimental results and calculated from theory. The dielectric response of tubulin polymerization was evaluated in broadband frequency range.

KEYWORDS

dielectric spectroscopy, protein, microtubule, electromagnetic field;

Forces and geometry determine the structure and govern a function. This fundamental principle can be applied to every biological nanostructure; molecule, amino acid or protein. Knowledge of the pertinent forces and their effects is therefore essential to fully understand their properties and behaviour.

Structure and all overall geometry of a protein can be obtained by multiple techniques such as Cryo-electron microscopy. It is allowing the observation of biological specimens in their native environment with unprecedented near-atomic resolution [1]. However, to obtain and understand also the forces and a function of biomolecules, knowledge of their static structure alone is insufficient. Dynamic behavior plays an important role, therefore it is attracting the attention of scientific community for several decades [2–5]. One of the very useful methods of probing the dynamic behavior of biomolecules in their native state is dielectric spectroscopy.

The dielectric spectroscopy enables to understand the biomolecular structure and its interactions through a broad variety of time-scales. It also provides a deeper understanding of electromagnetic properties of biomolecular nanostructures in their natural environment which determines the interaction of electromagnetic waves with polar and structurally complex biological matter. Such a piece of knowledge has a potential to boost research in several other fields of science and technology, including biophysics or high-frequency bioelectronics.

It is also opening a new way for possible probing of these structures by an electromagnetic field, to enhance or change their function and to explore novel paths to future electrodynamic and electronic therapeutic and diagnostic methods in biotechnology and medicine. However, due to their complexity, small dimensions (micro- to nano-size) and sophisticated dynamic behavior, characterization of these structure under their natural conditions is still a challenging task.

In this thesis, we focused mainly on the tubulin protein. There are numerous reasons for choosing it. Tubulin, or microtubule in its polymerized form, is the pillar of cellular cytoskeleton. One of the microtubule roles given by nature is to provide mechanical support of a cell [6] and participate in the molecular transport of crucial cell cargo [7]. The microtubule itself also possesses a unique ability of self-assembly and self-repairing [8,9] together with extraordinary electric properties [10, 11].

The microtubule also serves as a main target in cancer treatment and as a target of many post-translational modifications [12, 13].

Based on the arguments above, we firmly believe that obtaining the electromagnetic properties of such structures plays an important role.

The thesis is divided into several parts starting with *State of the art*. In the first Subsection 2.1 we briefly discuss the biological nature of microtubule. The Subsection 2.1 also contains some historical overview of the pioneering experiments which were mainly focused on the investigation of microtubule unusual electric properties. The dielectric spectroscopy and application, on biomolecules with a strong focus on proteins, is discussed in the following Subsection 2.2. The core of the work is then divided to the subsequent three sections. In Section 4 *Microwave absorption by nanoresonator vibrations tuned with surface modification* we provide a rigorous theoretical treatment of the interaction of the "nano-rod" like structures with surrounding medium and the possible effects on the vibrations as consequent interaction with the electromagnetic field. Section 5, *Resolving controversy of the unusually high refractive index of tubulin* is devoted to the measurement and calculation of the refractive index (and high-frequency permittivity) of tubulin and microtubule.

The last part of the thesis is then committed to the development of the microwave sensor which was used to probe the dielectric properties of the tubulin and microtubule solutions, see Section 6.

The thesis also includes the article devoted to sensor design for probing the broadband frequency range of biomolecules. Our initial intention was to provide the reader with a tool and manual how to approach to microwave sensor design from the bottom up approach. We verified all design steps starting from theoretical analysis, our manufacturing capabilities, the frequency of interest, sample volume etc. Our sensor was tested to measure the dielectric spectra of alanine biomolecule, see Appendix A. The approach and analysis we developed were later used to different design in previously mentioned Section 6.

List conclusion with a list of author's publications is placed at the end of the thesis. As appendix I also enclose the supplementary material to Sections 4, 5, and 6.

2.1 MICROTUBULES – NATURAL NANOSTRUCTURES

Microtubules, self-assembling and self-repairing protein nanostructures creating physical pillars for cell interior, are present in almost all eukaryotic cells [9]. They are involved as the main performer in crucial biological cell functions like division, transport of cellular components, and cell motility. Microtubule itself is constructed from numerous $\alpha\beta$ -tubulin dimers in "rod-like" shape with an approximate outer diameter of about 25 nm and the inner diameter about 17 nm, see Fig. 2.1. The whole structure is mostly composed of 13 protofilaments,

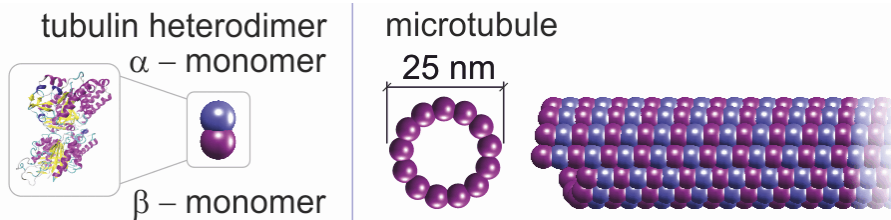


Figure 2.1: Left part: Tubulin heterodimer consist of α - and β -monomer. Right part: A cross-section of a microtubule and schematic depiction of a microtubule

which are creating the microtubule body. For certain highly specialized complexes, as for example neurons, they can be built from 11 to 15 protofilaments [14](p.974). Given by the composition of an amino acid chain and structure of $\alpha\beta$ -tubulin, microtubules posses several interesting properties. Most prevailed is electric property connected with tubulin. Tubulin itself has a high total static dipole moment of about 1,714 D [16]. This value, in comparison with other proteins, seems to be quite exceptional [15], see details in Fig. 2.2.

The electric properties of microtubules caught the attention of the scientific community already 30 years ago. One of the pioneering works which showed unusual properties of microtubule nanostructures was done by Vassilev *et al.* [17]. Their findings of microtubules alignment in the presence of electric and magnetic field suggested for the first time a possible role of microtubules in the biological effects of exo- and endogenous

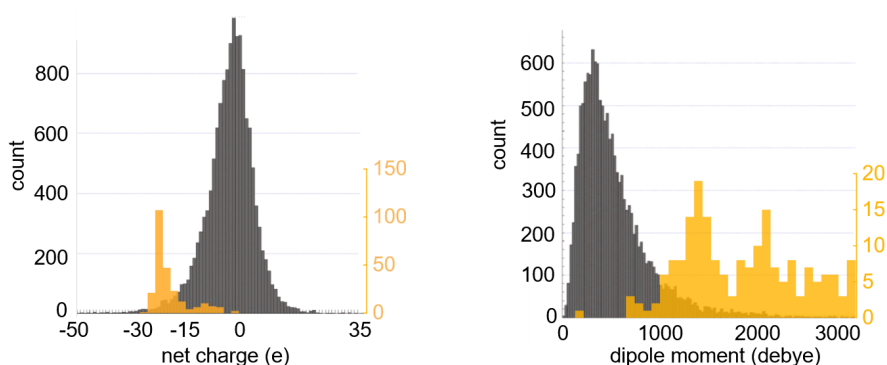


Figure 2.2: Distribution of electric charge (left) and dipole moment (right) in proteins (grey color) (12,000 PISCES set) and α - and β -tubulins (yellow color) from 240 species. Data of protein distribution obtained from work of Felder *et al.* [15].

fields. Another interesting experiment was performed by Ortner *et al.* [18] where they exposed microtubules to microwave radiation (2,450 MHz) during polymerization *in vitro*. They did not find any effect on polymerization in contrast to effects on cell division found in cells. Hence, they concluded that the cellular effects of microwaves are not directly connected with microtubules.

Whittier and Goddard [19] used radiofrequency reflectance spectroscopy to monitor polymerization of tubulin and the association with microtubule-related proteins by tracking changes in conductivity. Unfortunately, they did not extract any specific tubulin or microtubule parameters from the measured data. Microtubule behavior and alignment under strong electromagnetic field was also investigated by Ramalho *et al.* [20] or Uppalapati *et al.* [21]. Their experiment demonstrated again the possibility to manipulate with microtubules in the strong electromagnetic field and also estimate the microtubule conductivity to 250 mS/m. The most recent, controversial and instrumentally ingenious, an extensive experimental study revealed surprising properties of microtubule in axon core [22].

All of these results suggest unusual electric properties of the microtubule. Nevertheless is important to mention that results obtained by these experiments are not completely conclusive. For instance, in previously mentioned work [19], Whittier and Goddard performed measurement with the vector network analyzer but results obtained in such demanding and sensitive experiment are questionable due to calibration and position of their reference plains.

On the other hand, it is also worth to outline one of the most controversial topics of microtubule electromagnetic properties connected with the microtubule vibrations. In the case of the microtubule, these vibrations origin from the electrically polar tubulin structure. It was published earlier, that frequency of these vibration depends on the size and structure rigidity [23], as well as on the type of vibration mode [24]. This brings a new insight into the current-well established theory of vibrating modes of biomolecules which belongs to infrared region [25].

Due to the polar nature of tubulin, these vibrations can be in a specific condition a source of the electromagnetic field [26].

Debates have been taking place for quite a long time about this controversial topic. The authors like Pokorný argues and documents many scientific articles which provide experimental evidence that supports this theory. The arguments are connected with the existence of the bound water shell around the microtubule structure which has a decreased Brownian movement, but due to its own structure is also denser than bulk water [27]. Therefore bound (organized) water is expected to reduce longitudinal vibration damping with a comparison to free water. The reason is the existence of a sliding surface along the microtubule structure created by this water [28]. On a contrary, Foster and Baish [29] refer that all vibrations of microtubule in viscous cytosol structure are strongly damped. Till now, there are no experimental works which would quantify the damping coefficient or quality factor of vibrations on isolated microtubules to resolve this discussion. In this thesis, we contributed to this debate by our article in Section 4.

Craddock *et al.* [30] studied microtubules to investigate the existence of information processing in microtubules. By using a formalism of statistical physics and information processing they obtained a phase diagram of possible dynamic behaviors in microtubules. In later work, they tried to resolve a theory of energy transfer inside the tubulin. Based on their results, they suggest that coherent energy transfer in tubulin and microtubules is biologically feasible [31].

In all these studies a rather high value of tubulin refractive index (square root of dielectric constant) has been employed. To provide solid data for assessing several related-proposed or observed-controversial quantum and electromagnetic properties of microtubules [11, 32] we performed a solid experiment supported by a well-established theory, see Section 5.

2.2 DIELECTRIC SPECTROSCOPY – PROTEINS

The first works on dielectric spectroscopy of molecules [2], proteins [3, 33], and amino acids [34] are dated to early 1930s. During that time, most of fundamental theories about dielectric spectroscopy in liquids were established [35, 36]. Scientists were interested in interpretation of the dielectric increment as a direct result of protein content in solution [3], influence of protein dipole moment fluctuation [37], or on the completely other part of spectrum, in refractive index of proteins and how it is related to its amino acid composition [38].

These experiments, to our best knowledge, proved that electromagnetic force not only governs the behavior of biomolecules but could also serve as a probing tool to unravel and even change their properties or function. It can be used to modulate processes involving reactive oxygen species [39] or even regulates metabolic pathways [40]. There are also multiple proofs of the direct effect of intense electric field on proteins [41].

In addition, the electrical nature of biomolecules described by their dielectric properties influence the distribution of electromagnetic field and currents and determine their behavior in the electric field. The established elementary dielectric dispersion characteristic of proteins is described mainly by γ - and β -dispersion regions.

Processes involved in this dispersion regions were assigned to rearrangement of hydrogen-bonding network of water molecules (γ -dispersion) and the tumbling of the whole protein molecule (β -dispersion region). Figure 2.3 shows various molecular objects and their approximate tumbling relaxation frequencies (β -dispersion). Additionally, small dispersion (δ -dispersion) was discovered in works by Schwan [42], Grant *et al.*, Mashimo *et al.* [43, 44], and was attributed to relaxation of bounded water around protein. Experimental results showed different "states" of water (free water or bound surface water) in a water-protein environment which can have a direct impact on its structural and physical properties. The novelty of these experiments brought useful knowledge about protein behavior in their natural environment and opened the way to new discoveries over the century.

Later on, it was discovered that proteins in solution are known to produce "remarkably large increments" in the dielectric constant of water. These increments have been attributed to large permanent molecular electric dipole moments, which are partially oriented by an external electric field. A different interpretation was postulated by Kirkwood and Shumaker in work [37]. They related increments to dipole moment fluctuation which originate from the mobile proton distribution. Another interesting experiment was performed by Takashima [45] where he linked small dielectric increment of bovine serum albumin to charge distribution and its symmetry.

Step forward in topic of bound water is represented by Harvey and Hoekstra in their statement that bound water cannot be simply classified as "ice-like" or "not ice-like" because one of the observed properties (the relaxation time) is intermediate between that of ice and water, while another (the degree of order) is not [46]. Phenomena of bound water and their importance was deeper studied in other works [47–49] where experimental result suggested that in protein, water shell cannot relax freely and thus may be considered as part of the protein hydration shell. It also may have an influence on a variety of protein functions for all thermally activated processes at the protein–water interface, such as binding, recognition, and catalysis. Protein–water interactions are also known to influence the structure and protein function [50]. Still, nowadays it can be considered a particularly rich source of controversy and confusion in scientific community [51].

Important result in dispersion regions was observed by Oleinikova *et al.* [52]; observation of three further modes (δ_1 - δ_3) between β - and γ -relaxation, in contrast to a bimodal frequently reported δ -dispersion. The high-frequency part (δ_3) near 40 ps was attributed to hydration water reorientation, which, in the notion of other authors, corresponds to "loosely bound water".

Mellor *et al.* present a quantitative approach for measuring pH-controlled protein aggregation using dielectric spectroscopy [53]. Matyushov's theory [54] suggests an empirical equation that describes both the increment of the static dielectric constant and the decrements of the Debye water peak with increasing protein concentration. It gives fair agreement with broad-band dispersion and loss.

There are also many other papers which are focusing on theoretical modeling dielectric properties of a protein solution [55,56] and given electrostatic force models [57]. Wolf *et al.* [58] provide data on the temperature dependence of the relaxation times and relaxation strengths of all three detected processes and on the DC conductivity arising from ionic charge transport. The temperature dependencies of the β - and γ -relaxations are closely correlated. They found a significant temperature dependence of the protein dipole moment, indicating conformation changes.

For correct model of protein dielectric properties in solutions, knowledge of the dielectric constant plays a crucial role [55,59–63]. Incorrect value of dielectric constant also restrains the accuracy of methods for structure-based calculation of electrostatic energy [64] and limits our knowledge about forces in proteins.

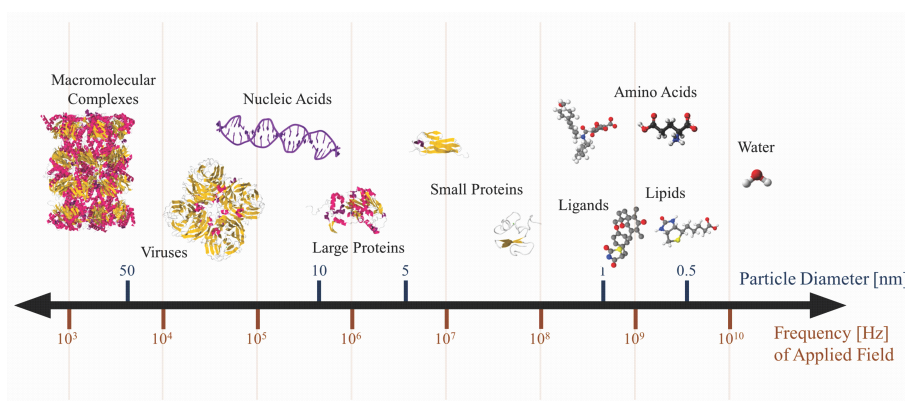


Figure 2.3: Spectrum of β -relaxation which was assigned to rearrangement of hydrogen-bonding network of water molecules of different molecular objects [65].

Thus part of this thesis is aimed at the electromagnetic characterization of microtubule structure by state of art dielectric spectroscopy method. Information gained will provide us with a better understanding of the dynamic behavior of the tubulin and microtubule. This characterization was our main target in Section 6

To summarize the current state of the art: due to biological ubiquity of microtubules and due to microtubule-related theories which predict far-reaching consequences in several research fields there is an urgent need for reliable experimental data and quantitatively predicting theoretical models of microtubule electrodynamic properties.

A more detailed overview of the current state of research on cellular electrodynamic phenomena and of microtubules is provided in introductory Sections 4, 5, 6, and Appendix A.

3 | GOALS OF THE THESIS

This thesis has the following goals:

- | Analytical model of vibrational damping of nanorod-structures in viscoelastic liquid environment.
- | Analytical model of electromagnetic interaction (absorption) of nanorod-structures in viscoelastic liquid environment.
- | Modeling and rigorous experimental analysis of refractive index of purified tubulin dimer.
- | Calculation of high frequency dielectric constant and polarizability of purified tubulin dimer.
- | Preliminary microwave spectroscopy of tubulin and microtubule in liquid phase.
- | Preliminary microwave spectroscopy of selected amino acids with analysis and verification of systematic errors in the measurement with designed sensor.
- | Design and fabrication of the new micropatterned planar microwave sensoric structures.
- | Acquisition and interpretation of broadband complex permittivity of microtubules.

4 | MICROWAVE ABSORPTION BY NANORESONATOR VIBRATIONS TUNED WITH SURFACE MODIFICATION

This chapter is a version of:

| **O. Krivosudský** and M. Cifra,

Microwave absorption by nanoresonator vibrations tuned with surface modification,

EPL: Europhysics Letters, vol. 115, issue 4, a. num. 44003, 2016. DOI: 10.1209/0295-5075/115/44003.

Author contributions:

| **Ondrej Krivosudský:**

Data curation, Formal analysis, Software, Visualization, Writing - original draft, Investigation (equal), Validation (equal), Methodology (equal)

| **Michal Cifra:**

Conceptualization, Funding acquisition, Project administration, Resources, Supervision, Writing - review & editing, Investigation (equal), Validation (equal), Methodology (equal)

| Candidate's contribution: 60%

The manuscript carries the following acknowledgements:

| We thank to Dr. Ondřej Kučera for useful comments on the manuscript, Dr N. Scott Lynn jr. for proofreading and an anonymous referee for comments which helped to improve the clarity of the manuscript. We acknowledge funding from Czech Science Foundation, project No. P102/15-17102S. The authors participate in COST Action BM1309 and project No. SAV-15-22 between Czech and Slovak Academies of Sciences.

Microwave absorption by nanoresonator vibrations tuned with surface modification

ONDREJ KRIVOSUDSKÝ and MICHAL CIFRA

Institute of Photonics and Electronics, The Czech Academy of Sciences - Prague, Czechia

received 2 April 2016; accepted in final form 5 September 2016

published online 26 September 2016

PACS 46.40.Ff – Resonance, damping, and dynamic stability

PACS 84.40.-x – Radiowave and microwave (including millimeter wave) technology

PACS 47.10.-g – General theory in fluid dynamics

Abstract – Elucidating the physical and chemical parameters that govern viscous damping of nanoresonator vibrations and their coupling to electromagnetic radiation is important for understanding the behavior of matter at the nanoscale. Here we develop an analytical model of microwave absorption of a longitudinally oscillating and electrically polar rod-like nanoresonator embedded in a viscoelastic fluid. We show that the slip length, which can be tuned via surface modifications, controls the quality factor and coupling of nanoresonator vibration modes to microwave radiation. We demonstrate that the larger slip length brings the sharper frequency response of the nanoresonator vibration and electromagnetic absorption. Our findings contribute to design guidelines of fluid embedded nanoresonator devices.

Copyright © EPLA, 2016

Introduction. – Mechanical nanoresonators can serve as probes having the ability to examine fundamental insights into the dynamic behavior of matter at the nanoscale [1,2]. Furthermore, their large surface-to-volume ratio makes their characteristics highly sensitive to surface effects when immersed in fluid; this feature gives nanoresonators immense potential to be a keystone of hypersensitive biological and chemical sensors [3–6]. The functional principle of these sensors is usually based on the shift of the resonant vibration frequency due to the selective addition of mass: for example, the capture of analyte by a functionalized nanoresonator surface [7]. In the quest to obtain higher sensitivities, it is thus desirable to understand both the vibrational response of the nanoresonator as well as the readout of frequency and damping parameters. In this paper, we develop quantitative theory for the design of nanoresonator vibration damping and propose a novel microwave read-out method.

Due to the combination of their inherent size, shape, stiffness and resonance character, nanoresonators typically operate in MHz–THz frequency range [8]; the most straightforward delivery of energy to nanoresonator for non-contact monitoring (*i.e.*, for sensing applications) of mechanical vibrations at these frequencies is through the electromagnetic radiation [9–13]. We focus on the coupling of monochromatic microwave radiation directly to electromagnetically active vibration modes of a nanoresonator

in this study. Monochromatic microwave radiation enables the resonant excitation of vibrational modes of the same frequency and has thus a higher selectivity than other alternatives, such as the broadband excitation by heating with femtosecond laser pulses [14]. This technique is also advantageous in cases in which samples scattering or the opacity of the experimental setup enclosure prohibits the usage of light. The quality factor (Q) of resonator vibrations is an important parameter that has a significant effect on the sensitivity for sensing applications [15] and furthermore, mediates information regarding nanoresonator material properties and interactions [16]. The mechanisms of vibrational damping at the nanoscale—where the molecular interactions of a nanoresonator with its surroundings become increasingly significant—have not been completely explored nor understood [17,18]. Unless prominent intrinsic damping is present in the resonator itself [16,19,20], major damping effects are expected to arise from the acoustic response of the surrounding liquid environment [21–23]. The Navier-Stokes equations are typically used to quantitatively analyze the dynamic behavior of such a liquid environment. For flows of simple fluids around relatively large objects it is often assumed that the liquid is Newtonian, where liquid in close proximity of a surface is motionless (no-slip condition), which has been found to be valid down to the nm scale [24]; however, in several applications a

departure from Newtonian behavior for simple liquids at the nanoscale has been reported as a result of the short time scale of nanoresonators vibrations [25] or due to extreme molecular confinement and structural reorganization on the molecular scale [26]. Such behavior suggests a need for incorporating elastic effects that are characteristic to non-Newtonian fluids. Additional results concerning non-Newtonian fluids have also suggested the presence of non-standard effects that can be interpreted as a violation of the no-slip condition at the solid-liquid boundary and are responsible for lowered energy dissipation into the fluid [18]. This violation of the no-slip boundary condition has been confirmed by several experiments [27–32] and furthermore, has been also shown to take place in high-frequency oscillatory regimes associated with nanoscale dimensions [33,34]. In this study we develop a theoretical framework to explore the possibility of engineering the vibrational damping of a nanomechanical resonator based solely on the modification of its surface properties and furthermore, to quantify the microwave absorption in a nanoresonator suspended in a thin film of fluid. We exploit the potential of slip of the fluid [28,31–33] at the nanoresonator surface and viscoelastic relaxation of the fluid taking place at high frequencies [35,36] which lower the vibrational damping.

Quality factor of nanoresonator vibrations in fluid. – To analyze the effect of the slip boundary condition on the vibration resonance, we consider the longitudinal vibration of a free cylindrical nanoresonator (nanorod or nanowire) with length L and radius R suspended in liquid as shown in fig. 1(a). Longitudinal vibrations are anticipated to displace less of the surrounding liquid and therefore should exhibit lower damping with respect to bending vibrations for the same energy in the mode. In addition, the longitudinal vibrations of a rod typically occupy a higher-frequency region with respect to bending vibrations, as the frequency of the former scales as $1/L$ vs. $1/L^2$ of the latter [37]. Consequently, the longitudinal vibrations of a nanoresonator take advantage of the effect of the viscoelastic relaxation of the liquid [35,36] at high-frequencies, and thus can potentially achieve a higher Q factor than the bending vibrations. The different frequency regions of operation of the longitudinal vs. bending modes also prevent their simultaneous excitation, which would both complicate the interpretation of experimental spectra and deteriorate sensing performance.

We first examine the behavior of water using the Maxwell model of shear stress, which is relevant for small strains [31] in the following form:

$$\tau + \lambda \frac{\partial}{\partial t} \tau = -\mu \dot{\gamma}, \quad (1)$$

where τ is the shear stress (*i.e.*, axial force per unit surface) acting on the nanoresonator surface, μ is the dynamic viscosity, $\dot{\gamma} = \left. \frac{\partial u(r,t)}{\partial r} \right|_{r=R}$ represents the strain rate, and λ is the relaxation time of the liquid water (lying in the

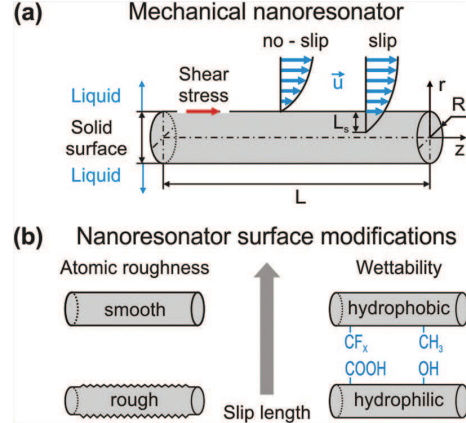


Fig. 1: (Color online) (a) Schematic illustration of fluid flow around a longitudinally vibrating cylindrical nanoresonator of length L and radius R . The slip boundary condition enables a non-zero velocity of the fluid at the nanoresonator surface. (b) Atomic-scale roughness and chemical modification of the nanoresonator surface affect the slip length.

picosecond region) [25,38]. In the special case that the relaxation time approaches zero, eq. (1) reduces to the well-known linear relationship of a Newtonian fluid. In order to determine the strain rate acting on a nanoresonator surface we consider the axially symmetric incompressible flow of a Maxwellian fluid around a cylinder along with a linear Navier slip boundary condition on the cylinder wall. The flow along the axial direction given by the momentum equation in cylindrical coordinates can thus be written as

$$\lambda \frac{\partial^2 u(r,t)}{\partial t^2} + \frac{\partial u(r,t)}{\partial t} = \nu \left(\frac{\partial^2 u(r,t)}{\partial r^2} + \frac{1}{r} \frac{\partial u(r,t)}{\partial r} \right), \quad (2)$$

where ν denotes the kinematic viscosity. The general slip boundary condition at the cylinder surface ($r = R$) undergoing longitudinal vibrations can be written in the form

$$u(r,t) = Ae^{i\omega t} + L_s \left. \frac{\partial u(r,t)}{\partial r} \right|_{r=R}, \quad (3)$$

where $u(r,t)$ is the velocity field and A is the velocity of the nanoresonator oscillations. The slip length L_s is considered constant, *i.e.*, independent of the strain rate or oscillation frequency. For the sake of simplicity we assume that the velocity is bound far from the cylinder, $u(\infty,t) = 0$. By substituting eq. (3) into eq. (2) the flow velocity can be expressed (similar to the result obtained by Fetecău [39], see footnote ¹ for more details) as

$$u(r,t) = Ae^{i\omega t} \frac{K_0(r\sqrt{\xi})}{K_0(R\sqrt{\xi}) + L_s\sqrt{\xi}K_1(R\sqrt{\xi})}, \quad (4)$$

where K_0 and K_1 are the zeroth- and first-order modified Bessel functions of the second kind, respectively. The term

¹See the supplemental material [SupportingInfo.pdf](#).

ξ is equal to $\omega(i - \lambda\omega)/\nu$. It follows that as L_s tends to zero, eq. (4) follows the solution obtained using a no-slip condition [40]. Substitution of eq. (4) into eq. (1) leads to the final form of the shear stress,

$$\tau = \int_0^t \left\{ \frac{\mu}{\lambda} e^{-(t-t')/\lambda} \right\} \dot{\gamma}(t') dt'. \quad (5)$$

In this integral, t is the time after one cycle ($2\pi/\omega_r$). The factor in the brackets represents the fading memory of the fluids rate-of-strain history. The most recent history has the greatest effect on the stress and the effect fades exponentially with time. The shear stress then can be evaluated as the absolute value of the complex function: with the real part representing losses as heat and changes to the imaginary part representing the energy stored in the material. The Q factor of vibrations is directly connected to the ratio of the imaginary to real parts as $Q = \tau''/\tau'$.

Microwave absorption due to nanoresonator vibrations. – For the wireless read-out of resonant frequency and the vibration damping, and the excitation of the nanoresonator vibrations using microwave radiation, we analyze absorption resulting from the electromagnetic coupling between the external field and nanoresonator. The excitation mechanism is not thermal but an electromechanical one; microwave radiation forces the bound charges on the resonator to mechanically oscillate and since the charges are bound to the structure, the structure is forced to oscillate as well. The power absorbed from the electromagnetic radiation depends on the nanoresonator absorption cross-section, which can be expressed as [10,41]

$$\sigma_a = 12\pi \left(\frac{c}{\omega} \right)^2 \frac{\Gamma_a \Gamma_s}{(\omega - \omega_r)^2 + \frac{\Gamma^2}{4}}, \quad (6)$$

where Γ_a, Γ_s are absorption and scattering widths and $\Gamma = \Gamma_a + \Gamma_s$ is the total width of the system. The absorption width can be directly associated to the Q factor of vibrations as $\Gamma_a = \omega_r/Q$, while the scattering width as $\Gamma_s = P_R/E_o$, where E_o represents the vibrational energy stored in the nanoresonator and P_R the electromagnetic power radiated by the oscillating charge associated with the nanoresonator vibration mode —effectively an oscillating dipole (see footnote ¹ for derivation).

Slip length control of vibration and microwave resonance. – The model presented here assumes that the vibrations of the resonator are purely linear. The vibrational part of our model is independent of the radius of the resonator. The resonant frequency of the considered vibration mode increases with decreasing nanoresonator length (see fig. 2(a)). This intuitive property is due to the fact that the nanoresonator can be approximated by a long ($L > R$) isotropic elastic rod that has a fundamental longitudinal vibration frequency given by $f = \sqrt{\frac{E}{\rho_{cyl}}}/(2L)$, where E is the Young modulus, ρ_{cyl} is the mass density of the rod [42,43]. The influence of the resonator length

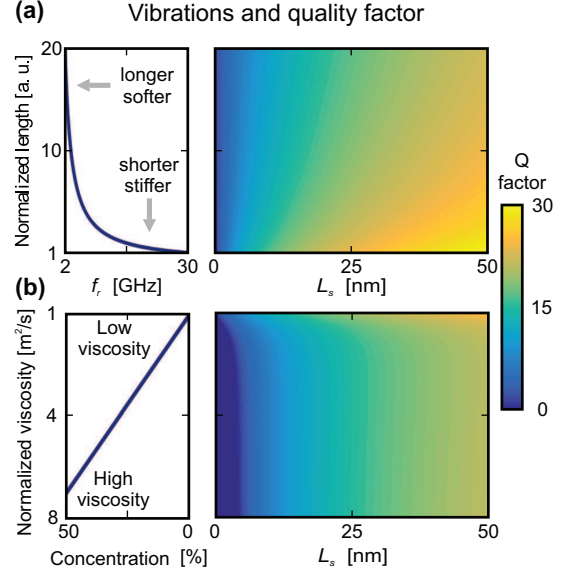


Fig. 2: (Color online) (a) Resonant frequency of the first longitudinal vibration mode depends on the length and stiffness of the nanoresonator. Length, stiffness and surface modifications (via slip length) can be used to tune the Q factor of the nanoresonator vibrations. The colorbar encodes the magnitude of Q factor. The vertical axis is the normalized length ($10^{11} L/\sqrt{E/\rho_{cyl}}$). (b) Kinematic viscosity (controlled, *e.g.*, by variable glycerol in water concentration) of the surrounding fluid can have a great impact on the Q factor of the nanoresonator vibrations. The vertical axis is the normalized kinematic viscosity ($(1-8)/10^{-6}$).

(through the frequency) and slip length on the vibrational Q factor is shown in fig. 2(a). The range of slip lengths considered herein ($L_s = 0-50$ nm) corresponds to conservative expectations based on both theory and achievable in experiments by surface modifications [24]. We found that while the Q factor is low (*i.e.*, high damping) and shows little variation across different nanoresonator lengths for a short slip length, a larger variation is observed for slip lengths over 30 nm. The results shown in fig. 2(a) suggest that more sensitive tuning of the nanoresonator Q factor —through the variation of its slip length— is possible for shorter or stiffer nanoresonators, *i.e.*, at higher frequencies. The vibrational characteristic of such nanoresonator system can be also tuned by modifying the kinematic viscosity of the surrounding fluid. The results shown in fig. 2(b) shows such vibrational characteristic of a 400 nm long nanoresonator immersed in water with variable glycerol concentration. By adding glycerol into water, viscosity and relaxation time are affected, ranging between $1-8 \times 10^{-6}$ m²/s and from 1 to 200 ps, respectively [38]. The Q factor increases with decreasing viscosity and increasing slip length in a complex manner since the shear stress is a nonlinear function of viscosity and slip length (see eqs. (1), (4) and (5)).

To connect our theoretical analysis to future experiments, we quantify the behavior of microwave absorption of randomly oriented nanoresonators suspended in a water film. The power P_{res} absorbed by such a population of nanoresonators can be connected to the absorption cross-section σ_a of a single nanoresonator as $P_{res} = \sigma_a I N_{res} / 3$ (see footnote ¹ for derivation), where I is the incident power density and N_{res} is a number of nanoresonators in a given volume. The description we develop here is completely general and requires only that the nanoresonator vibration mode under consideration is associated with a net change of dipole moment. In general, such effective dipole can arise from a nanoresonator surface charge-counterion double layer [44] or from the intrinsic polarization of the nanoresonator material [45]. To provide a specific example, we consider zinc oxide (ZnO) nanorods ($E = 160$ GPa [46], $\rho = 5606$ kg/m³, $L = 100$ – 1000 nm, radius $R = 25$ nm) as nanoresonators suspended in a $5 \mu\text{m}$ thick water film. ZnO is a low-cost semiconductor material and—due to its non-centrosymmetric wurtzite crystal structure—possesses a spontaneous polarization of about $P = 0.06$ C/m², with the exact value depending on the lattice orientation [45] and nanorod radius. This polarization, along with additional properties [2,45] such as the piezoelectric effect [47,48]—which can be connected with strain-induced macroscopic polarization—can create a dipole moment along the long axis of the nanoresonator and enable effective coupling of the first vibration mode to microwave radiation. The dipole moment is related to the effective charge q and polarization P as $p = qL = \int_V P dV$, where V is the volume of the nanoresonator. The effective charge density $q_s = q / (2\pi R^2)$ involved in the longitudinal vibration mode coupling to the microwave field can vary from tens to thousands of $\mu\text{C}/\text{cm}^2$. We varied the concentration of nanoresonators and the slip length in order to analyze their effect on the microwave absorption. In order to account for realistic conditions we have also included the microwave absorption of the water medium (see footnote ¹). From both fig. 3(a) and fig. 3(b), one can observe that the absorption increases with increasing concentration, slip length, surface charge density, and nanoresonator length (*i.e.*, the lowest resonant frequency considered). These quantitative predictions provide an estimation of the minimum required nanoresonator concentration (and their parameters) to acquire a sufficient signal-to-noise ratio for the broad range of experimental conditions. The highest microwave absorption of the nanoresonators over the water background takes place at the lowest frequencies. At first glance this may seem counterintuitive, as the vibration Q factor—as well as both the microwave absorption cross-section and absorbed power—increase with increasing frequency (fig. 2(a)); however, the microwave absorption by the water background also increases steeply with rising frequency and thus counteracts the effect of the rising nanoresonator vibration Q factor. The absorption curves in fig. 3(c) also show that higher

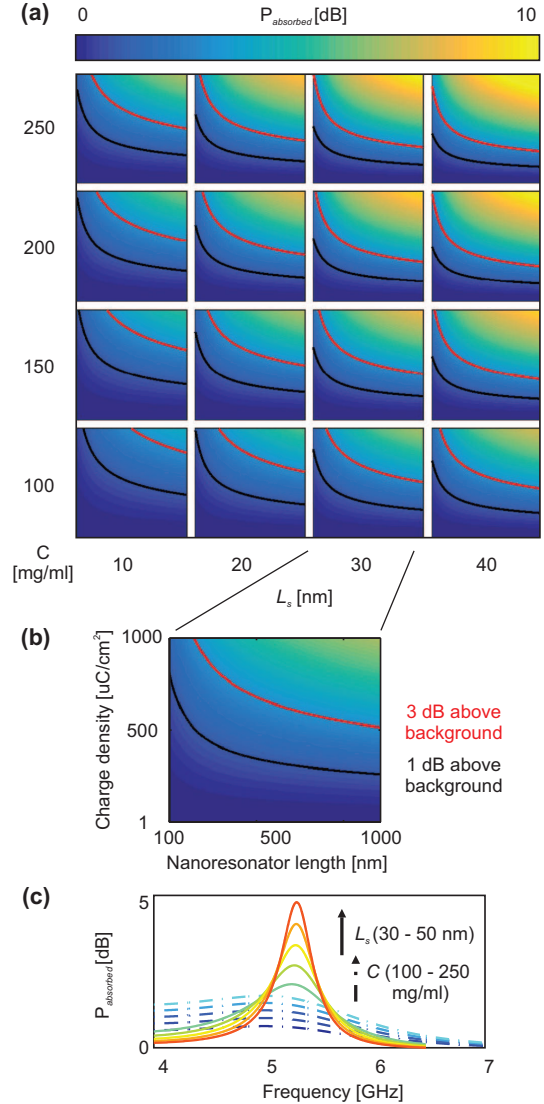


Fig. 3: (Color online) Microwave absorption of nanoresonators suspended in a water film is strongest for large slip lengths and high nanoresonator concentrations. (a) Microwave power absorbed by nanoresonators at their resonant frequency as a function of their concentration (C) and slip length (L_s). The black and red lines indicate the 1 dB and 3 dB power ratio above the water background. (b) The power absorption is calculated for nanoresonator lengths $L = 50$ – 1000 nm and surface charge densities $q_s = 1$ – $1000 \mu\text{C}/\text{cm}^2$. (c) Higher concentrations of nanoresonators ($C = 100$ – 250 mg/ml with 10 nm slip length, dashed line) yield increased microwave absorption around the resonant frequency. The slip length ($L_s = 30$ – 50 nm with 250 mg/ml concentration, solid line) increases the sharpness of the microwave absorption frequency response. The data here regards a 500 nm nanoresonator with a $500 \mu\text{C}/\text{cm}^2$ surface charge density.

concentrations lead to a stronger microwave absorption. For a fixed concentration of nanoresonators, our results show (fig. 3(c)) that the slip length has a strong influence on the frequency selectivity of the microwave absorption. While absorption curves are rather broad for slip lengths under 10 nm, they become increasingly sharper and distinct over the background absorption for larger slip lengths. Hence, the modification of the efficient slip length allows the tuning between a wider spectral bandwidth and a sharper frequency absorption response of the nanoresonators to the incident microwave radiation.

Discussion and conclusion. – The results presented herein demonstrate that i) the damping of the vibrations of a nanorod resonator is tunable through modification of both the length and the surface properties of the resonator, and that ii) the efficiency of the coupling of microwaves to these vibrations is limited by damping. Both the Young modulus and density of the nanoresonator are governed by the source material and its bulk properties (crystal lattice, porosity, . . .), and the length of the nanoresonators can be regulated by the speed and duration of the synthesis process during their fabrication. Together, these parameters enable control over the frequency range of the nanoresonator operation. The wettability of the nanoresonator material has a significant influence on the slip length of the surrounding liquid [49]. It has been confirmed—both by molecular dynamics as well as by experiments—that the slip length of water is higher on surfaces having a higher contact angle (*i.e.*, with high hydrophobicity) [24]. For instance, a short oxygen plasma treatment of glass and semiconductor surfaces forms polar hydroxyl groups, which, in turn, increase the hydrophilicity [50]. On the contrary, $-\text{CH}_x$, $-\text{CF}_x$ terminated or silylated surfaces [51,52] have a higher hydrophobicity, which can lead to a larger slip length (fig. 1(b)). Reversible switching between superhydrophobicity and superhydrophilicity of ZnO nanorods has been reported by alternating UV irradiation and storage in the dark [53]. Quantitatively, highly hydrophilic surfaces have slip lengths on the scale $< \text{nm}$, while highly hydrophobic surfaces reach effective slip lengths of few tens of nm [24]. Along a different approach, the surface roughness of the nanoresonator is another important property that has been shown to influence both the slip length [24,54] and damping of the nanoresonator vibrations [55] (fig. 1(b)): at the atomic and molecular scale, a higher roughness will lead to a shorter slip length [24]. Roughness at the macro- and mesoscopic scale lowers the fraction of the solid surface in a contact with liquid (the solid-liquid contact surface area) and can change the slip length [49]; although whether the mesoscopic roughness increases or decreases, the slip length depends on the surface energy at the atomic scale [56]. There are multiple surface functionalization techniques [57] (electrical-, optical-, pH- or temperature-based) that can control roughness and/or surface energy—hydrophilicity *vs.* hydrophobicity—of a material, thus

one can envisage tunable damping of the nanoresonator vibrations.

To summarize, we have developed a theoretical model of the vibrational damping and microwave absorption for a longitudinally oscillating cylindrical mechanical nanoresonator in a viscoelastic fluid that includes the use of a slip boundary condition. We have demonstrated that the slip at the solid-fluid boundary improves the quality factor of nanoresonator vibrations through the reduction of the effective shear stress and, furthermore, we have provided quantitative predictions for experiments such that relevant parameters can be optimized beforehand. The viscous damping of nanoresonator vibrations translates to its microwave absorption spectra, as microwave absorption is based on the coupling to the electromagnetically active vibration modes of the nanoresonator. We showed that while increases in both the nanoresonator concentration and slip length increase the microwave absorption at the resonance frequency, they do so in a distinct manner. While a higher concentration of nanoresonators increases the absorption magnitude, a larger slip length effectively decreases the bandwidth and increases the absorption only in the region close to the nanoresonator resonance frequency.

Our model provides a deeper understanding of the surface effects in nanoscale world dynamics. The procedure we developed can also be reversed and used as a basis for a novel method to characterize the surface properties of the nanoresonators and their interaction with fluids in a non-contact manner. We thus believe that this work contributes both to the design and characterization of nanoresonators for sensing applications and to the understanding of vibrational damping at the nanoscale in general.

We thank to Dr ONDŘEJ KUČERA for useful comments on the manuscript, Dr N. SCOTT LYNN jr. for proofreading and an anonymous referee for comments which helped to improve the clarity of the manuscript. We acknowledge funding from Czech Science Foundation, project No. P102/15-17102S. The authors participate in COST Action BM1309 and project No. SAV-15-22 between Czech and Slovak Academies of Sciences.

REFERENCES

- [1] PELTON M., SADER J. E., BURGIN J., LIU M., GUYOT-SIONNEST P. and GOSZTOLA D., *Nat. Nanotechnol.*, **4** (2009) 492.
- [2] WANG Z. L. and SONG J., *Science*, **312** (2006) 242.
- [3] VARSHNEY M., WAGGONER P. S., TAN C. P., AUBIN K., MONTAGNA R. A. and CRAIGHEAD H. G., *Anal. Chem.*, **80** (2008) 2141.
- [4] FISCHER L., WRIGHT V., GUTHY C., YANG N., MCDERMOTT M., BURIK J. and EVOY S., *Sens. Actuators B: Chem.*, **134** (2008) 613.

- [5] ARLETT J., MYERS E. and ROUKES M., *Nat. Nanotechnol.*, **6** (2011) 203.
- [6] TAMAYO J., KOSAKA P. M., RUZ J. J., SAN PAULO Á. and CALLEJA M., *Chem. Soc. Rev.*, **42** (2013) 1287.
- [7] EOM K., PARK H. S., YOON D. S. and KWON T., *Phys. Rep.*, **503** (2011) 115.
- [8] CLELAND A. N., *Foundations of Nanomechanics* (Springer-Verlag, Berlin, Heidelberg) 2003.
- [9] UNTERREITHMEIER Q. P., WEIG E. M. and KOTTHAUS J., *Nature*, **458** (2009) 1001.
- [10] JAVAHERI H., BARBIELLINI B. and NOUBIR G., *Nanoscale Res. Lett.*, **7** (2012) 1.
- [11] LIU T. M., LU J. Y. and CHEN, *Appl. Phys. Lett.*, **92** (2008) 093122.
- [12] LIU T., CHEN H., YEH S., WU C., WANG C., LUO T., CHEN Y., LIU S. and SUN C., *Appl. Phys. Lett.*, **95** (2009) 173702.
- [13] LIU T., CHEN H., WANG L., WANG J., LUO T., CHEN Y., LIU S. and SUN C., *Appl. Phys. Lett.*, **94** (2009) 043902.
- [14] PERNER M., GRESILLON S., MÁRZ J., VON PLESSEN G., FELDMANN J., PORSTENDORFER J., BERG K.-J. and BERG G., *Phys. Rev. Lett.*, **85** (2000) 792.
- [15] WAGGONER P. S. and CRAIGHEAD H. G., *Lab Chip*, **7** (2007) 1238.
- [16] PELTON M., WANG Y., GOSZTOLA D. and SADER J. E., *J. Phys. Chem. C*, **115** (2011) 23732.
- [17] FORD L., *Phys. Rev. E*, **67** (2003) 051924.
- [18] CHAKRABORTY D., VAN LEEUWEN E., PELTON M. and SADER J. E., *J. Phys. Chem. C*, **117** (2013) 8536.
- [19] RUIJGROK P. V., ZIJLSTRA P., TCHEBOTAREVA A. L. and ORRIT M., *Nano Lett.*, **12** (2012) 1063.
- [20] VAN DIJK M. A., LIPPITZ M. and ORRIT M., *Phys. Rev. Lett.*, **95** (2005) 267406.
- [21] VOISIN C., CHRISTOFILOS D., FATTI N. D. and VALLE F., *Physica B: Condens. Matter*, **316-317** (2002) 89.
- [22] MARTY R., ARBOUET A., GIRARD C., MLAYAH A., PAILLARD V., LIN V. K., TEO S. L. and TRIPATHY S., *Nano Lett.*, **11** (2011) 3301.
- [23] HU M., NOVO C., FUNSTON A., WANG H., STALEVA H., ZOU S., MULVANEY P., XIA Y. and HARTLAND G. V., *J. Mater. Chem.*, **18** (2008) 1949.
- [24] BOCQUET L. and CHARLAIX E., *Chem. Soc. Rev.*, **39** (2010) 1073.
- [25] PELTON M., CHAKRABORTY D., MALACHOSKY E., GUYOT-SIONNEST P. and SADER J. E., *Phys. Rev. Lett.*, **111** (2013) 244502.
- [26] ISRAELACHVILI J. N., MCGUIGGAN P. M. and HOMOLA A. M., *Science*, **240** (1988) 189.
- [27] CASADO-DÍAZ J., LUNA-LAYNEZ M. and SUÁREZ-GRAU F., *SeMA J.*, **58** (2012) 5.
- [28] ATWOOD B. and SCHOWALTER W., *Rheol. Acta*, **28** (1989) 134.
- [29] MIGLER K. B., HERVET H. and LEGER L., *Phys. Rev. Lett.*, **70** (1993) 287.
- [30] BROCHARD F. and DE GENNES P. G., *Langmuir*, **8** (1992) 3033.
- [31] SCHOWALTER W., *J. Non-Newtonian Fluid Mech.*, **29** (1988) 25.
- [32] HORN R. G., VINOGRADOVA O. I., MACKAY M. E. and PHAN-THIEN N., *J. Chem. Phys.*, **112** (2000) 6424.
- [33] ELLIS J. S. and THOMPSON M., *Phys. Chem. Chem. Phys.*, **6** (2004) 4928.
- [34] HUANG K. and SZLUFARSKA I., *Langmuir*, **28** (2012) 17302.
- [35] MONACO G., CUNSOLO A., RUOCCO G. and SETTE F., *Phys. Rev. E*, **60** (1999) 5505.
- [36] KARABACAK D., YAKHOT V. and EKINCI K., *Phys. Rev. Lett.*, **98** (2007) 254505.
- [37] MEIROVITCH L., *Fundamentals of Vibrations* (McGraw-Hill) 2010.
- [38] SLIE W. M., DONFOR A. R. and LITOVITZ T. A., *J. Chem. Phys.*, **44** (1966) 3712.
- [39] FETECĂU C. and FETECĂU C., *Proc. Rom. Acad. - Ser. A: Math. Phys. Tech. Sci. Info. Sci.*, **8** (2007) 77.
- [40] FOSTER K. R. and BAISH J. W., *J. Biol. Phys.*, **26** (2000) 255.
- [41] ADAIR R. K., *Biophys. J.*, **82** (2002) 1147.
- [42] LOVE A. E. H., *A Treatise on the Mathematical Theory of Elasticity*, Vol. **1** (Cambridge University Press) 1906.
- [43] ZIJLSTRA P., TCHEBOTAREVA A. L., CHON J. W., GU M. and ORRIT M., *Nano Lett.*, **8** (2008) 3493.
- [44] ELFSTRM N., JUHASZ R., SYCHUGOV I., ENGFELDT T., KARLSTRM A. E. and LINNROS J., *Nano Lett.*, **7** (2007) 2608.
- [45] BERNARDINI F., FIORENTINI V. and VANDERBILT D., *Phys. Rev. B*, **56** (1997) R10024.
- [46] WEN B., SADER J. E. and BOLAND J. J., *Phys. Rev. Lett.*, **101** (2008) 175502.
- [47] AGRAWAL R. and ESPINOSA H. D., *Nano Lett.*, **11** (2011) 786.
- [48] QIN C., GU Y., SUN X., WANG X. and ZHANG Y., *Nano Res.*, **8** (2015) 2073.
- [49] BOCQUET L. and BARRAT J.-L., *Soft Matter*, **3** (2007) 685.
- [50] GRUNDNER M. and JACOB H., *Appl. Phys. A*, **39** (1986) 73.
- [51] CHEN J.-K., HSIEH C.-Y., HUANG C.-F., LI P.-M., KUO S.-W. and CHANG F.-C., *Macromolecules*, **41** (2008) 8729.
- [52] ARKLES B., *Silane and Surface: Hydrophobicity, Hydrophilicity and Coupling Agents* (Gelest, Inc.) 2011.
- [53] FENG X., FENG L., JIN M., ZHAI J., JIANG L. and ZHU D., *J. Am. Chem. Soc.*, **126** (2004) 62.
- [54] NIAVARANI A. and PRIEZJEV N. V., *Phys. Rev. E*, **81** (2010) 011606.
- [55] PALASANTZAS G., *J. Appl. Phys.*, **103** (2008) 046106.
- [56] COTTIN-BIZONNE C., BARRAT J.-L., BOCQUET L. and CHARLAIX E., *Nat. Mater.*, **2** (2003) 237.
- [57] VERPLANCK N., COFFINIER Y., THOMY V. and BOUKHERROUB R., *Nanoscale Res. Lett.*, **2** (2007) 577.

5 | RESOLVING CONTROVERSY OF UNUSUALLY HIGH REFRACTIVE INDEX OF TUBULIN

This chapter is a version of:

| **O. Krivosudský**, P. Dráber and M. Cifra,
Resolving controversy of unusually high refractive index of tubulin,
EPL: Europhysics Letters, vol. 117, issue 3, a. num. 38003, 2017. DOI: 10.1209/0295-5075/117/38003.

Author contributions:

| **Ondrej Krivosudský:**
Data curation, Formal analysis, Software, Visualization, Writing - original draft, Investigation (equal),
Methodology (equal)

| **Pavel Dráber:**
Resources (supporting), Writing - review & editing (supporting), Validation (supporting)

| **Michal Cifra:**
Conceptualization, Funding acquisition, Project administration, Resources (lead), Supervision,
Writing - review & editing (lead), Validation (lead), Methodology (equal), Investigation (equal)

| Candidate's contribution: 60%

The manuscript carries the following acknowledgements:

| The research presented in this paper was supported by the Czech Science Foundation, projects no. P102/15-17102S and P302/16-25159S and by Institutional Research Support (RVO 68378050). Authors participate in COST Action BM1309 and bilateral exchange project between Czech and Slovak Academies of Sciences, no. SAV-15-22.

Resolving controversy of unusually high refractive index of a tubulin

O. KRIVOSUDSKÝ^{1(a)}, P. DRÁBER^{2(a)} and M. CIFRA^{1(a)}

¹ *Institute of Photonics and Electronics, The Czech Academy of Sciences - Prague, Czechia*

² *Institute of Molecular Genetics, The Czech Academy of Sciences - Prague, Czechia*

received 19 October 2016; accepted in final form 2 March 2017

published online 23 March 2017

PACS 87.16.Ka – Filaments, microtubules, their networks, and supramolecular assemblies

PACS 78.20.Ci – Optical constants (including refractive index, complex dielectric constant, absorption, reflection and transmission coefficients, emissivity)

PACS 87.14.E- – Proteins

Abstract – The refractive index of a tubulin is an important parameter underlying fundamental electromagnetic and biophysical properties of microtubules – protein fibers essential for several cell functions including cell division. Yet, the only experimental data available in the current literature show values of the tubulin refractive index ($n = 2.36$ – 2.90) which are much higher than what the established theories predict based on the weighted contribution of the polarizability of individual amino acids constituting the protein. To resolve this controversy, we report here modeling and rigorous experimental analysis of the refractive index of a purified tubulin dimer. Our experimental data revealed that the refractive index of the tubulin is $n = 1.64$ at wavelength 589 nm and 25 °C, that is much closer to the values predicted by the established theories than what the earlier experimental data provide.

Copyright © EPLA, 2017

Introduction. – The refractive index (n) is a fundamental material property which determines the interaction of light with a material. Microtubules, assembled from $\alpha\beta$ -tubulin heterodimers, represent an active biopolymer material which participates in essential cellular functions. α - and β -tubulins are highly conserved and consist of isotypes encoded by different genes [1]. Knowledge of the tubulin refractive index is essential not only for the accurate interpretation of the results from novel cytoskeleton label-free imaging methods [2], construction and optical characterization of hybrid biological microtubule-based nanodevices [3], but since it is directly related to the dielectric constant ϵ ($\epsilon = n^2$) it is also crucial for accurate electrostatic and coarse-grained molecular modeling of microtubules [4,5] and the design of di/electric manipulation techniques [6]. Well-established theories predict the refractive index of most proteins typically in the range $n = 1.5$ – 1.7 [7]. However, the experimental values of the tubulin and microtubule refractive index available until now in the literature are in

the range of $n = 2.36$ – 2.90 [2,8,9]. Many studies [10–12] which employed this high value of tubulin refractive index have already been performed. To resolve this discrepancy and to provide solid data for assessing several related – proposed or observed – controversial quantum and electromagnetic properties of microtubules [13,14], we carried out a theoretical analysis of the refractive index of the tubulin based on its primary structure and performed well-characterized experiments to obtain a refractive index increment (dn/dc) and the refractive index of both unpolymerized and polymerized tubulin.

Theory. – Our theoretical analysis of the refractive index of the tubulin is based on the contribution of the polarizability of individual amino acids which constitute the tubulin isotypes. The number of amino acids contained in a $\alpha\beta$ -tubulin heterodimer was obtained from two different models. The first model is derived from a protein sequence of a porcine tubulin (*Sus scrofa*). In mammals, the β -tubulin comprises 7 isotypes and the α -tubulin comprises 9 isotypes, each of which is a product encoded by a distinct gene [1,15,16]. We included several α -tubulin isotypes which are found in porcine tubulin. An overview of the used tubulin isotypes with UniProt database identifiers (ID) is shown in table 1. The detailed composition is

^(a) Authors' contributions: OK conceived the experiments and modeling and drafted the paper, PD provided the experimental material and important methodical suggestions, MC designed the research and co-wrote the paper.

Table 1: Overview of *Sus scrofa* tubulin isotypes and BSA.

Isotype	Gene name	ID UniPortKB
$\alpha 1A$	<i>TUBA1A</i>	P02550
$\alpha 1B$	<i>TUBA1B</i>	Q2XVP4
$\alpha 4A$	<i>TUBA4B</i>	F2Z5S8
$\alpha 8$	<i>TUBA8</i>	I3LDR2
βI	<i>TUBB</i>	Q767L7
βII	<i>TUBB2B</i>	F2Z5B2
βIII	<i>TUBB3</i>	F1S6M7
βIVa	<i>TUBB4A</i>	F2Z5K5
βIVb	<i>TUBB4B</i>	F2Z571
βV	<i>TUBB6</i>	I3LBV1
βVI	<i>TUBB1</i>	A5GFX6

	ID RCSB database
α -tubulin chain	1TUB: <i>A</i> GI:3745821
β -tubulin chain	1TUB: <i>B</i> GI:3745822
Bovine serum albumin	4F5S: <i>A, B</i> P02769

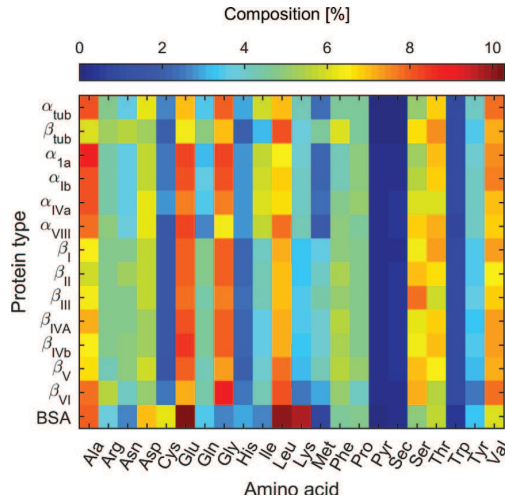
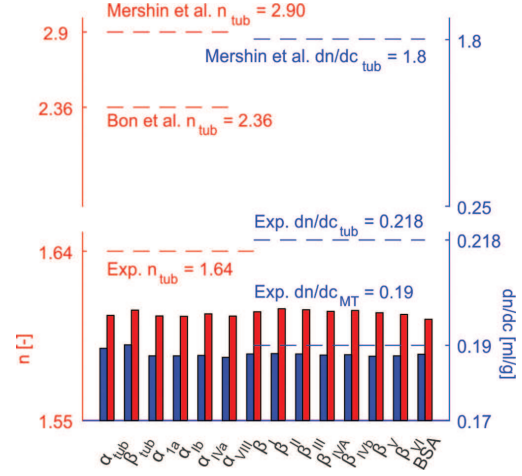


Fig. 1: (Color online) Amino acid composition of individual tubulin isotypes used in the theoretical calculation of the tubulin refractive index given by the RCSB Protein Data Bank and UniProt database. The color encodes the percentual contribution of individual amino acids in the tubulin molecule and its isotypes.

displayed in fig. 1). The composition of the second tubulin model is based on the experimentally determined crystallographic structure 1TUB [17] obtained from the RCSB protein database.

Refractive index of protein (n_p) can be obtained as a variation of the Lorentz-Lorenz formula which is given as a ratio

$$n_p = \sqrt{\frac{2R_p + \bar{v}_p}{\bar{v}_p - R_p}}, \quad (1)$$


 Fig. 2: (Color online) Bars represent the theoretical values of the refractive index (red bars) and dn/dc (blue bars) of the tubulin and bovine serum albumin. Dashed lines are our experimental data (labeled as Exp.) vs. earlier experimental data. Our data were experimentally obtained and theoretically calculated for wavelength 589.3 nm and 25 °C. The values from Mershin *et al.* [8,9] are at 760 nm and 26 °C and those from Bon *et al.* [2] for 527 nm and room temperature.

where R_p is the refraction per gram of the protein given by averaged contributions of its individual amino acids R_a [18,19] and their molecular masses M_a in the following way:

$$R_p = \frac{\sum_a R_a M_a}{\sum_a M_a} \quad (2)$$

and the protein partial specific volume \bar{v}_p which can be also estimated as a weighted average of specific volumes (\bar{v}_a) of individual amino acids [20,21]

$$\bar{v}_p = \frac{\sum_a \bar{v}_a M_a}{\sum_a M_a}. \quad (3)$$

Based on the theoretical prediction of the protein refractive index (eq. (1)) and a mixture rule represented by the Wiener equation [22] the refractive index increment can be estimated by using the following equation:

$$\frac{dn}{dc} = \frac{3}{2} \bar{v}_p n_{buffer} \frac{n_p^2 - n_{buffer}^2}{n_p^2 + 2n_{buffer}^2} \quad (4)$$

with a buffer refractive index n_{buffer} .

Based on the values of the refraction per gram and the specific volumes of individual amino acids available in the literature [18–21] and the tubulin composition, we predicted dn/dc and the refractive index of the tubulin isotypes as well as of the bovine serum albumin (BSA) as a reference protein. See fig. 2 and the supplementary material [SupplementaryMaterial.pdf](#) (SM) for more details.

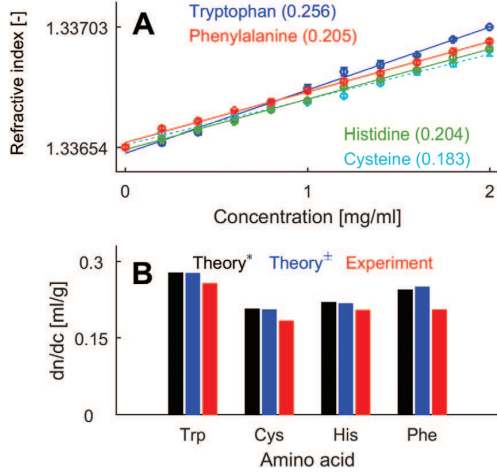


Fig. 3: (Color online) (A) Refractive index n of amino acid solutions. Data points were fitted by a first-order polynomial (linear regression was performed). The slope of the curve represents the refractive index increment of the given solution. (B) Predicted theoretical and experimental data (red) of amino acids. Theory* (black): data were predicted at 589 nm for a hypothetical polypeptide in water with 150 mM NaCl [7]. Theory[±] (blue): data calculation is based on the evaluation of eq. (4) for the amino acid buffer (BRB80) solution with specific volumes and refraction of individual amino acids [18–21].

Experiments. – To measure the refractive index, we used a critical-angle dispersion-refractometer with thermal regulation (DSR- λ SCHMIDT+HAENSCH) in all experiments. At first, we experimentally analyzed dn/dc of selected amino acids (see fig. 3(A)) and thereby verified that our method yields values consistent with the literature [18,19]. All refractive index measurements were carried out at 589 nm and sample temperature 25 °C since the values of the amino acid dn/dc from the literature were also at this wavelength and temperature.

Additionally, this temperature also prevents spontaneous polymerization of the tubulin in our conditions. All amino acids, tubulin (>99% purity, # T238P, Cytoskeleton, Inc.) and BSA (\geq 98% purity, A3803, Sigma-Aldrich) were stored in the BRB80 buffer (80 mM PIPES, 2 mM MgCl₂, 0.5 mM EGTA, 1 mM GTP, 6.9 pH, KOH). For the tubulin and BSA, the refractive index of their concentration series from 0 to 2 mg/ml (11 steps, each with 50 μ l sample volume) has been measured (each series took 75 min, with the tubulin run in an independent triplicate) to obtain dn/dc . Finally, the refractive index increment of a polymerized tubulin was measured. The tubulin was polymerized in the BRB80 buffer by adding taxol stepwise at 2, 20 and 200 μ M steps at 37 °C [23]. The results in fig. 3(A) indicate that the amino acid dn/dc is independent of concentration. A least-square fit linear regression yields straight lines, and dn/dc of amino acids did not deviate significantly from the established theoretical values, for details see SM. We obtained the refractive index of

proteins from their measured dn/dc (fig. 2) following the method outlined in [9]. In brief, assuming the contribution from all the buffer components we can write the refractive index of the tubulin as

$$n_{tub} = \frac{n_{sol} - (1 - \chi_p)n_{buffer}}{\chi_p}, \quad (5)$$

where $\chi_p = C_{tub}/\rho$ is the protein mass fraction with density ρ and refractive index of the solution n_{sol} which is based on the refractive index increment (dn/dc) in the following way:

$$n_{sol} = \frac{dn}{dc}C_{tub} + n_{buffer}. \quad (6)$$

As a tubulin concentration, $C_{tub} = 1.60$ mg/ml was used with the protein density $\rho = 1.41$ g/ml. Given by the experimental data of the tubulin increment (see fig. 2) solution, refractive index follows as

$$n_{sol} = 2.18 \times 10^{-4}C_{tub} + 1.33654 \quad (7)$$

and by applying eq. (5), the refractive index of the tubulin was found to have the value

$$n_{tub} = 1.64 \pm 0.02 @ 589 \text{ nm} @ 25 \text{ }^\circ\text{C}. \quad (8)$$

By using the same procedure with bovine serum albumin, $dn/dc_{BSA} = 0.179$ ml/g was measured, which results in the refractive index $n_{BSA} = 1.59 \pm 0.02$, which is in good agreement with the theoretical predictions. For microtubules, we experimentally obtained the value $dn/dc_{MT} = 0.19$ ml/g which would correspond to $n_{MT} = 1.60$. However, the Lorentz-Lorenz formula used to calculate the polarizability and the refractive index based on dn/dc assumes a spherical approximation of the particle ([24], pp. 88–92) which obviously is not valid for the microtubules. The small discrepancies between theory and experiment for n_{tub} and dn/dc_{tub} can be due to i) the deviation of the tubulin dimer shape from the spherical one assumed in the theory, ii) small concentration uncertainties, iii) effects of the buffer on dn/dc [25] or iv) additional polarization effects in the tubulin due to its large dipole moment [26,27]. The protein charge (influenced by pH) can also exert a slight effect on the observed refractive index via electrostatic interactions with the solvent (here water molecules) [18]. The tubulin dimer (110 kDa) charge is around $-25 e$ [26] and the BSA (66 kDa) charge is around $-15 e$ [28,29] at pH 7, hence both possess similar charge-to-mass ratio. Our theoretical calculations agree very well with the experimental data for BSA and also very satisfactorily for the tubulin, so we have reason to believe that the protein charge similar to the tubulin does not significantly affects results in our conditions.

The high-frequency polarizability (α_{tub}) of the tubulin can be also evaluated by using the well-known Clausius-Mossotti relationship in the following form:

$$\alpha_{tub} = \frac{3\epsilon_0 n_{tub}^2 - 1}{N n_{tub}^2 + 2} \quad (9)$$

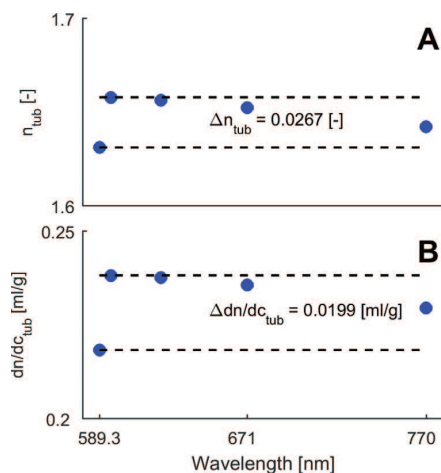


Fig. 4: (Color online) (A) Refractive index of the tubulin at different wavelengths calculated from (B) refractive index increments.

which, with the calculated number density of molecules $N = 8.7 \times 10^{21}$ per m^3 at a given concentration (C_{tub}), is equal to $\alpha_{tub} = 1.1 \times 10^{-33} \text{ Cm}^2\text{V}^{-1}$.

Discussion and conclusion. – What effect caused the high values of the detected refractive index in the earlier experimental works [2,8,9] is unclear. In the case of [8,9], $n_{tub} = 2.90 \pm 0.10$ was obtained using both surface plasmon resonance sensing as well as a refractometry technique similar to ours. While authors of [8,9] used a different wavelength (760 nm) from ours (589 nm), we found from our experiments only a very small difference of n ($\Delta n = n_{tub@770} - n_{tub@589} < 0.011$, see fig. 4 for the wavelength dependence) which does not explain the discrepancy. In the newer work [2], the refractive index of single microtubules was extracted using a quantitative phase imaging-based microscopy technique from fixed fluorescently labeled cells with a rather large error ($n_{MT} = 2.36 \pm 0.6$) – the cause of the high value of n is not entirely clear but might be due to the assumptions in the model required to extract n from their experimental data.

To summarize, we provide experimental data supported by theoretical modeling which reveal that the refractive index of the unpolymerized and polymerized tubulin is in the range $n_{tub} = 1.6\text{--}1.64$, yielding a high-frequency dielectric constant $\epsilon = 2.56\text{--}2.69$. This value provides lower dielectric screening within the tubulin than what previously thought. Lower screening enables larger interaction distance of the electrostatic forces within microtubules than what previously considered based on the higher values of ϵ [10]. Further implications are for the exciton energy transfer within the tubulin; lower n enhances electronic dipole-dipole coupling due its $(1/n^4)$ -dependence [30] suggesting a resonant energy transfer on a longer range than previously estimated [12]. We believe our data will enable a more accurate tubulin and

microtubule characterization and modeling much beyond the few examples we illustrated.

The research presented in this paper was supported by the Czech Science Foundation, projects Nos. P102/15-17102S and P302/16-25159S and by Institutional Research Support (RVO 68378050). Authors participate in COST Action BM1309 and bilateral exchange project between Czech and Slovak Academies of Sciences, No. SAV-15-22.

REFERENCES

- [1] LUDUEÑA R. F. and BANERJEE A., *The Role of Microtubules in Cell Biology, Neurobiology, and Oncology* (Humana Press, Totowa, NJ) 2008, Chapt. *The Isoforms of Tubulin*, pp. 123–175.
- [2] BON P., LÉCART S., FORT E. and LÉVÊQUE-FORT S., *Biophys. J.*, **106** (2014) 1588.
- [3] KORTEN T., MÅNSSON A. and DIEZ S., *Curr. Opin. Biotechnol.*, **21** (2010) 477.
- [4] BAKER N. A., SEPT D., JOSEPH S., HOLST M. J. and MCCAMMON J. A., *Proc. Natl. Acad. Sci. U.S.A.*, **98** (2001) 10037.
- [5] DERIU M. A., SONCINI M., ORSI M., PATEL M., ESSEX J. W., MONTEVECCHI F. M. and REDAELLI A., *Biophys. J.*, **99** (2010) 2190.
- [6] VAN DEN HEUVEL M. G., DE GRAAFF M. P. and DEKKER C., *Science*, **312** (2006) 910.
- [7] ZHAO H., BROWN P. H. and SCHUCK P., *Biophys. J.*, **100** (2011) 2309.
- [8] SCHUESSLER H., MERSHIN A., KOLOMENSKI A. and NANOPOULOS D., *J. Mod. Opt.*, **50** (2003) 2381.
- [9] MERSHIN A., KOLOMENSKI A., SCHUESSLER H. and NANOPOULOS D., *Biosystems*, **77** (2004) 73.
- [10] SCHOUTENS J. E., *J. Biol. Phys.*, **31** (2005) 35.
- [11] CRADDOCK T. J., BEAUCHEMIN C. and TUSZYNSKI J. A., *Biosystems*, **97** (2009) 28.
- [12] CRADDOCK T. J. A., FRIESEN D., MANE J., HAMEROFF S. and TUSZYNSKI J. A., *J. R. Soc. Interface*, **11** (2014) 20140677.
- [13] SAHU S., GHOSH S., GHOSH B., ASWANI K., HIRATA K., FUJITA D. and BANDYOPADHYAY A., *Biosens. Bioelectron.*, **47** (2013) 141.
- [14] HAMEROFF S., *Top. Cogn. Sci.*, **6** (2014) 91.
- [15] LUDUEÑA R. F., *International Review of Cell and Molecular Biology*, Vol. **302** (Academic Press) 2013, Chapt. 2, *A hypothesis on the origin and evolution of tubulin*, pp. 41–185.
- [16] LUDUEÑA R. F., *Multiple forms of tubulin: Different gene products and covalent modifications*, *International Review of Cytology*, Vol. **178** (Academic Press) 1997, pp. 207–275.
- [17] NOGALES E., WOLF S. G. and DOWNING K., *Nature*, **391** (1998) 199.
- [18] MCMEEKIN T. L., GROVES M. L. and HIPPI N. J., *Refractive Indices of Amino Acids, Proteins, and Related Substances*, *Advances in Chemistry*, Vol. **44** (American Chemical Society) 1964, Chapt. 5, pp. 54–66.
- [19] MCMEEKIN T. L., WILENSKY M. and GROVES M. L., *Biochem. Biophys. Res. Commun.*, **7** (1962) 151.

-
- [20] DURCHSCHLAG H., *Thermodynamic Data for Biochemistry and Biotechnology* (Springer, Berlin, Heidelberg) 1986.
- [21] ZAMYATNIN A. A., *Annu. Rev. Biophys. Bioeng.*, **13** (1984) 145.
- [22] HELLER W., *J. Phys. Chem.*, **69** (1965) 1123.
- [23] DESAI A. and MITCHISON T. J., *Annu. Rev. Cell Dev. Biol.*, **13** (1997) 83.
- [24] BORN M. and WOLF E., *Principles of Optics: Electromagnetic Theory of Propagation, Interference and Diffraction of Light* (Cambridge University Press) 2000.
- [25] BALL V. and RAMSDEN J. J., *Biopolymers*, **46** (1998) 489.
- [26] TUSZYŃSKI J. A., CARPENTER E. J., HUZIL J. T., MALINSKI W., LUCHKO T. and LUDUEÑA R. F., *Int. J. Dev. Biol.*, **50** (2006) 341.
- [27] TUSZYŃSKI J., BROWN J., CRAWFORD E., CARPENTER E., NIP M., DIXON J. and SATARIC M., *Math. Comput. Model.*, **41** (2005) 1055.
- [28] SALIS A., BOSTRM M., MEDDA L., CUGIA F., BARSE B., PARSONS D. F., NINHAM B. W. and MONDUZZI M., *Langmuir*, **27** (2011) 11597.
- [29] BÖHME U. and SCHELER U., *Chem. Phys. Lett.*, **435** (2007) 342.
- [30] ANDREWS D. L., CURUTCHET C. and SCHOLES G. D., *Laser Photon. Rev.*, **5** (2011) 114.

6 | ON-CHIP MICROWAVE SENSING OF TUBULIN AND ITS POLYMER

This chapter is a version of:

| **O. Krivosudský**, D. Havelka, D. E. Chafai and M. Cifra,
On-chip microwave sensing of tubulin and its polymer,
Submission in process

Author contributions:

| **Ondrej Krivosudský:**
Conceptualization, Data curation, Formal analysis, Investigation, Methodology, Software, Supervision,
Visualization (supporting), Writing - original draft (lead), Writing - review & editing

| **Daniel Havelka:**
Conceptualization, Data curation, Formal analysis, Investigation, Methodology, Software, Supervision,
Visualization (lead), Writing - original draft (supporting), Writing - review & editing (supporting)

| **Djamel Eddine Chafai:**
Data curation (supporting), Formal analysis (supporting), Investigation (supporting),
Methodology (supporting), Writing - original draft (supporting), Writing - review & editing

| **Michal Cifra:**
Conceptualization, Formal analysis (supporting), Funding acquisition, Investigation (supporting),
Project administration, Resources, Supervision, Validation, Writing - original draft (supporting),
Writing - review & editing

| Candidate's contribution: 35%

The manuscript carries the following acknowledgements:

| We acknowledge Czech Science Foundation projects nos 15-17102S, 17-11898S and 18-23597S.
Authors are also participating in COST Actions BM1309, CA1521 and bilateral exchange project
between Czech and Slovak Academy of Sciences, no. SAV-18-11. Vadym Sulimenko, Pavel Dráber
and Petra Vahalová are acknowledged for tubulin preparation.

On-chip microwave sensing of tubulin and its polymer

Ondrej Krivosudský^a, Daniel Havelka^a, Djamel Eddine Chafai, Michal Cifra^b

Institute of Photonics and Electronics of the Czech Academy of Sciences, Prague, 18200, Czechia

^aauthors contributed equally

^bcorresponding author, cifra@ufe.cz

Abstract

Microtubules are biologically ubiquitous, filamentous 25-nm diameter tube-like structures formed by reversible polymerization from protein sub-units – tubulin dimers. Since microtubules serve in essential cell functions such as cell division and intracellular transport and are one of major targets in cancer therapies, it is crucial to develop efficient methods for monitoring of the state of microtubule polymerization.

However, current methods for its monitoring require either fluorescence labeling or rely on light scattering measurement restricting the possibility of miniaturization and lab-on-chip integration, in contrast to electronic and high-frequency circuits. To alleviate the limitations of light-based microtubule monitoring, we designed a dedicated microwave chip with integrated microfluidics with sensing volume of 37 nL. Using the chip, for the first time, we demonstrate that state of polymerization of the tubulin to microtubules can be monitored using microwaves.

Our results contribute to novel label-free, microwave-based, on-chip methods for monitoring the state of microtubule cytoskeleton.

Keywords: dielectric spectroscopy, proteins, high-frequency biosensors, radiofrequency and microwave chips

1. Introduction

2 Cellular skeleton - cytoskeleton - is a network of protein-based fibers
3 which enable cell to perform its fundamental functions as motility, divi-
4 sion and transport of intracellular cargo. Microtubules are one of three

5 types of cytoskeleton fibers which are present virtually in every type of cell
6 (Mandelkow and Mandelkow, 1994). Microtubules are composed of protein
7 subunits, tubulin heterodimers, which reversibly polymerize (Nogales and
8 Alushin, 2012) to form a tube with 25-nm diameter and typical lengths from
9 few hundreds of nanometers to several tens of micrometers. Microtubule-
10 related malfunctions are also present neurodegenerative (Coedert et al., 1989;
11 Matamoros and Baas, 2016) and psychiatric (Matamoros and Baas, 2016;
12 Marchisella et al., 2016) diseases. One of the fundamental characteristics of
13 microtubule is its capability to be assembled from tubulin. The assembly
14 can be modulated by change of pH (Regula et al., 1981) addition of ions
15 (O'Brien et al., 1997), and various tubulin binding drugs (Churchill et al.,
16 2015) whereby therapeutic effects can be achieved. Therefore, it is impera-
17 tive to advance a variety of complementary methods to assess various aspects
18 of the microtubule properties and features including the state of polymeriza-
19 tion. The classical laboratory methods for monitoring microtubule assembly
20 (i.e. polymerization from tubulin) exploit turbidity (absorbance) measure-
21 ment using visible light spectrophotometers Mirigian et al. (2013). While
22 those methods work well in laboratory settings, they operate using rather
23 bulky optical devices which are limited in their possibility for miniaturiza-
24 tion to integrate them on lab-on-the-chip in the future. In contrast, electronic
25 and microwave devices can be readily miniaturized as demonstrated in large
26 scale production of plethora of wireless devices. Inspired by the preliminarily
27 data which were nevertheless limited to 1 GHz (Goddard and Whittier, 2006)
28 and to test the possibility to monitor the state of tubulin polymerization, we
29 design specific microwave chip operating in 1-50 GHz band based on copla-
30 nar waveguide with modified central conductor beneath microfluidic channel.
31 While several groups developed microwave chips for label-free biomolecule
32 (Abeyrathne et al., 2016a; Havelka et al., 2018) or cell analysis (Heileman
33 et al., 2013; Grenier et al., 2013; Meyne nee Haase et al., 2015; Abeyrathne
34 et al., 2016b; Bao et al., 2018), to our knowledge, it is for the first time that
35 microwave chip is used to analyze isolated subcellular components. Further-
36 more, the rigorous microwave design and measurement enables us to extract
37 permittivity of microtubule solutions for the first time.

38 2. Materials and methods

39 2.1. Fabrication

40 The fabrication of the sensor is based on standard microtechnological pro-
41 cesses. It may be divided in two main parts, which are: a) a chip manufactur-
42 ing and b) the polymer microfluidic channel elaboration and assembling. As
43 the substrate of proposed microwave sensor we used quartz glass purchased
44 from Technical Glass Products, Inc. with dimensions ($25.4 \times 25.4 \times 1$ mm³).
45 Micro-sized coplanar waveguide (CPW) and calibration lines used in this
46 work were fabricated by standard lift-off process with the mask-less direct
47 optical lithography. In brief, the slides were first spin-coated with 400 nm
48 of LOR lift-off resist (MicroChem Corp. LOR 5A lift-off resist), followed
49 by a 1.5 μ m thick layer of Shipley S1818 photoresist (Microposit[®] S1818TM
50 G2 positive photoresist). Softbake treatment in case of LOR was 200 °C
51 for 5 min and 120 °C for 2 min in case of S1818. The pattern was trans-
52 ferred by mask-less direct optical lithograph (MicroWriterML@2, Quantum
53 Design Inc.) with standard exposure dose 160 mJ/cm² @ 405 nm. Then it
54 was immediately developed in 30 mL of MF-319 developer (Microposit[®]) for
55 about 75 seconds with slow agitation. The sensor metallization after lithog-
56 raphy process consists of 5 nm layer of evaporated titanium as an adhesion
57 layer with 300 nm gold on a top. The evaporation was followed with lift-
58 off process by immersing into mr-Rem 700 remover solution (Micro resist
59 technology GmbH) for stripping of the resist. Afterwards, the slides were
60 thoroughly rinsed with acetone, ethanol and Millipore Q-water. Before final
61 use, the sensor was cleaned with UVO-Cleaner[®] 42-220 for additional 10 min.
62 The microchannel is fabricated from the elastomeric PDMS (Polydimethyl-
63 siloxane polymer) with the similar lithography process. First, the mold struc-
64 ture from SU-8 3050 negative photoresist (Micro resist technology GmbH)
65 is created in similar way as previously. The photoresist is spin-coated to
66 achieve 50 μ m thickness after 17 hours long soft-bake process at 65 °C. By
67 the same lithography maskless treatment the microfluidic channel pattern
68 is transferred (standard exposure dose = 1,810 mJ/cm² @ 375 nm). After
69 postbake procedure (65 °C for 5 min., 95 °C for 30 min. and 65 °C for
70 30 min), the pattern is developed for about 20 min in mr-Dev 600 developer,
71 rinsed with Isopropyl alcohol and gently dried with nitrogen. Mold is then
72 hardbaked at 100 °C for 10 min to make photoresist almost insoluble. Mi-
73 crochannel is finally created from PDMS polymer, which is mixed in 10 to
74 1 ratio (Base/Curing Agent, Dow Corning[®] 184 Silicone Elastomer) poured

75 on the mold, desiccated and solidified by curing (60 °C for 6 hours). It is
76 then gently peeled off from the mold and ready to use.

77 *2.2. Material characterization*

78 To correctly evaluate the complex permittivity of unknown liquid, the
79 material parameters (complex permittivity and surface impedance) of sensor
80 wafer and metallization had to be identified. We also identify the dielectric
81 function of PDMS through the whole frequency range of interest.
82 Dielectric function of quartz glass was extracted as follows. We used fab-
83 ricated calibration kit from our previous work, see (Havelka et al., 2018,
84 Fig. 3 H), as a sensor. The same Multiline-TRL (Thru-Reflect-Line) cali-
85 bration procedure (lines with $L = 1, 2, 4,$ and 8 mm; reflect short; thru) was
86 used to calibrate the Vector Network Analyzer ((VNA), Rohde & Schwarz®
87 ZVA67) in the frequency range 1 to 50 GHz. After calibration was performed
88 we positioned a quartz wafer onto middle of 24 mm line and evaluated the
89 transmission and reflection S-parameters. By using the similar method, (de-
90 scribed in (Havelka et al., 2018, Section 2.4.)) which is based on the use of
91 optimization algorithm in the CST Microwave Studio, we were able to ex-
92 tract dielectric function of the quartz glass material. Optimization algorithm
93 (Trust Region Framework) is able to extract unknown material parameters
94 by iteration approach and shift of complex permittivity of modelled glass.
95 Iteration process is stop by fulfilling the permittivity criteria at the desired
96 frequency point until scattering parameters of model and experimental one
97 are matched. Extracted values are enclosed in Fig. S3. Extracted points
98 were then fitted by polynomial function in CST Microwave Studio.
99 The another unknown to identify is the surface impedance of metallization.
100 To assess that, we again used CST Microwave Studio with Macro module
101 (Extract complex permittivity from measured S-parameters (broadband)).
102 This Macro enable to extract surface impedance from measured transmission
103 scattering parameter S_{21} of a transmission line section (Option - Extract from
104 measured propagation constant). As a transmission line section we measured
105 the 8 mm calibration line at our sensor (designated as Beatty 201712_3B) af-
106 ter Multiline-TRL calibration was performed. The reason to use the longest
107 line of our calibration standards is to achieve the highest robustness which is
108 increased with the length difference between the Thru calibration standard
109 and actual line. Then we model the 4 mm line which matched with the all
110 overall dimension of manufactured one with 300 nm of gold metallization.
111 The macro then by comparing propagation constant at desired frequency

112 points iterative changing and minimizing the difference between simulated
113 and measured parameters by changing the surface impedance of the gold
114 material. Extracted surface impedance of the gold metallization is presented
115 in Fig. S4.

116 As the last part of material characterization, dielectric function of PDMS
117 material was evaluated, see Fig. S5. We replicated the similar optimization
118 circle as with quartz glass. We used PDMS brick manufactured in the same
119 batch with the exact same procedure as a micro-channel, and placed it care-
120 fully in the middle of the 4 mm line (designated as LINE PDMS on the Beatty
121 201712_3B chip) sensor. Measured S-parameters were again used in the op-
122 timization procedure in CST Microwave Studio for matching the extraction
123 model. Advantage of using the same batch and manufacturing process in
124 case of extraction brick and microchannel is that we were also able to reduce
125 the error given by the strong dependency of a PDMS material parameters
126 on the curing temperature, curing length and another manufacturing steps
127 (Kachroudi et al. (2015)).

128 *2.3. Measurement with chip*

129 Before each measurement, vector network analyzer was calibrated using
130 Multiline-TRL method and our calibration kit on the chip (Reflect - Short,
131 Thru, Lines 1, 2, 4, and 8 mm). Then we positioned microchannel under
132 the microscope onto our sensing part. Calibration was verified by two tier
133 measurement in each experiment.

134 First, by using Beatty line with PDMS channel (see Fig. 1) in place and
135 evaluation of a ALSE (Average Least Square error) parameter (-60 dB was a
136 threshold line through the entire frequency range). It is visible from Fig. S6
137 that the ALSE between the real sensor and our model is below the -65 dB in
138 the the whole frequency range of interest. That means, that our extraction
139 procedure for material parameters together with geometrical dimensions are
140 extremely precisely matched.

141 Second, we employed so-called Thru test, which enables one to determine the
142 phase uncertainty of the measurement. It is evaluated as a phase difference
143 between Port 1 to Port 2 and vice versa. Results determine the threshold
144 value for material extraction algorithm. The Thru test results of both experi-
145 ments are presented in Fig. S7. The maximum phase deviation or uncertainty
146 is 0.2° at around 40 GHz.

147 Afterwards, setup with Beatty line (*Beatty line chip (201712_3B)*) was con-
148 nected to microfluidic tubes and syringe with a specimen. We injected slowly

149 the specimen (approximately 37 nL is volume of the sensing part, 50 μ L of the
 150 whole microfluidic system) into sensing area by a laboratory syringe pump
 151 and acquired S-parameters. Then by the using of syringe pump different
 152 part of the specimen was injected and parameters were saved again. The
 153 measurement of all solutions (pure water, BRB80 buffer, 5 mg/mL tubulin,
 154 and microtubule solution) have been repeated 16 times (8 times for 2 in-
 155 dependently prepared samples). The variability among measurements is in
 156 supplementary data, Fig. S8 and Fig. S9. The average of 32 S-parameter
 157 measurements was taken as the input into permittivity extraction. During
 158 the whole experiment, temperature, and humidity has been monitored and
 159 kept constant around 23°C as a prevention to spontaneous tubulin polymer-
 160 ization or other unknown biological effects. Variation in temperature and
 161 humidity can be seen in supplementary material in Fig. S1 for first experi-
 162 ment and in Fig. S2 for second one.

163 2.4. Permittivity extraction

164 Complex permittivity of the specimen was extracted in the following
 165 way. Our model of sensor in the CST Microwave Studio had all dimen-
 166 sions and material parameters corresponding to the those of the fabricated
 167 one (see Fig. S6). For the material parameters, previously extracted val-
 168 ues of quartz glass wafer, gold layer, and PDMS were used. Experimen-
 169 tally measured S-parameters were processed as $S_R^{Meas} = (S_{11} + S_{22})/2$ and
 170 $S_T^{Meas} = (S_{21} + S_{12})/2$ and then were compared with the calculated S-
 171 parameters (S_{11}^{Simul} and S_{21}^{Simul}) of model in the CST Microwave Studio. After
 172 that, an optimization algorithm (Trust Region Framework implemented in
 173 the CST Microwave Studio) as presented in section 2.2 was used again to keep
 174 shifting the specimen permittivity (ϵ'_{r2} and ϵ''_{r2}) until the two optimization
 175 goals for transmission parameter and one for reflection parameter were met
 176 at the same time. Optimization goals were (i) $||S_R^{Meas}| - |S_{11}^{Simul}|| < 0.002$,
 177 (ii) $||S_T^{Meas}| - |S_{21}^{Simul}|| < 0.002$, and (iii) $|\angle S_T^{Meas} - \angle S_{21}^{Simul}| < 0.5^\circ$. In
 178 the optimization algorithm, initial values of permittivity are set to a permit-
 179 tivity of Debye water model (Ellison et al. (1996): $\epsilon(0) = 79$, $\epsilon(\infty) = 6$).
 180 This procedure was repeated for essential number of frequency points. Thus,
 181 complex permittivity function of our unknown specimen was obtained.

182 2.5. Fitting of extracted permittivity points

183 The Cole-Davidson spectral function (Eq. 1), which is known for fitting
 184 the frequency dependence of complex dielectric permittivity of glycerol mix-

185 tures (Behrends et al., 2006; Puzenko et al., 2005), was used in all data
186 treatment. All points up to 50 GHz were used as an input to the data fitting
187 in MATLAB. Cole-Davidson equation can be described as:

$$\varepsilon^* = \varepsilon(\infty) + \frac{\Delta\varepsilon}{(1 + j\omega\tau)^\beta} + \frac{\sigma_{DC}}{j\omega\varepsilon_0} \quad (1)$$

188 where $\varepsilon(\infty)$ is permittivity at high frequency, $\Delta\varepsilon = \varepsilon(0) - \varepsilon(\infty)$ is the
189 dielectric increment, ω is angular frequency, τ is a relaxation time, $0 < \beta < 1$
190 is an empirical parameter referred to as a measure of asymmetrical relaxation
191 peak broadening, and j is imaginary unit ($j^2 = -1$). For parameter value of
192 $\beta = 1$ the Eq. 1 converge to well known Debye relationship. Permittivity of
193 free space is contained as ε_0 and the term $\sigma_{DC}/j\omega\varepsilon_0$ we added due to the
194 presence of an ionic DC conductivity σ_{DC} caused by free charge carriers of
195 salts included in our BRB80 buffer.

196 2.6. Tubulin preparation and assembly

197 Purified tubulin was provided by Dr. P. Draber lab (Institute of Molec-
198 ular Genetics of the Czech Academy of Sciences). Briefly, the isolation of
199 microtubule protein (MTP-2) was done from porcine brain by two tempera-
200 ture-dependent cycles of assembly and disassembly. The tubulin was stored
201 in BRB80 buffer (80 mM PIPES pH 6.8, 1 mM EGTA, and 1 mM MgCl_2)
202 supplemented with 0.1 mM GTP. Tubulin concentration was assessed by mea-
203 suring the absorbance at 280 nm using an extinction coefficient at 280 nm
204 of $115,000 \text{ M}^{-1}\text{cm}^{-1}$. The obtained tubulin was of high purity MTP2 > 95 -
205 98 % and stored in liquid nitrogen with a concentration of 22.6 mg/mL.
206 The microtubule polymerization was monitored by turbidimetry at 350 nm
207 and 37°C using a multimode microplate reader (Spark[®] TECAN, Austria)
208 equipped with temperature controller. The tubulin was assembled in BRB80
209 supplemented with GTP (1 mM) and glycerol (3.0 M) at final concentrations.
210 When polymerization plateau is reached, taxol was added at final concentra-
211 tion of 10 μM to insure the stability of microtubule during dielectric mea-
212 surement. All chemicals were purchased from Sigma Aldrich, Czechia. Detail
213 procedure of microtubules preparation was published in work of Dráberová
214 et al. (2010).

215 **3. Results and Discussion**

216 *3.1. Chip design and measurement setup*

217 Design of our chip is based on a coplanar waveguide located on the quartz
218 glass substrate with the dimensions as $24.5 \times 24.5 \times 1 \text{ mm}^3$ see Fig. 1 A. The
219 CPWs have a center electrode $200 \text{ }\mu\text{m}$ wide except under the microfluidic
220 channel, where the center electrode is $70 \text{ }\mu\text{m}$ wide. The gaps between center
221 and ground electrodes are $30 \text{ }\mu\text{m}$ wide except under the microfluidic channel,
222 where the gap is $95 \text{ }\mu\text{m}$ wide. The ground electrodes are $500 \text{ }\mu\text{m}$ wide. The
223 chip including (i) a calibration kit, (ii) a CPW for PDMS characterization,
224 and (iii) a CPW for the specimen measurement with the PDMS microfluidic
225 channel was fabricated using standard microtechnological processes (see more
226 in the section 2.1). We decided for Multiline-TRL calibration technique
227 (Rumiantsev et al., 2008; DeGroot et al., 2002; Marks, 1991) and designed
228 appropriate calibration kit (reflect - short, thru, lines 1, 2, 4, and 8 mm
229 length) in the frequency range from 1 to 50 GHz. The reference planes for the
230 vector network analyzer measurement are marked on the CPW structure as
231 depicted in the Fig. 1 A (down left). We electrically characterized the same
232 PDMS which was used as microfluidic channel using a CPW *Line PDMS*
233 and PDMS block with dimensions as $3 \times 7 \times 1.1 \text{ mm}^3$ (see more in the section
234 2.2). The sensing CPW called *Beatty line* is 4 mm long with $2.74 \times 7 \times 1 \text{ mm}^3$
235 PDMS block with channel on it. The PDMS block has 0.74 mm wide and
236 $50 \text{ }\mu\text{m}$ height microfluidic channel in the middle as you can see in the Fig. 1 B.

237 The measurement setup (see Fig. 1 C) was composed of two port vector
238 network analyzer (Rohde & Schwarz[®], ZVA67) connected through adapters
239 (CentricRF, C8135) to 50 GHz coaxial cables (MPI Corporation, MRC-50Q-
240 MF-800) and then to the 50 GHz probes (MPI Corporation, T50A-GSG0150)
241 mounted on the mechanical probe system (MPI Corporation, MPI TS150
242 with upgrade the RF MP60 micropositioners and Z10U-ITSS microscope).
243 The chip was put on auxiliary ceramic chuck, fixed by the vacuum, and was
244 under constant supervision by the microscope all the time. The PDMS block
245 with the microfluidic channel was fixed and pushed down to the chip by two
246 wire arms to avoid specimen leakage. Two microfluidic tubes (Hamilton,
247 TUB PTFE 1xHUB GA30x500mm) were used to deliver the specimens into
248 our microfluidic channel (approximately 37 nL is volume of the sensing part)
249 on the chip (see in detail of Fig. 1 C). The inlet tube was feed by the syringe
250 (BD Luer-LokTM 1-mL syringe, REF 309628) with the specimens. Precise
251 delivering of the specimen ensured XenoWorks[®] analog microinjector (Sut-

252 ter Instrument, BRI-213) fixed on the right sliding shelf. The outlet tube
 253 delivered the measured specimens to the 1.5 mL Eppendorf tubes fixed in
 254 the tube holder situated on the left sliding shelf.

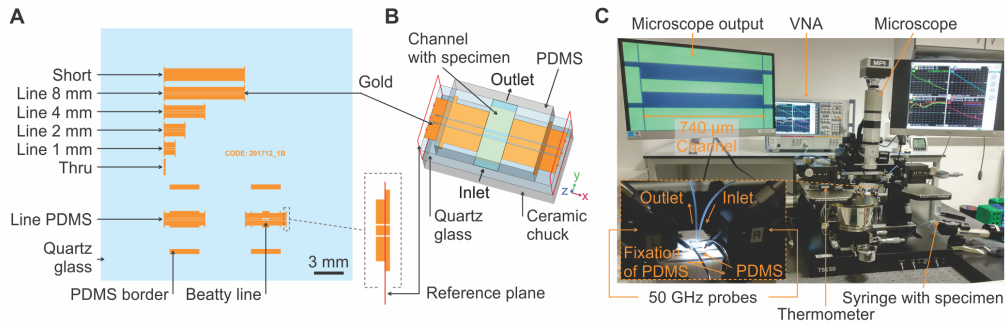


Figure 1: A) The chip includes Multiline TRL calibration kit (top), line for PDMS characterization (down left), and sensing Beatty line on the quartz glass substrate ($24.5 \times 24.5 \times 1$ mm³), B) 3D depiction of the Beatty line with the PDMS channel and a specimen in the channel, and C) The depiction of the measurement setup during measurement with the detail on probe connection to the Beatty line with PDMS channel (down left). The view on the channel during measurement is on the screen top left.

255 3.2. Microtubule polymerization

256 The formation of microtubules was verified by a standard turbidimetric
 257 measurements as shown in Fig. 2. In this figure, we provide the average ab-
 258 sorbance signal of three samples used for subsequent experiments. The first
 259 phase from Fig. 2 (represented by red curve) shows the typical polymerization
 260 absorbance curve where the maximum microtubules formation is reached af-
 261 ter 15 min at stable temperature 37°C. The second phase of the curve (green
 262 line) shows the absorbance when Taxol was added to insure microtubules
 263 stabilization. The absorbance signal was obviously decreased slightly due to
 264 the mechanical disturbance of microtubules during Taxol injection. The ver-
 265 ification of the stability of our microtubules during subsequent experiments,
 266 and their correlation to dielectric properties measurements is shown in blue
 267 curve of the Fig. 2. The blue curve represents the absorbance signal of the
 268 collected microtubules after the dielectric measurements in the chip that took
 269 place. The approximate temperature of the measurement was 23°C and ex-
 270 periment took about 30 min. This absorbance signal gives an evidence that
 271 the dielectric measurements are tightly related to stable microtubules.

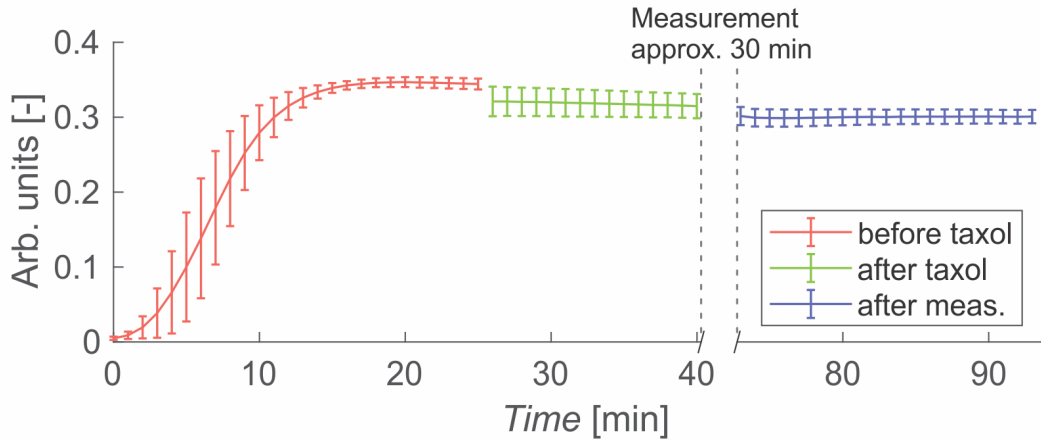


Figure 2: Polymerization curve of microtubules before taxol addition (red), after stabilization with taxol (green), and after on-chip measurements (blue) measured by TECAN Spark[®] multimode microplate reader.

3.3. Complex permittivity of tubulin and microtubule

The fabricated and verified sensor was used to measure S-parameters for extraction of the complex permittivity of a model biomolecular liquid. We were interested to examine the dielectric spectra of tubulin in BRB80 buffer solution and curious to see the impact of its polymerization into microtubule. Microtubule, assembled from $\alpha\beta$ -tubulin heterodimers, represent an essential biopolymer material which participates in critical cellular functions, such as cell division, and governs the transport of material within the cell. Complex permittivity of all solutions is showed in Fig. 3 and Fig. 4. For pure water a well-known Debye behavior of the dielectric function is observed, single relaxation process of water molecule tumbling at around 20 GHz connected with maximum losses demonstrated in imaginary part of the complex permittivity.

Completely another situation is observed in buffer experiment. To keep protein in its nature environment BRB80 buffer containing basic salts (see detailed description in Subsection 2.6) have to be used. We also added glycerol (3.0 M final concentration in BRB80 buffer) to enhance the microtubule polymerization. Therefore before use of biological samples, we have measured dielectric response of BRB80 buffer solution.

The extracted spectrum represents the well known water-glycerol behavior,

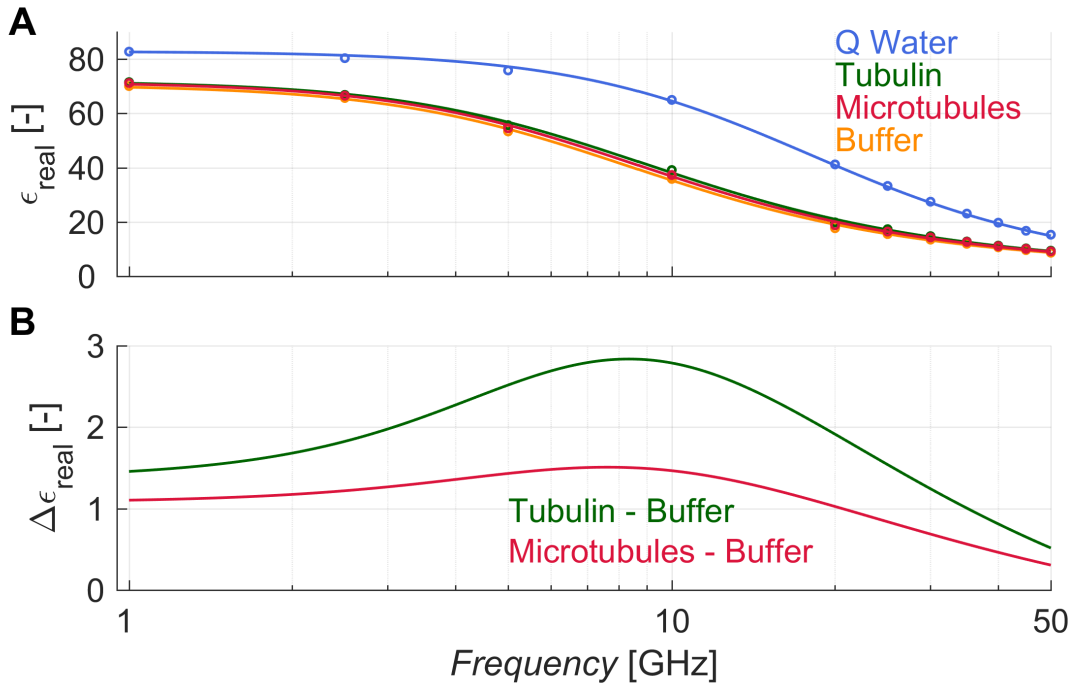


Figure 3: A) Real part of relative complex permittivity of a liquid specimens obtained using our sensor after fitting (line) by Cole-Davidson equation. Blue curve represent Q - Water, Green - Tubulin solution, Red - Microtubule solution, and Orange curve represent buffer solution. The extracted data are represented by circles and their fitting by line, B) Difference between imaginary part of tubulin and buffer in green and of microtubules and buffer in red calculated from the fitted data.

293 with a shifted relaxation time to lower frequency at around 8 GHz, which
 294 can be modeled with the Cole-Davidson distribution (Hayashi et al., 2005).
 295 This shift is strongly dependent on the water/glycerol concentration and can
 296 be explained through the cooperative effect in dielectric orientation of groups
 297 containing molecules of both kind (McDuffie et al., 1962) and changes of vis-
 298 cosity.

299

300 On the other hand, after diluting tubulin in buffer with a final concentra-
 301 tion of 5 mg/mL, dielectric function manifests a slightly different dependency.
 302 Different behavior is illustrated in both real and imaginary part of the dielec-
 303 tric spectrum. The relaxation frequency is shifted to approximately of 9 GHz
 304 (see Fig. 5) with corresponding relaxation time of 17.5 ps (see Fig. 6). We also
 305 compare directly the absolute value of permittivity of tubulin/microtubules

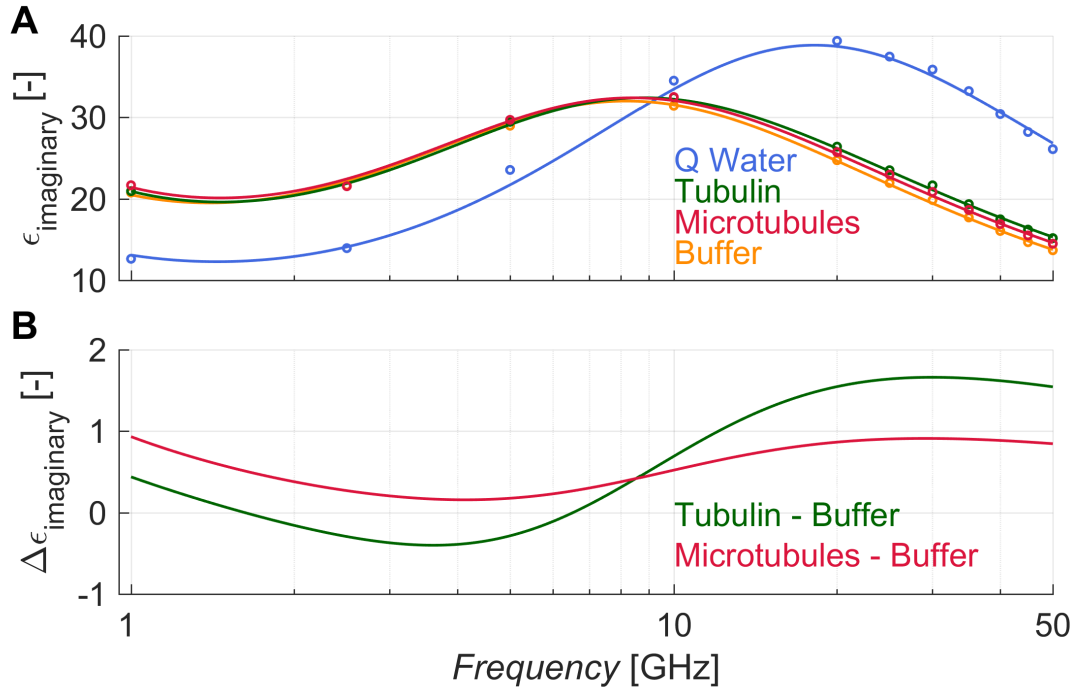


Figure 4: A) Imaginary part of relative complex permittivity of a liquid specimens obtained using our sensor after fitting by Cole-Davidson equation. Blue curve represent Q Water, Green - Tubulin solution, Red - Microtubule solution, and Orange curve represent buffer solution. The extracted data are represented by circles and their fitting by line, B) Difference between imaginary part of tubulin and buffer in green and of microtubules and buffer in red calculated from the fitted data.

306 with the BRB80 buffer - see data presented in Fig. 7. After the polymeriza-
 307 tion, first the real part of the permittivity increased in the whole frequency
 308 range. On the other hand, the maximum value of dielectric loss represented
 309 by imaginary part of dielectric spectra indicates that the dielectric losses are
 310 similar to those of tubulin. Nevertheless there exists a significant frequency
 311 shift, corresponding with change of relaxation time of whole solution. To
 312 our best knowledge, change manifested in the imaginary part of spectra (in-
 313 creased relaxation time) is due to increased viscosity after polymerization of
 314 tubulin to microtubules. It is not the consequence of changing the concen-
 315 tration of the salts of glycerol since they are the same. What we actually
 316 did is that during the growth period, protein structure (globular structure)
 317 is changing into microtubules (rod like structures) which likely restricts ro-
 318 tational mobility of the solvent molecules. That might be also prevailed in

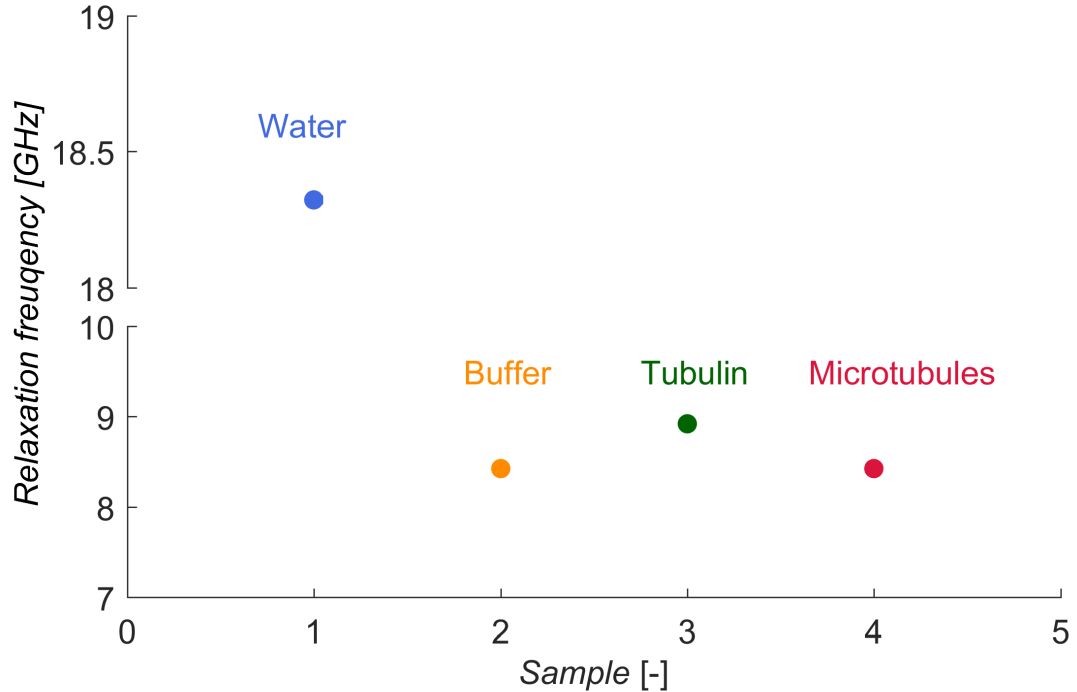


Figure 5: Relaxation frequency of a liquid specimen obtained using our sensor after fitting by Cole-Davidson equation. Blue dot represent Q - Water, Green - tubulin solution, Red - microtubule solution. Orange dot represents buffer solution.

319 different water/microtubule interaction than with water/protein.

320

321 In summary the design of CPW with structured sensing area has been al-
 322 ready proposed before by various authors (Grenier et al., 2013; Chen et al.,
 323 2013). However, they were limited by two main factors. First, we overcome
 324 two tier calibration problem by implementing the calibration kit directly with
 325 sensor on one chip. This eliminates the need to use the external calibration
 326 kit (mostly supplied by manufacturer of the probe station) on different sub-
 327 strate, metallization, and length of calibration lines (i.e. different frequency
 328 range to calibrate). By using our on-chip kit we are able to calibrate the
 329 whole platform on the substrate, with the same metallization which enable
 330 us to achieve unprecedented precision and calibration robustness.

331 Second, due to implementation of 4 mm sensor line we were also able to fully
 332 extract the permittivity of the PDMS polymer in the whole frequency range.

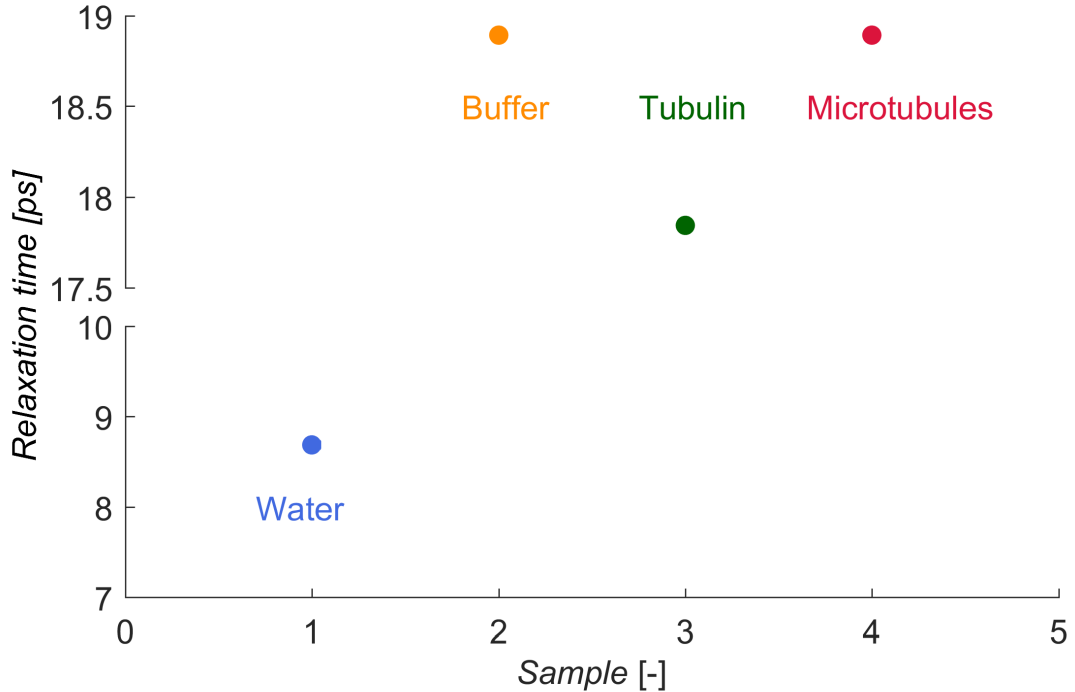


Figure 6: Relaxation time of a liquid specimen obtained using our sensor after fitting by Cole-Davidson equation. Blue dot represent Q - Water, Green - tubulin solution, Red - microtubule solution. Orange dot represents buffer solution.

333 Full knowledge of materials characteristic and using model in CST Microwave
 334 Studio enable to extract the complex permittivity of the sample under test
 335 with high precision without any a priori knowledge about the sample itself.
 336 We were able to not only to distinguish the change of dielectric properties of
 337 the sample under test, lowered the specimen volume required for the experi-
 338 ment but also assign the changes to real parameters represented by complex
 339 dielectric function to compared to these recent developments.

340 4. Conclusion

341 In this work, we started with (i) fundamental design of planar microwave
 342 sensor with implemented on wafer calibration kit, then created (ii) accurate
 343 design model of the sensor in CST Microwave studio to give estimation of the
 344 sensor performance (iii) followed by fabrication and testing the whole system

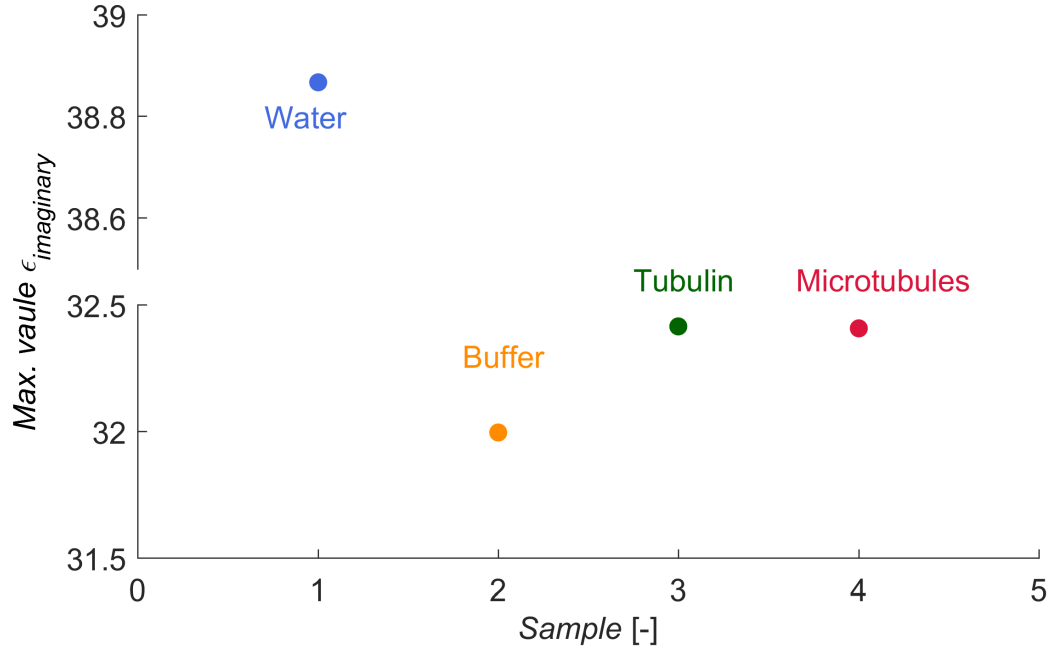


Figure 7: Maximum value of imaginary part of complex permittivity. Blue dot represent Q - Water, Green - tubulin solution, Red - microtubule solution. Orange dot represent buffer solution.

345 with calibration kit.

346 Accurate modeling enable us to perform (iv) material characterization which
 347 led to assessment of (v) experimentally obtained complex permittivity of
 348 biological solutions (vi) and interpret the permittivity change after tubulin
 349 polymerization into microtubules.

350 In summary, we described a whole design the sensor which addresses not
 351 only the low volume low concentration sensing ability but also dielectric
 352 spectroscopy of biomolecules. Here we chose coplanar waveguide-based chip
 353 topology with calibration kit implemented on the same wafer and tubulin as
 354 a protein under investigation. We believe that both the specific chip design
 355 we developed here as well as the experimental results will allow identifying
 356 and tracking biological processes such as as protein polymerization from a
 357 novel perspective.

358 **Author contributions statement**

359 Contribution roles according to CRediT:

360 https://dictionary.casrai.org/Contributor_Roles:

361 **Conceptualization:** Michal Cifra, Daniel Havelka, Ondrej Krivosudský

362 **Data curation:** Ondrej Krivosudský, Daniel Havelka, Djamel Eddine Chafai
363 (supporting)

364 **Formal analysis:** Ondrej Krivosudský, Daniel Havelka, Michal Cifra (sup-
365 porting), Djamel Eddine Chafai (supporting)

366 **Funding acquisition:** Michal Cifra

367 **Investigation:** Ondrej Krivosudský, Daniel Havelka, Michal Cifra (support-
368 ing), Djamel Eddine Chafai (supporting)

369 **Methodology:** Ondrej Krivosudský, Daniel Havelka, Djamel Eddine Chafai
370 (supporting)

371 **Project administration:** Michal Cifra

372 **Resources:** Michal Cifra, Vadym Sulimenko (supporting), Pavel Dráber
373 (supporting), Petra Vahalová (supporting)

374 **Software:** Ondrej Krivosudský, Daniel Havelka

375 **Supervision:** Daniel Havelka, Ondrej Krivosudský, Michal Cifra

376 **Validation:** Michal Cifra

377 **Visualization:** Daniel Havelka (lead), Ondrej Krivosudský (supporting)

378 **Writing original draft:** Ondrej Krivosudský (lead), Michal Cifra (sup-
379 porting), Daniel Havelka (supporting), Djamel Eddine Chafai (supporting)

380 **Writing review & editing:** Ondrej Krivosudský, Michal Cifra, Daniel
381 Havelka, Djamel Eddine Chafai

382 **5. Conflict of interest**

383 The authors declare that they have no competing interests.

384 **6. Acknowledgements**

385 We acknowledge Czech Science Foundation projects nos 15-17102S, 17-
386 11898S and 18-23597S. Authors are also participating in COST Actions
387 BM1309, CA1521 and bilateral exchange project between Czech and Slo-
388 vak Academy of Sciences, no. SAV-18-11. Vadym Sulimenko, Pavel Dráber
389 and Petra Vahalová are acknowledged for tubulin preparation.

390 **7. Appendix A. Supplementary data**

391 **References**

- 392 Abeyrathne, C. D., Huynh, D. H., Lee, T. T., Nguyen, T. C., Nasr, B.,
393 Chana, G., Skafidas, E., May 2016a. GFAP Antibody Detection Using
394 Interdigital Coplanar Waveguide Immunosensor. *IEEE Sensors Journal*
395 16 (9), 2898–2905.
- 396 Abeyrathne, C. D., Huynh, D. H., Mcintire, T. W., Nguyen, T. C., Nasr, B.,
397 Zantomio, D., Chana, G., Abbott, I., Choong, P., Catton, M., Skafidas, E.,
398 2016b. Lab on a chip sensor for rapid detection and antibiotic resistance
399 determination of *Staphylococcus aureus*. *The Analyst* 141 (6), 1922–1929.
- 400 Bao, X., Ocket, I., Crupi, G., Schreurs, D., Bao, J., Kil, D., Puers, B.,
401 Nauwelaers, B., Mar. 2018. A Planar One-Port Microwave Microfluidic
402 Sensor for Microliter Liquids Characterization. *IEEE Journal of Electro-*
403 *magnetics, RF and Microwaves in Medicine and Biology* 2 (1), 10–17.
- 404 Behrends, R., Fuchs, K., Kaatze, U., Hayashi, Y., Feldman, Y., 2006. Dielec-
405 tric properties of glycerol/water mixtures at temperatures between 10 and
406 50°C. *The Journal of Chemical Physics* 124 (14), 144512.
- 407 Chen, T., Artis, F., Dubuc, D., Fournié, J., Poupot, M., Grenier, K., June
408 2013. Microwave biosensor dedicated to the dielectric spectroscopy of a
409 single alive biological cell in its culture medium. In: 2013 IEEE MTT-S
410 International Microwave Symposium Digest (MTT). pp. 1–4.
- 411 Churchill, C. D. M., Klobukowski, M., Tuszynski, J. A., Nov. 2015. Eluci-
412 dating the Mechanism of Action of the Clinically Approved Taxanes: A
413 Comprehensive Comparison of Local and Allosteric Effects. *Chemical Bi-*
414 *ology & Drug Design* 86 (5), 1253–1266.
- 415 Coedert, M., Spillantini, M. C., Rutherford, D., Crowther, R. A., 1989. Mul-
416 tiple Isoforms of Human Microtubule-Associated Protein Tau: Sequences
417 and localization in Neurofibrillah Tangles of Alzheimer’s Disease. *Neuron*
418 3, 519–26.
- 419 DeGroot, D. C., Jargon, J. A., Marks, R. B., 2002. Multiline trl revealed. In:
420 60th ARFTG Conference Digest. pp. 131–155.

- 421 Dráberová, E., Sulimenko, V., Sulimenko, T., Böhm, K. J., Dráber, P., 2010.
422 Recovery of tubulin functions after freeze-drying in the presence of tre-
423 halose. *Analytical Biochemistry* 397 (1), 67–72.
- 424 Ellison, W., Lamkaouchi, K., Moreau, J.-M., 1996. Water: a dielectric refer-
425 ence. *Journal of Molecular Liquids* 68 (2), 171–279.
- 426 Goddard, G., Whittier, J. E., Mar. 2006. Biomolecules as nanomaterials:
427 interface characterization for sensor development. p. 617206.
428 URL [http://proceedings.spiedigitallibrary.org/proceeding.](http://proceedings.spiedigitallibrary.org/proceeding.aspx?doi=10.1117/12.658771)
429 [aspx?doi=10.1117/12.658771](http://proceedings.spiedigitallibrary.org/proceeding.aspx?doi=10.1117/12.658771)
- 430 Grenier, K., Dubuc, D., Chen, T., Artis, F., Chretiennot, T., Poupot, M.,
431 Fournié, J., May 2013. Recent advances in microwave-based dielectric spec-
432 troscopy at the cellular level for cancer investigations. *IEEE Transactions*
433 *on Microwave Theory and Techniques* 61 (5), 2023–2030.
- 434 Havelka, D., Krivosudský, O., Průša, J., Cifra, M., 2018. Rational design of
435 sensor for broadband dielectric spectroscopy of biomolecules. *Sensors and*
436 *Actuators B: Chemical* 273, 62–69.
- 437 Hayashi, Y., Puzenko, A., Balin, I., Ryabov, Y. E., Feldman, Y., 2005. Relax-
438 ation dynamics in glycerol water mixtures. 2. mesoscopic feature in water
439 rich mixtures. *The Journal of Physical Chemistry B* 109 (18), 9174–9177,
440 pMID: 16852092.
- 441 Heileman, K., Daoud, J., Tabrizian, M., Nov. 2013. Dielectric spectroscopy
442 as a viable biosensing tool for cell and tissue characterization and analysis.
443 *Biosensors and Bioelectronics* 49, 348–359.
- 444 Kachroudi, A., Basrour, S., Rufer, L., Sylvestre, A., Jomni, F., 2015. Dielec-
445 tric properties modelling of cellular structures with pdms for micro-sensor
446 applications. *Smart Materials and Structures* 24 (12), 125013.
- 447 Mandelkow, E., Mandelkow, E.-M., 1994. Microtubule structure. *Current*
448 *Opinion in Structural Biology* 4 (2), 171–179.
- 449 Marchisella, F., Coffey, E. T., Hollos, P., Oct. 2016. Microtubule and micro-
450 tubule associated protein anomalies in psychiatric disease: MAP Anoma-
451 lies in Psychiatric Disease. *Cytoskeleton* 73 (10), 596–611.

- 452 Marks, R. B., 1991. A multiline method of network analyzer calibration.
453 IEEE Transactions on Microwave Theory and Techniques 39 (7), 1205–
454 1215.
- 455 Matamoros, A. J., Baas, P. W., Sep. 2016. Microtubules in health and de-
456 generative disease of the nervous system. Brain Research Bulletin 126,
457 217–225.
- 458 McDuffie, G. E., Quinn, R. G., Litovitz, T. A., 1962. Dielectric properties of
459 glycerol water mixtures. The Journal of Chemical Physics 37 (2), 239–242.
- 460 Meyne nee Haase, N., Fuge, G., Trieu, H. K., Zeng, A.-P., Jacob, A. F.,
461 Oct. 2015. Miniaturized Transmission-Line Sensor for Broadband Dielec-
462 tric Characterization of Biological Liquids and Cell Suspensions. IEEE
463 Transactions on Microwave Theory and Techniques 63 (10), 3026–3033.
- 464 Mirigian, M., Mukherjee, K., Bane, S. L., Sackett, D. L., 2013. Measurement
465 of In Vitro Microtubule Polymerization by Turbidity and Fluorescence.
466 In: Methods in Cell Biology. Vol. 115. Elsevier, pp. 215–229.
467 URL [http://linkinghub.elsevier.com/retrieve/pii/
468 B9780124077577000141](http://linkinghub.elsevier.com/retrieve/pii/B9780124077577000141)
- 469 Nogales, E., Alushin, G., 2012. 4.6 Tubulin and Microtubule Structure:
470 Mechanistic Insights into Dynamic Instability and Its Biological Rele-
471 vance. In: Comprehensive Biophysics. Elsevier, pp. 72–92.
472 URL [http://linkinghub.elsevier.com/retrieve/pii/
473 B9780123749208004070](http://linkinghub.elsevier.com/retrieve/pii/B9780123749208004070)
- 474 O’Brien, E. T., Salmon, E., Erickson, H. P., 1997. How calcium causes mi-
475 crotubule depolymerization. Cell Motility and the Cytoskeleton 36 (2),
476 125–135.
- 477 Puzenko, A., Hayashi, Y., Ryabov, Y. E., Balin, I., Feldman, Y., Kaatze,
478 U., Behrends, R., 2005. Relaxation dynamics in glycerol water mixtures:
479 I. glycerol-rich mixtures. The Journal of Physical Chemistry B 109 (12),
480 6031–6035, pMID: 16851659.
- 481 Regula, C. S., Berlin, R. D., others, 1981. Microtubule assembly and disas-
482 sembly at alkaline pH. The Journal of cell biology 89 (1), 45–53.

483 Rumiantsev, A., Sweeney, S. L., Corson, P. L., 2008. Comparison of on-wafer
484 multiline trl and lrm+ calibrations for rf cmos applications. In: Microwave
485 Measurement Symposium, 2008 72nd ARFTG. IEEE, pp. 132–136.

7 | RESULTS

Results of the research presented in this thesis were published in scientific journals and conference proceedings (see the list of author's publications). The core of the dissertation consists of three main parts [Sections 4, 5, and 6] and one paper [A] in the Appendix. Full bibliographic citation, the contribution of the candidate, and acknowledgments are stated at the beginning of each section.

First Section 4 describes the interaction of electromagnetic radiation with "nano-rod" like structures. The resonant frequency, fluid interaction and consequent quality factor of vibrations were calculated. The reported results suggest that mechanical vibrations of nano-structures are in most cases heavily damped.

The second part is fully focused on the high-frequency dielectric properties of tubulin. We were able to (i) calculate the refractive index based on the well-established theory and (ii) verify the theory with experiment. The result revealed the refractive index of the tubulin is $n = 1.64$ at wavelength @ 589 nm and 25 °C, that is in a good match with our theory. The main implication of our finding is that (i) interaction distance of the electrostatic forces within microtubules and (ii) electronic dipole-dipole coupling are enhanced.

Section 6 presents the result of dielectric spectroscopy of tubulin and microtubule sample. This enables us for the first time to observe the impact of the tubulin polymerization on dielectric properties. This observation was possible due to the unique design of our microwave sensor and given calibration technique. The results demonstrate the existence of a change in both real and imaginary part of complex permittivity during tubulin polymerization. These changes are also connected with a shift in relaxation frequency peak of a whole system. In other words, we believe that the polymerization process of tubulin affects the solvent through the changes in the interaction with solvent molecules. The polymerized system displays higher real part of the relative permittivity and increased relaxation time. The application of such a system can serve as a prospective way of tubulin polymerization monitoring.

8 | CONCLUSIONS

8.1 CONTRIBUTION OF THE DISSERTATION

This thesis has provided a novel theoretical analysis of the interaction of the electromagnetic field with "rod-like" nanoresonators. It estimated the conditions for possible resonances and gave an estimate of experimental verification. Then we analyzed the high-frequency permittivity and polarizability of tubulin and microtubule. Our experimental findings were correlated with a solid theory which relies on the amino acid composition of the protein. Then we presented for the first time the dielectric spectra of tubulin solution and impact of tubulin polymerization on the whole system. We were mainly interested in observing the difference in a relaxation frequency shift of buffer. That might be used as an indicator for tubulin polymerization as a comparative technique to currently used optical absorbance measurement.

8.2 FUTURE DIRECTIONS

Results presented in this thesis are, more or less, proved by theory and experimental evidence. The next steps might follow these directions:

- | Design of highly sensitive (resonant) sensor to perform live "imaging" of tubulin polymerization. Resonant structure would be used as a polymerization sensor.
- | Characterization of tubulin and microtubule properties on radio frequencies and verification of the predictions obtained using the presented model. Observation of relaxation frequency of tubulin protein might be observable.

In conclusion, the goals of the thesis summarized in Section 3 were fulfilled in candidate's papers [A1-A3].

BIBLIOGRAPHY

- [1] E. H. Kellogg, N. M. A. Hejab, S. Poepsel, K. H. Downing, F. DiMaio, and E. Nogales, “Near-atomic model of microtubule-tau interactions,” *Science*, vol. 360, no. 6394, pp. 1242–1246, 2018. [Online]. Available: <http://science.sciencemag.org/content/360/6394/1242>
- [2] P. Debye, “Part I. Dielectric constant. Energy absorption in dielectrics with polar molecules,” *Transactions of the Faraday Society*, vol. 30, pp. 679–684, 1934. [Online]. Available: <http://pubs.rsc.org/en/content/articlepdf/1934/ft/tf9343000679>
- [3] J. L. Oncley, “The Investigation of Proteins by Dielectric Measurements.” *Chemical Reviews*, vol. 30, no. 3, pp. 433–450, 1942. [Online]. Available: <http://pubs.acs.org/doi/abs/10.1021/cr60097a008>
- [4] J. D. Ferry and J. L. Oncley, “Studies of the dielectric properties of protein solutions. II. The water-soluble proteins of normal horse serum,” *Journal of the American Chemical Society*, vol. 60, no. 5, pp. 1123–1132, 1938. [Online]. Available: <http://pubs.acs.org/doi/abs/10.1021/ja01272a036>
- [5] J. G. Kirkwood, “The Dielectric Polarization of Polar Liquids,” *The Journal of Chemical Physics*, vol. 7, no. 10, pp. 911–919, Oct. 1939. [Online]. Available: <http://aip.scitation.org/doi/10.1063/1.1750343>
- [6] T. Vignaud, L. Blanchoin, and M. Théry, “Directed cytoskeleton self-organization,” *Trends in Cell Biology*, vol. 22, no. 12, pp. 671–682, 2012. [Online]. Available: <http://www.sciencedirect.com/science/article/pii/S096289241200164X>
- [7] D. Portran, J. Gaillard, M. Vantard, and M. Théry, “Quantification of map and molecular motor activities on geometrically controlled microtubule networks,” *Cytoskeleton*, vol. 70, no. 1, pp. 12–23, 2013. [Online]. Available: <https://onlinelibrary.wiley.com/doi/abs/10.1002/cm.21081>
- [8] C. Aumeier, L. Schaedel, J. Gaillard, K. John, L. Blanchoin, and M. Théry, “Self-repair promotes microtubule rescue,” *Nature Cell Biology*, vol. 18, no. 10, pp. 1054–1064, Sep. 2016. [Online]. Available: <http://www.nature.com/doi/abs/10.1038/ncb3406>
- [9] L. Schaedel, K. John, J. Gaillard, M. V. Nachury, L. Blanchoin, and M. Théry, “Microtubules self-repair in response to mechanical stress,” *Nature Materials*, vol. 14, no. 11, pp. 1156–1163, Sep. 2015. [Online]. Available: <http://www.nature.com/doi/abs/10.1038/nmat4396>
- [10] S. Sahu, S. Ghosh, K. Hirata, D. Fujita, and A. Bandyopadhyay, “Multi-level memory-switching properties of a single brain microtubule,” *Applied Physics Letters*, vol. 102, no. 12, p. 123701, mar 2013. [Online]. Available: <http://aip.scitation.org/doi/10.1063/1.4793995>
- [11] S. Sahu, S. Ghosh, B. Ghosh, K. Aswani, K. Hirata, D. Fujita, and A. Bandyopadhyay, “Atomic water channel controlling remarkable properties of a single brain microtubule: Correlating single protein to its supramolecular assembly,” *Biosensors and Bioelectronics*, vol. 47, pp. 141–148, sep 2013. [Online]. Available: <http://linkinghub.elsevier.com/retrieve/pii/S0956566313001590>
- [12] C. Janke and J. Chloë Bulinski, “Post-translational regulation of the microtubule cytoskeleton: mechanisms and functions,” *Nature Reviews Molecular Cell Biology*, vol. 12, no. 12, pp. 773–786, Nov. 2011. [Online]. Available: <http://www.nature.com/doi/abs/10.1038/nrm3227>

- [13] M. Sirajuddin, L. M. Rice, and R. D. Vale, "Regulation of microtubule motors by tubulin isotypes and post-translational modifications," *Nature Cell Biology*, vol. 16, p. 335, Mar. 2014. [Online]. Available: <http://dx.doi.org/10.1038/ncb2920>
- [14] B. Alberts, A. Johnson, J. Lewis, M. Raff, K. Roberts, and P. Walter, *Molecular biology of the cell*, 5th ed. Garland Science, Taylor & Francis Group, 2008.
- [15] C. E. Felder, J. Prilusky, I. Silman, and J. L. Sussman, "A server and database for dipole moments of proteins," *Nucleic Acids Research*, vol. 35, no. Web Server, pp. W512–W521, May 2007. [Online]. Available: <http://nar.oxfordjournals.org/lookup/doi/10.1093/nar/gkm307>
- [16] J. Tuszyński, J. Brown, E. Crawford, E. Carpenter, M. Nip, J. Dixon, and M. Sataric, "Molecular dynamics simulations of tubulin structure and calculations of electrostatic properties of microtubules," *Mathematical and Computer Modelling*, vol. 41, no. 10, pp. 1055–1070, 2005. [Online]. Available: <http://www.sciencedirect.com/science/article/pii/S0895717705001652>
- [17] P. M. Vassilev, R. T. Dronzine, M. P. Vassileva, and G. A. Georgiev, "Parallel arrays of microtubules formed in electric and magnetic fields," *Bioscience Reports*, vol. 2, no. 12, pp. 1025–1029, 1982. [Online]. Available: <http://www.bioscirep.org/content/2/12/1025>
- [18] M. J. Ortner, M. J. Galvin, and R. D. Irwin, "The effect of 2450-MHz microwave radiation during microtubular polymerization in vitro," *Radiation Research*, vol. 93, no. 2, pp. 353–363, 1983. [Online]. Available: <http://www.jstor.org/stable/3575991>
- [19] J. E. Whittier and G. R. Goddard, "Microtubule structural dynamics measured with impedance spectroscopy," *The FASEB Journal*, vol. 20, no. 4, pp. A492–A492, 2006.
- [20] R. Ramalho, H. Soares, and L. Melo, "Microtubule behavior under strong electromagnetic fields," *Materials Science and Engineering: C*, vol. 27, no. 5-8, pp. 1207–1210, Sep. 2007. [Online]. Available: <http://linkinghub.elsevier.com/retrieve/pii/S0928493106003547>
- [21] M. Uppalapati, Y.-M. Huang, T. N. Jackson, and W. O. Hancock, "Microtubule Alignment and Manipulation Using AC Electrokinetics," *Small*, vol. 4, no. 9, pp. 1371–1381, Sep. 2008. [Online]. Available: <http://doi.wiley.com/10.1002/sml.200701088>
- [22] L. Agrawal, S. Sahu, S. Ghosh, T. Shiga, D. Fujita, and A. Bandyopadhyay, "Inventing atomic resolution scanning dielectric microscopy to see a single protein complex operation live at resonance in a neuron without touching or adulterating the cell," *Journal of Integrative Neuroscience*, vol. 15, pp. 1–28, 01 2017.
- [23] O. Kučera and D. Havelka, "Mechano – electrical vibrations of microtubules – Link to subcellular morphology." *Biosystems*, vol. 109, no. 3, pp. 346–355, 2012. [Online]. Available: <http://dblp.uni-trier.de/db/journals/biosystems/biosystems109.html#KuceraH12>
- [24] D. Havelka, M. A. Deriu, M. Cifra, and O. Kučera, "Deformation pattern in vibrating microtubule: Structural mechanics study based on an atomistic approach," *Scientific reports*, vol. 7, no. 1, p. 4227, 2017.
- [25] A. Barth, "Infrared spectroscopy of proteins," *Biochimica et Biophysica Acta (BBA) - Bioenergetics*, vol. 1767, no. 9, pp. 1073–1101, 2007. [Online]. Available: <http://www.sciencedirect.com/science/article/pii/S0005272807001375>
- [26] D. Havelka, M. Cifra, O. Kučera, J. Pokorný, and J. Vrba, "High-frequency electric field and radiation characteristics of cellular microtubule network," *Journal of Theoretical Biology*, vol. 286, pp. 31–40, 2011. [Online]. Available: <http://www.sciencedirect.com/science/article/pii/S0022519311003511>
- [27] J. Pokorný, "Viscous effects on polar vibrations in microtubules," *Electromagnetic Biology and Medicine*, vol. 22, no. 1, pp. 15–29, 2003. [Online]. Available: <http://informahealthcare.com/doi/abs/10.1081/JBC-120020349>

- [28] J. Pokorný, J. Hašek, and F. Jelínek, “Endogenous electric field and organization of living matter,” *Electromagnetic Biology and Medicine*, vol. 24, no. 3, pp. 185–197, 2005. [Online]. Available: <http://dx.doi.org/10.1080/15368370500379566>
- [29] K. R. Foster and J. W. Baish, “Viscous damping of vibrations in microtubules,” *Journal of Biological Physics*, vol. 26, no. 4, pp. 255–260, 2000.
- [30] T. J. Craddock, C. Beauchemin, and J. A. Tuszyński, “Information processing mechanisms in microtubules at physiological temperature: Model predictions for experimental tests,” *Biosystems*, vol. 97, no. 1, pp. 28–34, 2009.
- [31] T. J. A. Craddock, D. Friesen, J. Mane, S. Hameroff, and J. A. Tuszyński, “The feasibility of coherent energy transfer in microtubules,” *Journal of The Royal Society Interface*, vol. 11, no. 100, 2014.
- [32] S. Hameroff, “Quantum walks in brain microtubules – a biomolecular basis for quantum cognition?” *Topics in cognitive science*, vol. 6, no. 1, pp. 91–97, 2014.
- [33] J. Wyman, “Studies on the dielectric constant of protein solutions,” *Journal of Biological Chemistry*, vol. 90, no. 2, pp. 443–476, 1931.
- [34] J. Wyman Jr and T. L. McMeekin, “The dielectric constant of solutions of amino acids and peptides,” *Journal of the American Chemical Society*, vol. 55, no. 3, pp. 908–914, 1933. [Online]. Available: <http://pubs.acs.org/doi/abs/10.1021/ja01330a006>
- [35] L. Onsager, “Electric moments of molecules in liquids,” *Journal of the American Chemical Society*, vol. 58, no. 8, pp. 1486–1493, 1936. [Online]. Available: <http://pubs.acs.org/doi/abs/10.1021/ja01299a050>
- [36] J. Wyman Jr, “Polarization and dielectric constant of liquids,” *Journal of the American Chemical Society*, vol. 58, no. 8, pp. 1482–1486, 1936. [Online]. Available: <http://pubs.acs.org/doi/abs/10.1021/ja01299a049>
- [37] J. G. Kirkwood and J. B. Shumaker, “The influence of dipole moment fluctuations on the dielectric increment of proteins in solution,” *Proceedings of the National Academy of Sciences*, vol. 38, no. 10, pp. 855–862, 1952.
- [38] T. L. McMeekin, M. Wilensky, and M. L. Groves, “Refractive indices of proteins in relation to amino acid composition and specific volume,” *Biochemical and Biophysical Research Communications*, vol. 7, no. 2, pp. 151–156, 1962.
- [39] R. J. Usselman, C. Chavarriaga, P. R. Castello, M. Procopio, T. Ritz, E. A. Dratz, D. J. Singel, and C. F. Martino, “The Quantum Biology of Reactive Oxygen Species Partitioning Impacts Cellular Bioenergetics,” *Scientific Reports*, vol. 6, p. 38543, Dec. 2016. [Online]. Available: <http://www.nature.com/articles/srep38543>
- [40] S. A. Stanley, L. Kelly, K. N. Latcha, S. F. Schmidt, X. Yu, A. R. Nectow, J. Sauer, J. P. Dyke, J. S. Dordick, and J. M. Friedman, “Bidirectional electromagnetic control of the hypothalamus regulates feeding and metabolism,” *Nature*, vol. 531, no. 7596, pp. 647–650, Mar. 2016. [Online]. Available: <http://www.nature.com/doi/abs/10.1038/nature17183>
- [41] N. J. English and C. J. Waldron, “Perspectives on external electric fields in molecular simulation: progress, prospects and challenges,” *Phys. Chem. Chem. Phys.*, vol. 17, pp. 12407–12440, 2015. [Online]. Available: <http://dx.doi.org/10.1039/C5CP00629E>
- [42] H. P. Schwan, “Electrical properties of bound water,” *Annals of the New York Academy of Sciences*, vol. 125, no. 2, pp. 344–354, 1965. [Online]. Available: <http://dx.doi.org/10.1111/j.1749-6632.1965.tb45401.x>

- [43] C. R. Middaugh, “Dielectric behavior of biological molecules in solution (Grant, E. H.; Sheppard R. J.; South G. P.),” *Journal of Chemical Education*, vol. 56, no. 8, p. A260, 1979. [Online]. Available: <http://dx.doi.org/10.1021/ed056pA260.3>
- [44] S. Mashimo, S. Kuwabara, S. Yagihara, and K. Higasi, “Dielectric relaxation time and structure of bound water in biological materials,” *Journal of Physical Chemistry*, vol. 91, no. 25, pp. 6337–6338, 1987.
- [45] S. Takashima, “Dielectric dispersion of albumins. Studies of denaturation by dielectric measurement,” *Biochimica et Biophysica Acta (BBA)-Specialized Section on Biophysical Subjects*, vol. 79, no. 3, pp. 531–538, 1964.
- [46] S. Harvey and P. Hoekstra, “Dielectric relaxation spectra of water adsorbed on lysozyme,” *The Journal of physical chemistry*, vol. 76, no. 21, pp. 2987–2994, 1972.
- [47] N. Miura, N. Asaka, N. Shinyashiki, and S. Mashimo, “Microwave dielectric study on bound water of globule proteins in aqueous solution,” *Biopolymers*, vol. 34, no. 3, pp. 357–364, 1994.
- [48] B. Bagchi, “Water dynamics in the hydration layer around proteins and micelles,” *Chemical Reviews*, vol. 105, no. 9, pp. 3197–3219, 2005.
- [49] S. Khodadadi, S. Pawlus, and A. P. Sokolov, “Influence of Hydration on Protein Dynamics: Combining Dielectric and Neutron Scattering Spectroscopy Data,” *The Journal of Physical Chemistry B*, vol. 112, no. 45, pp. 14 273–14 280, Nov. 2008. [Online]. Available: <http://pubs.acs.org/doi/abs/10.1021/jp8059807>
- [50] J. Mijović, Y. Bian, R. A. Gross, and B. Chen, “Dynamics of Proteins in Hydrated State and in Solution As Studied by Dielectric Relaxation Spectroscopy,” *Macromolecules*, vol. 38, no. 26, pp. 10 812–10 819, Dec. 2005. [Online]. Available: <http://pubs.acs.org/doi/abs/10.1021/ma051854c>
- [51] B. Halle, “Protein hydration dynamics in solution: a critical survey,” *Philosophical Transactions of the Royal Society B: Biological Sciences*, vol. 359, no. 1448, pp. 1207–1224, Aug. 2004. [Online]. Available: <http://rstb.royalsocietypublishing.org/cgi/doi/10.1098/rstb.2004.1499>
- [52] A. Oleinikova, P. Sasisanker, and H. Weingärtner, “What Can Really Be Learned from Dielectric Spectroscopy of Protein Solutions? A Case Study of Ribonuclease A,” *The Journal of Physical Chemistry B*, vol. 108, no. 24, pp. 8467–8474, Jun. 2004. [Online]. Available: <http://pubs.acs.org/doi/abs/10.1021/jp049618b>
- [53] B. L. Mellor, S. J. Wood, and B. A. Mazzeo, “Quantitation of pH-induced Aggregation in Binary Protein Mixtures by Dielectric Spectroscopy,” *The Protein Journal*, vol. 31, no. 8, pp. 703–709, Dec. 2012. [Online]. Available: <http://link.springer.com/10.1007/s10930-012-9450-5>
- [54] D. V. Matyushov, “On the theory of dielectric spectroscopy of protein solutions,” *Journal of Physics: Condensed Matter*, vol. 24, no. 32, p. 325105, Aug. 2012. [Online]. Available: <http://stacks.iop.org/0953-8984/24/i=32/a=325105?key=crossref.b0469289d4b9945520eaf2732275e5f0>
- [55] S. Boresch, P. Höchtel, and O. Steinhauser, “Studying the Dielectric Properties of a Protein Solution by Computer Simulation,” *The Journal of Physical Chemistry B*, vol. 104, no. 36, pp. 8743–8752, Sep. 2000. [Online]. Available: <http://pubs.acs.org/doi/abs/10.1021/jp0008905>
- [56] G. Löffler, H. Schreiber, and O. Steinhauser, “Calculation of the dielectric properties of a protein and its solvent: theory and a case study,” *Journal of molecular biology*, vol. 270, no. 3, pp. 520–534, 1997.
- [57] A. Warshel and J. Aqvist, “Electrostatic energy and macromolecular function,” *Annual review of biophysics and biophysical chemistry*, vol. 20, no. 1, pp. 267–298, 1991.

- [58] M. Wolf, R. Gulich, P. Lunkenheimer, and A. Loidl, "Relaxation dynamics of a protein solution investigated by dielectric spectroscopy," *Biochimica et Biophysica Acta (BBA) - Proteins and Proteomics*, vol. 1824, no. 5, pp. 723–730, May 2012. [Online]. Available: <http://linkinghub.elsevier.com/retrieve/pii/S1570963912000374>
- [59] C. N. Schutz and A. Warshel, "What are the dielectric "constants" of proteins and how to validate electrostatic models?" *Proteins: Structure, Function, and Genetics*, vol. 44, no. 4, pp. 400–417, Sep. 2001. [Online]. Available: <http://doi.wiley.com/10.1002/prot.1106>
- [60] M. Neumann and O. Steinhauser, "On the calculation of the frequency-dependent dielectric constant in computer simulations," *Chemical physics letters*, vol. 102, no. 6, pp. 508–513, 1983.
- [61] N. Q. Vinh, S. J. Allen, and K. W. Plaxco, "Dielectric Spectroscopy of Proteins as a Quantitative Experimental Test of Computational Models of Their Low-Frequency Harmonic Motions," *Journal of the American Chemical Society*, vol. 133, no. 23, pp. 8942–8947, Jun. 2011. [Online]. Available: <http://pubs.acs.org/doi/abs/10.1021/ja200566u>
- [62] S. Floros, M. Liakopoulou-Kyriakides, K. Karatasos, and G. E. Papadopoulos, "Detailed study of the dielectric function of a lysozyme solution studied with molecular dynamics simulations," *European Biophysics Journal*, vol. 44, no. 8, pp. 599–611, Dec. 2015. [Online]. Available: <http://link.springer.com/10.1007/s00249-015-1052-7>
- [63] L. Li, C. Li, Z. Zhang, and E. Alexov, "On the Dielectric "Constant" of Proteins: Smooth Dielectric Function for Macromolecular Modeling and Its Implementation in DelPhi," *Journal of Chemical Theory and Computation*, vol. 9, no. 4, pp. 2126–2136, Apr. 2013. [Online]. Available: <http://pubs.acs.org/doi/abs/10.1021/ct400065j>
- [64] D. A. Karp, A. G. Gittis, M. R. Stahley, C. A. Fitch, W. E. Stites, and B. García-Moreno E., "High Apparent Dielectric Constant Inside a Protein Reflects Structural Reorganization Coupled to the Ionization of an Internal Asp," *Biophysical Journal*, vol. 92, no. 6, pp. 2041–2053, Mar. 2007. [Online]. Available: <http://linkinghub.elsevier.com/retrieve/pii/S000634950771010X>
- [65] B. L. Mellor, "Liquid dielectric spectroscopy and protein simulation," Ph.D. dissertation, Brigham Young University, 2012.

LIST OF AUTHOR'S PUBLICATIONS RELATED TO THE DOCTORAL THESIS

All authors contributed equally, unless otherwise states.

PAPERS IN PEER-REVIEWED JOURNALS WITH IMPACT FACTOR

- [A1] O. Krivosudský, M. Cifra, "Microwave absorption by nanoresonator vibrations tuned with surface modification", *EPL: Europhysics Letters*, vol. 115, issue 4, a. num. 44003, 2016.
Candidate's contribution: 60 %
- [A2] O. Krivosudský, P. Dráber and M. Cifra, "Resolving controversy of unusually high refractive index of tubulin", *EPL: Europhysics Letters*, vol. 117, issue 3, a. num. 38003, 2017.
Candidate's contribution: 60 %
- [A3] O. Krivosudský, D. Havelka, D. E. Chafai and M. Cifra, "On-chip microwave sensing of tubulin and its polymer", Submission in process.
Candidate's contribution: 35 %
- [A4] D. Havelka, O. Krivosudský, J. Průša and M. Cifra, "Rational design of sensor for broadband dielectric spectroscopy of biomolecules", *Sensors and Actuators B: Chemical*, vol. 273, pages 62 - 69, 2018.
Candidate's contribution: 25 %

PAPERS AND ABSTRACTS IN CONFERENCE PROCEEDINGS LISTED IN THE WEB OF KNOWLEDGE

- [D1] O. Krivosudský, M. Cifra, "Microwave absorption of electromechanical nanoresonators", *European biophysics journal with biophysics letters*, vol. 44, pages s57, 2015.
- [D2] D. Havelka, O. Krivosudský, M. Cifra, "Grounded Coplanar Waveguide- based 0.5-50 GHz Sensor for Dielectric Spectroscopy", *2017 47th European Microwave Conference (EUMC)*, pages 950 - 953, 2017.
- [D3] D. Havelka, O. Krivosudský, J. Průša and M. Cifra, "Microvolume Dielectric Spectroscopy and Molecular Dynamics of Amino Acids", *Biophysical journal*, vol. 112, issue 3, pages 457A, 2017.

PATENTS

We have no patents related to the doctoral thesis.

CITATIONS IN WEB OF KNOWLEDGE AND SCOPUS

Citations are presented.

Paper [A1]:

[A1.1] Salari V. et al.: "Electromagnetic fields and optomechanics in cancer diagnostics and treatment", *Frontiers in bioscience - landmark*, vol. 23, pages 1391-1406, 2018.

Paper [A2]:

[A2.1] Barzanjeh Sh. et al.: "Optomechanical proposal for monitoring microtubule mechanical vibrations", *Physical review E*, vol. 96, issue 1, 2017.

[A2.2] Kurian P. et al.: "Oxidative species-induced excitonic transport in tubulin aromatic networks: Potential implications for neurodegenerative disease", *Journal of Photochemistry and Photobiology B: Biology*, vol. 175, pages 109-124, 2017.

[A2.3] Santelices I. B. et al.: "Response to Alternating Electric Fields of Tubulin Dimers and Microtubule Ensembles in Electrolytic Solutions", *Scientific Reports*, vol. 7, issue 1, 2017.

RESEARCH PROJECTS

Radio-frequency characterization of microtubules using micro- and nanosensors, No. 15-17102S, Czech Science Foundation, *Member of the team*.

Nanosecond electric pulses for modulation of microtubule dynamics, No. 17-11898S, Czech Science Foundation, *Member of the team*.

High-frequency microdevices for controlling protein nanomotors, No. 18-23597S, Czech Science Foundation, *Member of the team*.

APPENDIX

This chapter includes one paper [A4], the supplementary data of Section 4, Section 5, Section 6, and Article [A4] A.

This chapter is a version of:

- | D. Havelka, **O. Krivosudský**, J. Průša and M. Cifra,
Rational design of sensor for broadband dielectric spectroscopy of biomolecules,
Physical review E, vol. 96, issue 1, 2017. DOI: 10.1016/J.SNB.2018.05.124.

Author contributions:

- | **Daniel Havelka:**
Investigation (lead), Data curation. Formal analysis (lead), Software (lead), Methodology (equal),
Validation (lead), Visualization, Writing - original draft (supporting)
- | **Ondrej Krivosudský:**
Formal analysis (supporting), Writing - original draft (supporting), Investigation (supporting),
Software (supporting), Writing - original draft (supporting)
- | **Jiří Průša :**
Formal analysis (supporting), Investigation (supporting), Software (supporting), Writing - original draft
(supporting)
- | **Michal Cifra:**
Conceptualization, Funding acquisition, Investigation (supporting), Methodology (equal), Project
administration, Validation (supporting), Resources, Supervision, Writing - original draft (lead),
Writing - review & editing (lead)
- | Candidate's contribution: 25%

The manuscript carries the following acknowledgements:

- | We acknowledge major financial support from the Czech Science Foundation, project no. 15-17102S. Authors participate in COST Actions BM1309, CA15211 and bilateral exchange project between Czech and Slovak Academies of Sciences, no. SAV-15-22. The CESNET LM2015042 provided computational resources and the CERIT Scientific Cloud LM2015085, provided under the programme "Projects of Large Research, Development, and Innovations Infrastructures". Milan Příhoda is acknowledged for his initial contribution to CBCPW design, Martin Kempa and Viktor Bovtun from the Institute of Physics, CAS, are for assisting in the reference dielectric spectroscopy measurements, Maxime Alcover for pointing to the derivation of the analytical model and Djamel E. Chafai and Abhishek K. Jha for proofreading



Contents lists available at ScienceDirect

Sensors and Actuators B: Chemical

journal homepage: www.elsevier.com/locate/snb

Rational design of sensor for broadband dielectric spectroscopy of biomolecules



Daniel Havelka, Ondrej Krivosudský, Jiří Průša, Michal Cifra*

Institute of Photonics and Electronics of the Czech Academy of Sciences, Prague, 18200, Czechia

ARTICLE INFO

Keywords:

High-frequency biosensors
Radiofrequency and microwave chips
Dielectric spectroscopy
Proteins
Molecular dynamics

ABSTRACT

Knowledge of electromagnetic properties of biomolecules is essential for a fundamental understanding of electric field interaction with biosystems and for development of novel biomedical diagnostic and therapeutic methods. To enable systematic analysis of the dielectric properties of biomolecule solutions we presented here a method for a rational design of radiofrequency and microwave chip for quantitative dielectric sensing. At first, we estimated the primary frequency band of interest using a relaxation time of targeted molecule via the Stokes–Einstein–Debye equation. Then we proposed a microwave sensing chip for the estimated frequency band and evaluated its performance using both analytical modeling and numerical electromagnetic simulations. We fabricated the chip and experimentally demonstrated that we can extract the complex permittivity (0.5–40 GHz) of the water solution of alanine – one of the most common proteinogenic amino acids – without any calibration liquid and with about 20-fold smaller volume than with commercial methods. The observed dependence of extracted complex permittivity on the alanine concentration was interpreted using molecular dynamics simulations. The procedure we described here can be applied for the development of dielectric sensing method of any polar biomolecule solution.

1. Introduction

Fundamental function of biomolecules is governed by a delicate balance of electric and electrodynamic forces within and among them [1–4]. The electric nature of biomolecules can be described by their dielectric properties, which influence the distribution of electromagnetic fields and determine a behavior of biomolecules in electric field. Hence, dielectric and polarization properties of the biomolecules are essential for (i) fundamental understanding of biomolecular interactions [5] and for (ii) understanding of external electric field interaction with biological matter at the nanoscale [6,7]. This understanding is also opening a new way for possible manipulation of biomolecules, to enhance or change their function and to explore novel paths for development of biomedical electromagnetic-field based diagnostic [8] and therapeutic [9,10] methods. However, due to their complexity, small dimensions (micro- to nano-size) and dynamic behavior across multiple timescales, characterization of biomolecular structures under their natural conditions remains a challenging task.

Here we present a method for rational design of a dielectric spectroscopy chip starting from the volume and shape of the biomolecule to be analyzed. Furthermore, the chip we designed overcomes several limitations of standard commercial dielectric spectroscopy methods.

The broadband dielectric spectroscopy is a common method to explore electric properties of materials on timescales across several orders of magnitude [11] and brings a deeper understanding of matter on a molecular level [12–15]. There are numerous solutions for dielectric spectroscopy which are commercially available, including various techniques, specimen holders, and principles described in [16,17] as well as technique for liquid specimen measurement [18,19]. All these techniques are dependent on the information about complex parameters (magnitude and phase) of an electromagnetic wave which is reflected or transmitted (reflection and transmission coefficients) through the material under investigation. While there are numerous techniques available they have several limitations. The most widely used technique for measurement of the liquid specimens is with an open-ended coaxial probe [20–23]. The open-ended coaxial probe is a section of coaxial transmission line. The material is measured by immersing the probe into a liquid or touching it to the flat face of a solid material. The permittivity and impedance of a test specimen then translate into the input reflection coefficient measured with the probe. One of the limitations of the coaxial probe technique is that a specimen must be homogeneous within a volume sufficiently large (several milliliters) to simulate a slab which is electrically infinite in size [24]. The need of large specimen volumes prevents analysis of many types of

* Corresponding author.

E-mail address: cifra@ufe.cz (M. Cifra).<https://doi.org/10.1016/j.snb.2018.05.124>

Received 6 October 2017; Received in revised form 27 April 2018; Accepted 21 May 2018

Available online 26 May 2018

0925-4005/ © 2018 Elsevier B.V. All rights reserved.

biological structures which are often expensive in a purified state and can not be provided in volumes larger than a small fraction of a milliliter. Another common limitation and uncertainty is connected with calibration where it is necessary to use a material with known dielectric properties [25] as a calibration standard. Typical coaxial probe techniques are also inherently bulky which prevents a possibility of their integration on chips for potential biomedical applications.

These limitations prompted a design of new broadband microwave/radiofrequency (RF) dielectric spectroscopy techniques which (i) can operate with much smaller volumes and which (ii) can measure both reflection coefficient and transmission coefficient to increase robustness for a wide range of specimen properties. These requirements are met by a coplanar waveguide (CPW) which additionally offers the advantage of simple transition from commonly used coaxial cables. CPW structures served for exposing cells to high frequency electromagnetic field [26,27] and were already employed for sensing of small volumes biosamples [28–32] reaching even down to sub-nanoliter [33]. However, on the one hand, they either required microfluidic approaches [33–35], which can be cumbersome to fabricate or require additional mechanical machining [36]. On the other hand, some approaches such as polydimethylsiloxane microfluidics formed by baking in a mold are rather easy to fabricate microfluidics but typically do not enable accurate placing and geometry, hence they are often useful for sensing only a relative change of electric parameters of biosamples [37,28] and not for extraction of absolute electric parameters such as complex permittivity. Furthermore, the vast majority of works demonstrating new RF and microwave sensors does not explicitly consider spectral requirements for the sensing design given by the specific physical properties of the biosamples.

In this paper, we identify the main spectral region of interest based on the structural properties (approximate volume and shape) of the molecule to be analyzed and exploit this knowledge in design of novel conductor-backed coplanar waveguide (CBCPW) based sensing structure which overcomes limitations mentioned above. We demonstrate the use of the procedure on L-alanine – one of the most common proteinogenic amino acids – and use alanine water solution to verify the function of our low-volume sensor in comparison with standard large volume commercial method. Also, we interpret the measured dependence of solution complex permittivity on the alanine concentration using molecular dynamics simulation. See the Fig. 1 for the graphical depiction of the logical flow and structure of the paper.

2. Materials and methods

2.1. Chemicals

Amino acid L-alanine ($\geq 98\%$ purity, A7627) here investigated was purchased from Sigma–Aldrich and used as received. Aqueous solutions were prepared by dissolving the amino acid in Millipore Q-water with DC conductivity $0.05 \mu\text{S}/\text{cm}$. All measurements were performed after full dissolution at 22°C . The DC conductivity of alanine solutions was 8.74, 12.44, and $16.09 \mu\text{S}/\text{cm}$ for 50, 100, and $150 \text{ mg}/\text{mL}$ concentration, respectively. Conductivity meter Thermo Scientific Orion Star A222 with Orion 013010MD probe was used for all DC (2 kHz) conductivity measurements.

2.2. Reference measurement

As a standard reference commercial method, Agilent 85070E Dielectric Probe Kit (0.5–50 GHz, Slim Form Probe) was used with Agilent E8364B vector network analyzer. The dielectric coaxial probe was calibrated before each measurement by standard calibration probe kit (Air, Short, and Liquid). As a liquid Millipore Q-water was used. Measurements were performed by immersing the probe in 5 mL specimen volumes at stable 22°C temperature. Between each immersion, the probe was rinsed in Q-water and dried on air. After every probe immersion into the specimen, a tip of the probe was checked for bubble formation to avoid measurement artifacts.

2.3. Measurement with chip

Vector network analyzer (VNA) Rohde&Schwarz® ZVA40 was used in all experiments with the chip “SAMPLE 1 4 mm”. One pair of phase-stable cables (Mini-Circuits, KBL-2M-PHS+) was used. End-launch connectors (2.4 mm female) of Southwest Microwave model 1492-03A-5 were used as a connection between cables and our coplanar waveguide chip. Before each measurement, VNA was calibrated using Multiline-TRL method (Reflect, Thru, 1, 2, 4, and 8 mm) calibration lines. Calibration was verified using Beatty line and evaluation of ALSE parameter (Average Least Square Error value with a -35 dB threshold line through the entire frequency range). Afterward, scattering parameters of the ideal line (72 mm line) were measured. Data were used for extraction of substrate permittivity in CST Microwave Studio, to achieve the best match of experimental and simulated data. Thereafter the experimental setup with chip (SAMPLE 1 4 mm) was connected. A droplet of the specimen ($250 \mu\text{L}$) was carefully injected into sensing area by a laboratory micropipette and S-parameters were saved. Then the specimen was removed by the KIMTECH SCIENCE Precision fiber free tissue without touching the chip surface, and then the chip was blow-dried with compressed air between each specimen change. The measurement of S-parameters of alanine solution has been repeated nine times (3×3 independently prepared specimens) for each concentration, while pure water has been measured once. The measurement sequence was pure water, 50, 100, and $150 \text{ mg}/\text{mL}$. See Fig. S5 for information on the reproducibility of the measurement. The average of 9 S-parameter measurements was taken as the input into permittivity extraction.

2.4. Permittivity extraction

Our method of permittivity extraction does not require any a priori assumption about the dielectric properties of a liquid specimen. Complex permittivity of the specimen was extracted in the following way. Our model of chip in the CST Microwave Studio had all dimensions corresponding to the those of the fabricated chip with specimen droplet on the top of it (Fig. 3D). Experimentally measured S-parameters were processed as $S_R^{\text{MEAS}} = (S_{11} + S_{22})/2$ and $S_T^{\text{MEAS}} = (S_{21} + S_{12})/2$ and then were compared with the calculated S-parameters (S_{11}^{SIMUL} and S_{21}^{SIMUL}) of model in the CST Microwave Studio. After that, an optimization algorithm (Trust Region Framework) implemented in CST Microwave Studio was used to keep shifting the specimen permittivity (ϵ'_2 and ϵ''_2) at the desired frequency point until the four optimization goals were met at the same time. Optimization

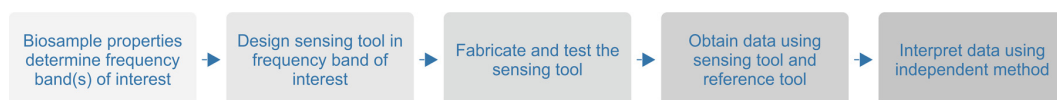


Fig. 1. The logical flow and structure of the paper. The biosample (here alanine in water) determines the frequency band where the sensor should have the best performance. Next, we design, fabricate and test the sensor. Then we obtain complex permittivity data using our sensor as well as using a reference method (coaxial dielectric probe). Finally, the complex permittivity data are interpreted using an independent theoretical method – molecular dynamics simulation.

goals were (i) $\|S_R^{\text{MEAS}} - S_{11}^{\text{SIMUL}}\| < 0.05$, (ii) $\|S_T^{\text{MEAS}} - S_{21}^{\text{SIMUL}}\| < 0.005$, (iii) $|\angle S_R^{\text{MEAS}} - \angle S_{11}^{\text{SIMUL}}| < 5^\circ$, and (iv) $|\angle S_T^{\text{MEAS}} - \angle S_{21}^{\text{SIMUL}}| < 5^\circ$. In the optimization algorithm, initial values of permittivity (ϵ'_{r2} and ϵ''_{r2}) are set to a permittivity of Debye water model [38,39] ($\epsilon(0) = 79.27$, $\epsilon(\infty) = 6.09$, $\tau = 8.84$ ps, and $\sigma = 5$ $\mu\text{S}/\text{m}$). See supplementary data, Eq. (13) at a corresponding frequency. Optimization intervals of ϵ'_{r2} and ϵ''_{r2} were $\langle 10, 130 \rangle$ and $\langle 1, 50 \rangle$, respectively. This procedure was repeated for essential number of frequency points. Thus, complex permittivity function of any unknown liquid specimen could be obtained. Note that throughout the paper we use complex permittivity sign convention based on electric field harmonic time dependence given by $e^{-j\omega t}$.

2.5. Fitting of extracted permittivity points

The Debye model (Eq. (1)) was used for fitting of pure water data and the double Debye model (Eq. (2)) was used for fitting of alanine 50 mg/mL, alanine 100 mg/mL, and alanine 150 mg/mL data in the MATLAB. Points up to 20 GHz were used as an input to the data fitting. The function obtained by fitting was plot up to 40 GHz:

$$\epsilon^*(\omega) = \epsilon_\infty + \frac{\Delta\epsilon_w}{1 + j\omega\tau_w} \quad (1)$$

$$\epsilon^*(\omega) = \epsilon_\infty + \frac{\Delta\epsilon_w}{1 + j\omega\tau_w} + \frac{\Delta\epsilon_{AA}}{1 + j\omega\tau_{AA}} \quad (2)$$

where ϵ_∞ is permittivity at high frequency, $\Delta\epsilon_w$ is the dielectric increment of water, $\Delta\epsilon_{AA}$ is the dielectric increment of amino acids, ω is angular frequency, τ_w is relaxation time of water molecules, τ_{AA} is relaxation time of amino acid (alanine) molecules, and j is imaginary unit ($j^2 = -1$).

2.6. Molecular dynamics simulations

The simulation procedure was same for all concentrations of alanine. We positioned 0, 9, 17, and 25 amino acid molecules, respectively, with mutually random position and orientation into $32 \times 32 \times 32 \text{ \AA}^3$ water box, removed water molecules overlapping with alanine and minimized the energy of the system by conjugate gradient algorithm for 200 steps. After this, the 300 ps in NpT ensemble (300 K, 1 atm) was run for equilibration of the system. The main production run was 3 ns long NVT simulation (300 K) with all bond length constrained applying SHAKE algorithm [40] with the box dimensions inherited from NpT equilibration part. Time step for both simulation procedures was set to 2 fs and evaluation of long-range electrostatics treated by Particle mesh Ewald (PME) method [41], cutoff 10 \AA and the coordinates from trajectory were saved for every 0.5 ps. The simulation contained 9/17/25 alanine molecules (81/153/225 alanine atoms) and 913/850/794 water molecules (2739/2550/2382 water atoms) for alanine concentrations 50/100/150 mg/mL, respectively. All the simulations were carried out by NAMD [42] software utilizing CHARMM19 united-atom force field [43] and TIP3P water model. The CHARMM19 force field was used because it provided a better match to experimental data than newer versions of this force field. We used the last 2,700 ps from main production run for evaluation of dielectric properties.

For low electric field intensity the dielectric function $\epsilon(\omega)$ of solution as function of frequency can be derived from equilibrium molecular dynamics (MD) simulation as shown by Boresch and Steinhauser [44,45]. Specifically a complex susceptibility $\chi(\omega) = \chi'(\omega) + j\chi''(\omega) = \epsilon(\omega) - 1$ of specimen is given as Fourier–Laplace transformation of time derivative of dipole moment time correlation function of the system (specimen):

$$\chi(\omega) = \frac{1}{3VKT} \mathcal{L}[-\dot{\Phi}(t)] \quad (3)$$

where V is volume of the system (simulation box), k is Boltzmann constant, T is thermodynamic temperature, \mathcal{L} is the Fourier–Laplace transformation, and Φ is time correlation function of dipole moment given by

$$\Phi_{ij}(t) = \langle \vec{M}_i(0) \cdot \vec{M}_j(t) \rangle \quad (4)$$

where $\vec{M}_i(0)$ is the total dipole moment of i th component at the time 0. Index $i = j$ for the autocorrelation function. As shown by Boresch and Steinhauser [44] the overall susceptibility of the system can be expressed as the sum of “individual” components susceptibilities

$$\chi(\omega) = \sum_{ij} \chi_{ij}(\omega) = \frac{1}{3VKT} \sum_{ij} \mathcal{L}[-\dot{\Phi}_{ij}(t)] \quad (5)$$

where χ_{ij} is the contribution to susceptibility from ij component. In this study we chose to divide the system into two components. The first includes all the water molecules of the system and the later all alanine molecules. We suppose that $\chi_{AW} = \chi_{WA}$ and the total susceptibility of the system is given by (putting together Eqs. (3) and (5))

$$\chi(\omega) = \chi_{AA}(\omega) + 2\chi_{AW}(\omega) + \chi_{WW}(\omega) = \frac{1}{3VKT} (\mathcal{L}[-\dot{\Phi}_{AA}(t)] + 2\mathcal{L}[-\dot{\Phi}_{AW}(t)] + \mathcal{L}[-\dot{\Phi}_{WW}(t)]) \quad (6)$$

where χ_{AA} is the susceptibility contribution of amino acid, χ_{AW} is amino acid-water part of susceptibility and χ_{WW} is the susceptibility contribution of water. Although the effect of different alanine concentrations could be simply simulated by putting an appropriate number of alanine molecules into the box, there is still a question how long should be the simulation to sufficiently sample the system phase space for various mutual distances and orientations of individual alanine molecules. Especially the effect of molecule aggregation could prolong the correlation time markedly. To provide sufficient sampling of the phase space, we prepared the system in 50 different initial coordinates and then ran the simulation procedure individually for each of them and finally averaged the obtained time-correlation function over the number of simulation runs after that. By this procedure, we obtain fifty 3 ns trajectories. We calculate the dipole moment correlation function for each trajectory independently (from Eq. (4)) and then we obtain a mean dipole moment correlation function as an average from these fifty autocorrelation functions. Thereafter we fit the obtained correlation function by a biexponential fitting function $\Phi_{fit}(t) = A_1 e^{-t/\tau_1} + A_2 e^{-t/\tau_2}$. Hence, the real (χ') and imaginary (χ'') part of susceptibility as the Fourier–Laplace transform of Φ_{fit} could be obtained from analytical formulas:

$$\chi'(\omega) = \chi(0) - \omega \left(\frac{A_1 \tau_1^2 \omega}{1 + \tau_1^2 \omega^2} + \frac{A_2 \tau_2^2 \omega}{1 + \tau_2^2 \omega^2} \right) \quad (7)$$

$$\chi''(\omega) = \omega \left(\frac{A_1 \tau_1}{1 + \tau_1^2 \omega^2} + \frac{A_2 \tau_2}{1 + \tau_2^2 \omega^2} \right) \quad (8)$$

3. Results

3.1. Identification of the spectral region of interest

Relaxation phenomena dominate complex permittivity of biomaterials in radiofrequency and microwave band due to rotational diffusion of constituent molecular dipoles [46]. Therefore, the relaxation time due to rotational diffusion of the molecules is of central interest and determines the frequency range of interest for dielectric spectroscopy sensing. Here we show guidelines to identify the spectral region of interest on the example of a small molecule solute in the water as a solvent. In the first step, depending on its shape and dipole moment orientation, the molecule can be approximated as a spherical particle or ellipsoidal particle [47,46]. A small amino acid in the water we aimed to analyze can be reasonably approximated by a spherical particle in a

viscous medium, for which the Stokes–Einstein–Debye formula [48,p. 206; 49] gives relaxation time [50]:

$$\tau = \frac{3V\eta}{kT} \quad (9)$$

where V is the specific volume of amino acid, η is the solvent dynamic viscosity at given temperature T , k is the Boltzmann constant. Considering a range of volumes of amino acids ($50\text{--}163 \text{ \AA}^3$) [51] and solvent (water) viscosity $\eta = 10^{-3} \text{ Pa s}$ at room temperature $T = 293.15 \text{ K}$, then the relaxation time lies in sub-nanosecond region and corresponding frequency band ($f_{AA} = 1/(2\pi\tau)$) due to amino acids rotational diffusion lie in 1–4.5 GHz band. The center frequency of the alanine, our model amino acid, is predicted to be at 3.2 GHz. Same arguments applied to a single water molecule (considering effective Van der Waals volume of water molecule $\approx 15 \text{ \AA}^3$) lead to the theoretical frequency at around 14 GHz which slightly differs from experimental values of ca. 17–19 GHz [39] due to simplicity of the model in Eq. (9) which neglects other effects. Based on these predictions, for the next design, the primary aim was to obtain a maximum sensitivity of the method at the expected frequency band due to amino acid rotational diffusion (1–4.5 GHz) while having reasonable sensitivity at the frequency band due to water molecule rotational diffusion (14–20 GHz).

3.2. Predictive sensitivity analysis

Due to advantages described in the Introduction, we decided to base our sensor design on a conductor-backed coplanar waveguide structure (CBCPW). The principle of the operation of CBCPW for dielectric sensing is as follows. Electromagnetic wave propagates along the grounded coplanar waveguide and enters into sensing area of the CBCPW which contains biological specimen. A fraction of the wave is reflected and a fraction is transmitted through the specimen. We measure amplitude and phase of the reflected and transmitted wave and that enables us to extract complex permittivity of the specimen.

Our sensor is combining two approaches: (i) CBCPW which has a reasonable sensitivity across the broadband from 1 to 40 GHz, and (ii) the sensing segment loaded with the liquid specimen behaves as a dielectric resonator with a low quality factor to enhance sensitivity in the frequency band of interest. To make a guiding assessment of the sensitivity of scattering parameters (S-parameters like S_{11} and S_{21}) of the chip to a variation of the specimen permittivity ϵ_{r2} , we defined the sensitivity as $\xi_{11} = |\Delta S_{11}/\Delta\epsilon_{r2}|$ and $\xi_{21} = |\Delta S_{21}/\Delta\epsilon_{r2}|$. We used an analytical model of CBCPW with a dielectric on the top which enables us to calculate S-parameters of the CBCPW. We considered a 50 \Omega impedance CBCPW separated into three segments see Fig. 2A. Middle segment has a dielectric specimen on the top with thickness h_2 and complex permittivity ϵ_{r2} given by the Debye model [38,39] of water to represent a

water-like solution of the biomolecular specimen. Length of the specimen is the same as the length of the middle segment of CBCPW (l_2). We derived equations of S-parameters of such CBCPW, see Methods and Supplementary data. Using these equations, we calculated the sensitivity of the magnitude of reflection and transmission coefficient to the variation of permittivity dependent on the frequency and the specimen length (Fig. 2B and C). Analytical formulation enabled us to estimate that for maximal sensitivity in the frequency bands of amino acids while keeping the specimen sufficiently small, the optimal length l_2 of the specimen segment is around 6.4 mm. We used this length as a starting point for an accurate design of the chip in the numerical 3D electromagnetic simulator. We see in Fig. 2B and C that transmission coefficient S_{21} provides higher sensitivity for the 4 GHz band than reflection coefficient S_{11} band while S_{11} provides a slightly better sensitivity in the band $> 20 \text{ GHz}$, beyond the water molecule dispersion.

3.3. Chip design

After analytical estimates, we chose to follow a specific design based on a conductor-backed coplanar waveguide (50 \Omega impedance) chip where the sensing site is formed by switching the sides of the CBCPW through the vias (Fig. 3B, C, E, and F). We implemented this design in the CST (Computer Simulation Technology) Microwave Studio model for all further analyses. The electromagnetic wave is launched to the CBCPW on the reverse (feeding) side (Fig. 3C) and enters along the vias into front (sensing) side of the chip (Fig. 3B). This design modification of the standard CBCPW brought an important advantage over same-feeding-sensing-side CBCPW design: provided that the volume is larger than a certain threshold volume (given by the field distribution, see Fig. 3G and F), the chip provides accurate reading regardless of the exact shape and volume of the specimen droplet to be analyzed. This advantage would not be possible on same-sensing-feeding-side CBCPW without microfluidics or other specimen geometry delimiting cuvette which would require taking into account cuvette material in the permittivity extraction analysis. The chip structure enables appropriate interaction of electromagnetic wave with specimen droplet (Fig. 3D) and high reproducibility for all three analyzed alanine concentrations (see Fig. S5). We arrived to the 4 mm via-to-via length of the sensing segment, which corresponds to roughly 6.4 mm length of the analytical model when distance the wave has to traverse through the vias is added. We selected Multiline-TTL (Through-Reflect-Line) [52–54] calibration technique, designed and fabricated appropriate calibration kit (lines with $L = 1, 2, 4,$ and 8 mm ; reflect – short; through) for our chip in the frequency range 0.5–40 GHz, see Fig. 3H. Multiline-TTL method overcomes standard problems with a use of broadband matched load and brings better accuracy with the minimization of random effects

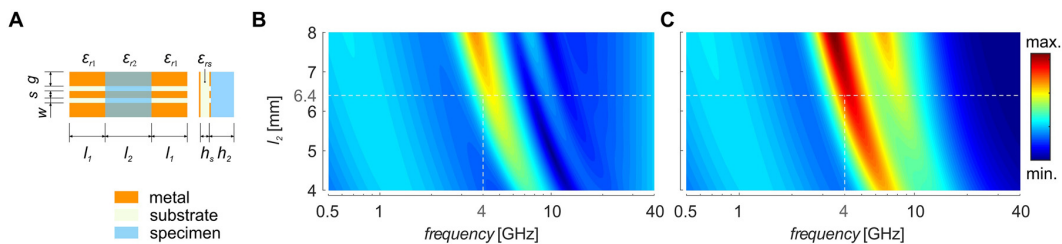


Fig. 2. Sensitivity analysis reveals that the optimal length of the specimen sensing segment (l_2) of the chip is 6.4 mm. (A) Scheme of a model (divided into 3 segments) which analytically approximates the sensitivity of our chip: conductor-backed coplanar waveguide (CBCPW), w is 395 \mu m , s is 1 mm , g is ∞ , ϵ_{r1} is relative permittivity on the top of outer (feeding) CBCPW segments ($\epsilon_{r1} = 1 + j0$) and l_1 is length of outer (feeding) segments of the model and is fixed at 6 mm for the calculation of sensitivity, l_2 is length of middle (sensing) CBCPW segment of the model and its length is varied from 4 to 8 mm for calculation of sensitivity, ϵ_{r2} is relative complex permittivity of dielectric specimen (water) on the top of the middle (sensing) CBCPW segment (Debye model [38,39]: $\epsilon(0) = 79.27$, $\epsilon(\infty) = 6.09$, $\tau = 8.84 \text{ ps}$, and $\sigma = 5 \text{ \mu S/m}$) and height of the specimen h_2 is 4 mm . There is air with permittivity of ϵ_{r1} above the specimen. Substrate RO4350B has permittivity $\epsilon_{rs} = 3.74 + j0.03$ and thickness $h_s = 508 \text{ \mu m}$. (B) Calculated sensitivity $\xi_{11} = |\Delta S_{11}/\Delta\epsilon_{r2}|$. (C) Calculated sensitivity $\xi_{21} = |\Delta S_{21}/\Delta\epsilon_{r2}|$. We used $\Delta\epsilon_{r2} = 5 + j5$ for calculation of sensitivity depicted in (B) and (C). In the colorbar, max. value of sensitivity is 1.59×10^{-2} and min. value is 6.55×10^{-6} . (For interpretation of the references to color in this figure legend, the reader is referred to the web version of this article.)

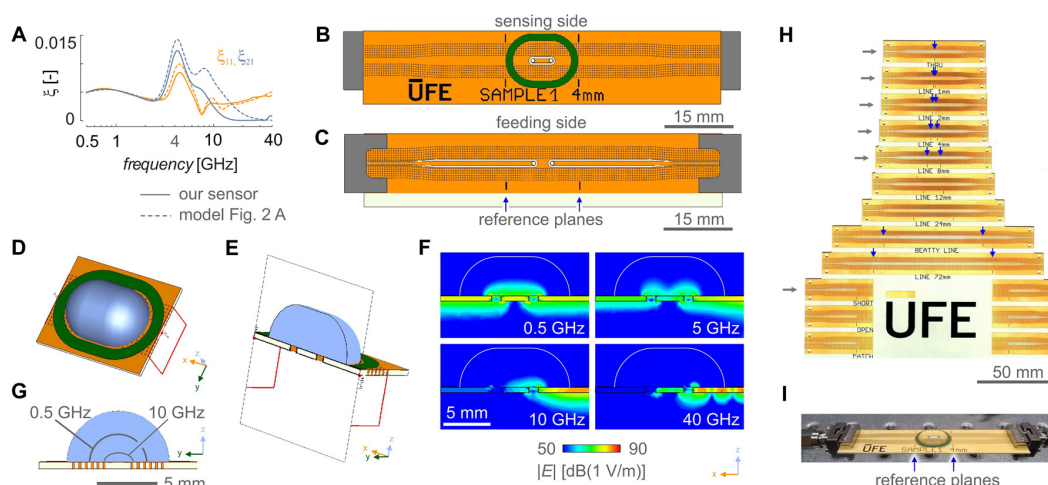


Fig. 3. Our designed and fabricated chip for quantitative dielectric sensing. CST Microwave studio model of a conductor-backed coplanar waveguide chip with the sensing part on the reverse side of the substrate: (A) Sensitivity (ξ) calculated by model Fig. 2A (length $l_2 = 6.4$ mm) and our chip (D). (B) Sensing side of the chip – short black lines represent the reference plane and dark-green mask delimits the sensing area. (C) Feeding side of the chip – light yellow color is RO4350B substrate. (D) Model of a water droplet specimen (250 μ L volume) on the sensing part of the chip. (E) The longitudinal cross-section of the chip with water droplet specimen. (F) The simulated electric field distribution in the cross-section plane of (E). The average of the absolute value of electric intensity is coded in color. The wave propagates from right to left. The curved white line is the border of the water droplet specimen. (G) Isoplanes demarcate volume where 99% of the electric field is enclosed (electric field intensity criterion). (H) Fabricated calibration kit with Beatty line (the grey arrows highlight employed the calibration lines and the blue arrows highlight the reference planes). (I) Fabricated chip “SAMPLE 1 4 mm” with a water droplet (250 μ L volume) on the sensing side of the chip. The blue arrows show the reference planes. (For interpretation of the references to color in this figure legend, the reader is referred to the web version of this article.)

(repeatability of connections, etc.). The reference plane for vector network analyzer (VNA) measurement is marked on the CBCPW structure as depicted on Fig. 3B and C. Since the reference plane is located on the CBCPW transmission line, it was possible to avoid the effects of coaxial-planar end-launchers. Chip, Beatty line and calibration kit were fabricated using a common commercially available printed circuit board technique.

3.4. Complex permittivity of a biomolecular liquid: the experimental case of L-alanine solution

The fabricated and verified chip was used to measure S-parameters for extraction of the complex permittivity of a model biomolecular liquid. We selected L-alanine water solution as a model liquid. Alanine (molar mass 89 Da) belongs to one of the most common α -amino acids used in the biosynthesis of proteins. The Agilent kit based on a coaxial probe was used as a commercial reference tool to obtain complex permittivity from a 5 mL specimen (see Methods for more details). Three different concentrations (50, 100, and 150 mg/mL) of alanine were used in order to cover whole range of solubility and to demonstrate the effects of amino acid presence on the dielectric response of solution. Complex permittivity of a pure water and alanine solution is showed in Fig. 4. Data measured using our chip and extracted using our method are in a good agreement with data obtained using coaxial probe method (see Methods). Nevertheless, our chip requires 20-fold lower volume than the reference coaxial probe method. For pure water (Fig. 4A), a well-known behavior of the dielectric function is observed; single relaxation process of water molecule tumbling at around 20 GHz causes decreasing ϵ'_r of the water and maximum losses (peak of ϵ''_r). Alanine solutions manifest additional concentration-dependent features due to rotational relaxation of alanine. At first, alanine dipole orientation causes an additional polarization at low frequencies (< 3 GHz). This additional polarization is manifested as a concentration-dependent increase of the real part of permittivity at low frequencies, see Figs. 4B–D and S6). At second, ϵ''_r increases around a few GHz – a central frequency band of dispersion due to alanine molecule dipoles (Figs. 4B–D and S6). Since relaxation features are spectrally

broad, the dispersion of alanine and water molecule partially overlap. Hence separated dispersions cannot be seen in experimental data, but are visible if decomposed or analyzed by molecular dynamics (as we show in Fig. S7).

3.5. Complex permittivity from molecular dynamics simulations

To theoretically reproduce and interpret the experimental data from basic principles, we performed equilibrium molecular dynamics (MD) simulations (see Methods) for calculation of the complex permittivity of pure water and alanine solutions (hereinafter termed ‘system’). With certain modifications we followed procedure described by Boresch and Steinhäuser [44,45]. In this procedure a complex frequency dependent susceptibility $\chi(\omega) = \epsilon(\omega) - 1$ of a molecular system ($\omega = 2\pi f$) can be calculated as Fourier–Laplace transformation of time derivative of dipole moment time correlation function of the system or its components (see Methods for details). Results from MD agree satisfactorily with the experimental data (Fig. 4) providing a semi-quantitative comparison. As one can see in Fig. 4 molecular dynamics reproduces all essential features of the experimental data such as concentration-dependent low frequency dielectric increment $\Delta\epsilon(0) = \epsilon(0)_{\text{SOLUTION}} - \epsilon(0)_{\text{WATER}}$, frequency ranges corresponding to the relaxation processes of both amino acid and water molecule tumbling and values of both real and imaginary part of the permittivity with a reasonable accuracy. Furthermore, MD also semi-quantitatively reproduces emergent features which simple theories cannot predict (without auxiliary approximations and parameters): concentration-dependent frequency shift of the ϵ''_r peak of water (see Fig. 4A–D) and as well as that of amino acid (see Fig. S7) which are usually demonstrated only in experimental works [13,46].

4. Discussion

The CBCPW design with sensing area on the opposite side of the substrate than the feeding side has been already recently proposed [55,56]. However, it was limited to 5 GHz missing thus the typical microwave signature of biological specimens: absorption peak of water around 20 GHz. An additional limitation of sensor design in recent

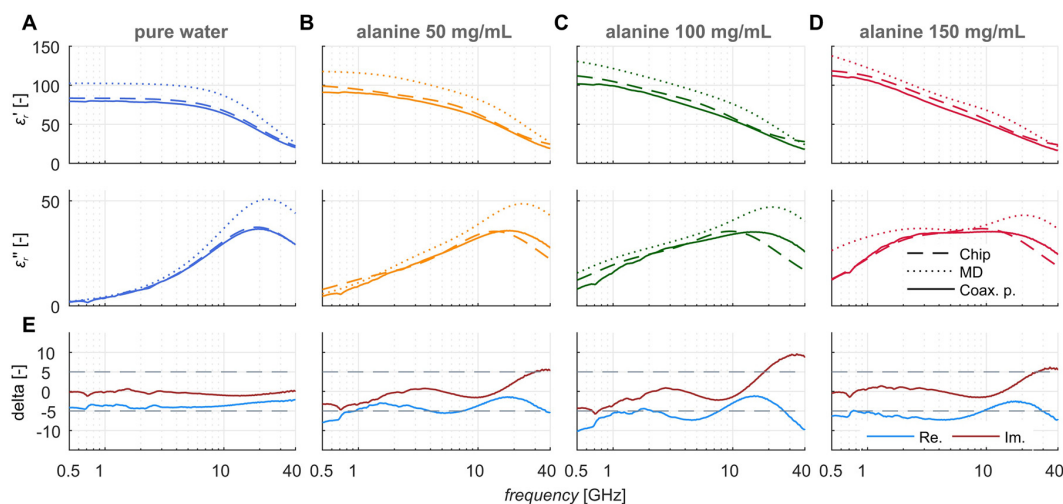


Fig. 4. Experimental results from our chip fairly agree with reference measurement and with molecular dynamics simulation. Real and imaginary parts of relative complex permittivity of a liquid specimen obtained using our chip after fitting (dashed line) vs. reference coaxial probe bulk measurement (solid line) and from molecular dynamics simulation (dotted line) for (A) pure water, (B) 50 mg/mL, (C) 100 mg/mL, and (D) 150 mg/mL of alanine concentration in the pure water. (E) Difference between results from reference method and results from our chip, i.e. coaxial probe data minus data from our chip. Re. stands for real part of permittivity and Im. stands for imaginary part of permittivity.

works [55,56] was the requirement of rather large specimen volumes (order of milliliter). We extended both the frequency range of this approach and significantly lowered the specimen volume required for the experiment compared to these recent developments.

Complex permittivity data obtained using our chip and permittivity extraction method agree very well with the reference data obtained by a reference method with the exception of frequency band > 20 GHz in case of 100 and 150 mg/mL alanine concentrations – this is understandable since our chip was not designed to operate with high sensitivity in this frequency band (see earlier design sections). Our chip enables broadband dielectric spectroscopy: a method which provides broadband data on complex permittivity of a biomaterial. Apart from the molecular understanding of electromagnetic properties of biosystems, dielectric spectroscopy and sensing, yet often in a narrow band, has also many potential biomedical applications [31] in sensing biomolecules as disease biomarkers [57], sensing single cells [28] or analyzing cellular viability [35].

Employing molecular dynamics simulations for complex permittivity data is a powerful approach for both prediction and interpretation of the experimental data because in a MD simulation one obtains direct access to trajectories of every atom which enables separation of polarization contributions from individual molecules and molecular species [58,59]. In Fig. S7, individual contributions to susceptibility from water and alanine obtained from MD simulation enable qualitative and quantitative interpretation of data: while roughly half of $\Delta\epsilon(0)$ is due to alanine dipole moment correlation, another half is due to cross-correlation of alanine and water molecules dipole fluctuations – a finding which is impossible to determine from experimental data only. Additionally, both alanine and cross-correlation of alanine and water molecules dipole fluctuations increase imaginary part of permittivity in a concentration-dependent manner yet at a different rate and increasingly different central frequencies. In general, one has to be careful; since MD simulations may employ various combinations of force fields and water models, they might not always reproduce absolute values within the accuracy we managed to achieve here and may provide only relative ranking, e.g. in energetics of molecular binding [60], while absolute values being few-fold different than the experimental data. In our case, most substantial discrepancy compared to experimental data seems to be in low-frequency real part of the permittivity of water. Taking all potential pitfalls into account, MD still may serve as a useful

tool for parametric study and for data prediction and interpretation across a wide range of parameters which might not always be entirely experimentally accessible or difficult to control precisely such as pressure or temperature. We need to emphasize that here we employed MD only to demonstrate its practical capabilities in prediction and interpretation of biomaterial electromagnetic properties which aid to steer RF and microwave design. Extensive analysis of the effects of various water models and force fields on the computationally obtained complex permittivity is beyond the scope of current paper and will be analyzed in upcoming works.

5. Conclusion

In this work, we started from (i) fundamental principles (rotational diffusion times of molecular components in the specimen to be studied) to predict the frequency bands of interest, (ii) then used simplified analytical models to give preliminary estimate of the sensitivity of the measurement with our proposed chip structure to variations of permittivity, (iii) afterwards we accurately designed the chip in electromagnetic simulator, fabricated, and (iv) we also tested both the conductor-backed coplanar waveguide sensing chip and kit for the most suitable calibration technique. We then (v) experimentally obtained complex permittivity of alanine water solution both using our chip (250 μ L of the specimen) and reference bulk measurement method (5 mL of the specimen) and we finally (vi) interpreted the obtained complex permittivity using molecular dynamics simulations. In summary, we described a whole life cycle of the scientific-rationale-based design of the chip for dielectric spectroscopy of biomolecules: here we chose conductor-backed coplanar waveguide-based chip topology and alanine amino acid as a model biomolecule. We believe that both the specific chip structure we developed here as well as the suggested rationalization of the process for high-frequency electromagnetic design rooted in a deep physical understanding of a biomolecule system to be analyzed will enhance research of future methods in biosensing and bioelectromagnetics.

Author contributions statement

D.H. implemented analytical model of CBCPW, performed chip microwave design, microwave measurements, permittivity extraction,

prepared figures, co-wrote the paper, O.K. implemented analytical dielectric models, prepared the specimens and performed the experiments, co-wrote the paper, J.P. performed all molecular dynamics simulations and co-wrote corresponding part of the paper and M.C. designed the research, formulated the experiments, introduced analytical modeling and wrote the paper. All authors reviewed the manuscript.

Contributions according to CRediT: http://dictionary.casrai.org/Contributor_Roles: D.H.: Investigation (lead), Data curation. Formal analysis (lead), Software (lead), Methodology (equal), Validation (lead), Visualization, Writing – original draft (supporting) O.K.: Formal analysis (supporting), Writing – original draft (supporting), Investigation (supporting), Software (supporting), Writing – original draft (supporting), J.P.: Formal analysis (supporting), Investigation (supporting), Software (supporting), Writing – original draft (supporting), M.C. Conceptualization, Funding acquisition, Investigation (supporting), Methodology (equal), Project administration, Resources, Supervision, Validation (supporting), Writing – original draft (lead), Writing – review & editing (lead).

Conflict of interest

The authors declare that they have no competing interests.

Acknowledgements

We acknowledge major financial support from the Czech Science Foundation, project no. 15-17102S. Authors participate in COST Actions BM1309, CA15211 and bilateral exchange project between Czech and Slovak Academies of Sciences, no. SAV-15-22. The CESNET LM2015042 provided computational resources and the CERIT Scientific Cloud LM2015085, provided under the programme “Projects of Large Research, Development, and Innovations Infrastructures”. Milan Přihoda is acknowledged for his initial contribution to CBCPW design, Martin Kempa and Viktor Bovtun from the Institute of Physics, CAS, are for assisting in the reference dielectric spectroscopy measurements, Maxime Alcover for pointing to the derivation of the analytical model and Djamel E. Chafai and Abhishek K. Jha for proofreading.

Appendix A. Supplementary data

Supplementary data associated with this article can be found, in the online version, at <https://doi.org/10.1016/j.snb.2018.05.124>.

References

- [1] S.D. Fried, S. Bagchi, S.G. Boxer, Extreme electric fields power catalysis in the active site of ketosteroid isomerase, *Science* 346 (6216) (2014) 1510–1514.
- [2] C.M. Roth, B.L. Neal, A.M. Lenhoff, Van der Waals interactions involving proteins, *Biophys. J.* 70 (2) (1996) 977 <http://www.ncbi.nlm.nih.gov/pmc/articles/PMC1224998/>.
- [3] M.-Y. Tsai, W. Zheng, D. Balamurugan, N.P. Schafer, B.L. Kim, M.S. Cheung, P.G. Wolynes, Electrostatics, structure prediction, and the energy landscapes for protein folding and binding: electrostatic energy landscapes for folding and binding, *Protein Sci.* 25 (1) (2016) 255–269, <http://dx.doi.org/10.1002/pro.2751>.
- [4] D. Leckband, D. Bray, A. Johnson, *Intermolecular Forces in Biology*, Cambridge University Press, 2001.
- [5] Z. Zhang, S. Witham, E. Alexov, On the role of electrostatics in protein–protein interactions, *Phys. Biol.* 8 (3) (2011) 035001, <http://dx.doi.org/10.1088/1478-3975/8/3/035001>.
- [6] D.R. Hekstra, K.I. White, M.A. Socolich, R.W. Henning, V. Šrajcar, R. Ranganathan, Electric-field-stimulated protein mechanics, *Nature* (2015), <http://dx.doi.org/10.1038/nature20571>.
- [7] A.C. Aragonès, N.L. Haworth, N. Darwish, S. Ciampi, N.J. Bloomfield, G.G. Wallace, I. Diez-Perez, M.L. Coote, Electrostatic catalysis of a Diels–Alder reaction, *Nature* 531 (7592) (2016) 88–91, <http://dx.doi.org/10.1038/nature16989>.
- [8] T.M. Grzegorzczak, P.M. Meaney, P.A. Kaufman, R.M. di Florio-Alexander, K.D. Paulsen, Fast 3-D tomographic microwave imaging for breast cancer detection, *IEEE Trans. Med. Imaging* 31 (8) (2012) 1584–1592, <http://dx.doi.org/10.1109/TMI.2012.2197218>.
- [9] R.P. Joshi, K.H. Schoenbach, Bioelectric effects of intense ultrashort pulses, *Crit. Rev. Biomed. Eng.* 38 (3) (2010).
- [10] W. Rao, Z.-S. Deng, J. Liu, A review of hyperthermia combined with radiotherapy/chemotherapy on malignant tumors, *Crit. Rev. Biomed. Eng.* 38 (1) (2010) 101–116, <http://dx.doi.org/10.1615/CritRevBiomedEng.v38.i1.80>.
- [11] U. Kaatz, Y. Feldman, Broadband dielectric spectrometry of liquids and biosystems, *Meas. Sci. Technol.* 17 (2) (2006) R17–R35, <http://dx.doi.org/10.1088/0957-0233/17/2/R01>.
- [12] E. Levy, S. Cerveny, I. Ermolina, A. Puzenko, Y. Feldman, Dielectric spectra broadening as a signature for dipole–matrix interaction. IV. Water in amino acids solutions, *J. Chem. Phys.* 140 (13) (2014).
- [13] I. Rodríguez-Arteche, S. Cerveny, A. Alegria, J. Colmenero, Dielectric spectroscopy in the GHz region on fully hydrated zwitterionic amino acids, *Phys. Chem. Chem. Phys.* 14 (2012) 11352–11362, <http://dx.doi.org/10.1039/C2CP41496A>.
- [14] I. Popov, P.B. Ishaq, A. Khamzin, Y. Feldman, The mechanism of the dielectric relaxation in water, *Phys. Chem. Chem. Phys.* 18 (2016) 13941–13953, <http://dx.doi.org/10.1039/C6CP02195F>.
- [15] N. Yamamoto, K. Ohta, A. Tamura, K. Tominaga, Broadband dielectric spectroscopy on lysozyme in the sub-gigahertz to terahertz frequency regions: effects of hydration and thermal excitation, *J. Phys. Chem. B* 120 (21) (2016) 4743–4755, <http://dx.doi.org/10.1021/acs.jpcc.6b01491> pMID: 27158918.
- [16] Application Note 1369-1, Solutions for Measuring Permittivity and Permeability with LCR Meters and Impedance Analyzers, No. Agilent Literature Number 5980-2862EN, (2003) [cited 22.12.15] <http://cp.literature.agilent.com/litweb/pdf/5980-2862EN.pdf>.
- [17] Application Note, Agilent Basics of Measuring the Dielectric Properties of Materials, No. Agilent Literature Number 5989-2589EN, (2014) [cited 22.12.15] <http://cp.literature.agilent.com/litweb/pdf/5989-2589EN.pdf>.
- [18] Technical Overview, Keysight 85070E Dielectric Probe Kit 200 MHz to 50 GHz, No. Keysight Technologies, (2014) [cited 22.12.15] <http://literature.cdn.keysight.com/litweb/pdf/5989-0222EN.pdf>.
- [19] Technical Overview, Keysight N1501A Dielectric Probe Kit 10 MHz to 50 GHz, No. Keysight Technologies, (2015) [cited 22.12.15] <http://literature.cdn.keysight.com/litweb/pdf/5992-0264EN.pdf>.
- [20] J.P. Grant, R.N. Clarke, G.T. Symm, N.M. Spyrou, A critical study of the open-ended coaxial line sensor technique for RF and microwave complex permittivity measurements, *J. Phys. E: Sci. Instrum.* 22 (9) (1989) 757, <http://dx.doi.org/10.1088/0022-3735/22/9/015/meta>.
- [21] V. Raicu, A simple theoretical and practical approach to measuring dielectric properties with an open-ended coaxial probe, *Meas. Sci. Technol.* 6 (4) (1995) 410, <http://dx.doi.org/10.1088/0957-0233/6/4/011/meta>.
- [22] K. Folgerø, T. Tjomsland, Permittivity measurement of thin liquid layers using open-ended coaxial probes, *Meas. Sci. Technol.* 7 (8) (1996) 1164, <http://dx.doi.org/10.1088/0957-0233/7/8/012/meta>.
- [23] M. Wu, X. Yao, L. Zhang, An improved coaxial probe technique for measuring microwave permittivity of thin dielectric materials, *Meas. Sci. Technol.* 11 (11) (2000) 1617, <http://dx.doi.org/10.1088/0957-0233/11/11/311/meta>.
- [24] T.W. Athey, M.A. Stuchly, S.S. Stuchly, Measurement of radio frequency permittivity of biological tissues with an open-ended coaxial line: Part I, *IEEE Trans. Microwave Theory Techn.* 30 (1) (1982) 82–86 <http://ieeexplore.ieee.org/abstract/document/1131021/>.
- [25] M.A. Stuchly, T.W. Athey, G.M. Samaras, G.E. Taylor, Measurement of radio frequency permittivity of biological tissues with an open-ended coaxial line. Part II. Experimental results, *IEEE Trans. Microwave Theory Techn.* 30 (1) (1982) 87–92 <http://ieeexplore.ieee.org/abstract/document/1131022/>.
- [26] I. Marchionni, A. Paffi, M. Pellegrino, M. Liberti, F. Apollonio, R. Abeti, F. Fontana, G. D’Inzeo, M. Mazzanti, Comparison between low-level 50 Hz and 900 MHz electromagnetic stimulation on single channel ionic currents and on firing frequency in dorsal root ganglion isolated neurons, *Biochim. Biophys. Acta (BBA) – Biomembr.* 1758 (5) (2006) 597–605, <http://dx.doi.org/10.1016/j.bbmem.2006.03.014>.
- [27] M. Liberti, F. Apollonio, A. Paffi, M. Pellegrino, G. D’Inzeo, A coplanar-waveguide system for cells exposure during electrophysiological recordings, *IEEE Trans. Microwave Theory Techn.* 52 (11) (2004) 2521–2528, <http://dx.doi.org/10.1109/TMTT.2004.837155>.
- [28] Y. Ning, C. Multari, X. Luo, C. Palego, X. Cheng, J.C.M. Hwang, A. Denzi, C. Merla, F. Apollonio, M. Liberti, Broadband electrical detection of individual biological cells, *IEEE Trans. Microwave Theory Techn.* 62 (9) (2014) 1905–1911, <http://dx.doi.org/10.1109/TMTT.2014.2342660>.
- [29] H. Li, C. Multari, C. Palego, X. Ma, X. Du, Y. Ning, J. Buceta, J.C. Hwang, X. Cheng, Differentiation of live and heat-killed *E. coli* by microwave impedance spectroscopy, *Sens. Actuators B: Chem.* 255 (2018) 1614–1622, <http://dx.doi.org/10.1016/j.snb.2017.08.179>.
- [30] A. Denzi, C. Merla, C. Palego, A. Paffi, Y. Ning, C.R. Multari, X. Cheng, F. Apollonio, J.C.M. Hwang, M. Liberti, Assessment of cytoplasm conductivity by nanosecond pulsed electric fields, *IEEE Trans. Biomed. Eng.* 62 (6) (2015) 1595–1603, <http://dx.doi.org/10.1109/TBME.2015.2399250>.
- [31] K. Grenier, D. Dubuc, T. Chen, F. Artis, T. Chretiennot, M. Pouput, J.-J. Fournié, Recent advances in microwave-based dielectric spectroscopy at the cellular level for cancer investigations, *IEEE Trans. Microwave Theory Techn.* 61 (5) (2013) 2023–2030, <http://dx.doi.org/10.1109/TMTT.2013.2255885>.
- [32] F. Artis, T. Chen, T. Chretiennot, J.-J. Fournié, M. Pouput, D. Dubuc, K. Grenier, Microwaving biological cells: intracellular analysis with microwave dielectric spectroscopy, *IEEE Microwave Mag.* 16 (4) (2015) 87–96, <http://dx.doi.org/10.1109/MMM.2015.2393997>.
- [33] J.C. Booth, N.D. Orloff, X.L. Lu, Y. Wang, E. Rocas, J. Mateu, C. Collado, M. Janezic, Quantitative permittivity measurements of nanoliter fluid volumes from 50 MHz to 40 GHz with microfluidic channels, Conference on Precision Electromagnetic

- Measurements (CPEM), 2010 (2010) 353–354, <http://dx.doi.org/10.1109/CPE.M.2010.5544289>.
- [34] C. Dalmay, m. Cheray, A. Pothier, F. Lalloué, P. Jauberteau, P. Blondy, Ultra sensitive biosensor based on impedance spectroscopy at microwave frequencies for cell scale analysis, *Sens. Actuators A: Phys.* 162 (2) (2010) 189–197, <http://dx.doi.org/10.1016/j.sna.2010.04.023>.
- [35] N. Meyne nee Haase, G. Fuge, H.K. Trieu, A.-P. Zeng, A.F. Jacob, Miniaturized transmission-line sensor for broadband dielectric characterization of biological liquids and cell suspensions, *IEEE Trans. Microwave Theory Techn.* 63 (10) (2015) 3026–3033, <http://dx.doi.org/10.1109/TMTT.2015.2472009>.
- [36] M. Giraud-Carrier, K. Moon, E. Teng, A.R. Hawkins, K.F. Warnick, B.A. Mazzeo, Broadband RF impedance spectroscopy in micromachined microfluidic channels, 2011 Annual International Conference of the IEEE Engineering in Medicine and Biology Society (2011) 4042–4045, <http://dx.doi.org/10.1109/IEMBS.2011.6091004>.
- [37] T. Chen, D. Dubuc, M. Poupot, J.J. Fournier, K. Grenier, Accurate nanoliter liquid characterization up to 40 GHz for biomedical applications: toward noninvasive living cells monitoring, *IEEE Trans. Microwave Theory Techn.* 60 (12) (2012) 4171–4177, <http://dx.doi.org/10.1109/TMTT.2012.2222660>.
- [38] W.J. Ellison, K. Lamkaouchi, J.-M. Moreau, Water: a dielectric reference, *J. Mol. Liq.* 68 (2–3) (1996) 171–279 <http://www.sciencedirect.com/science/article/pii/0167732296009269>.
- [39] W.J. Ellison, Permittivity of pure water, at standard atmospheric pressure, over the frequency range 0–25 THz and the temperature range 0–100 °C, *J. Phys. Chem. Ref. Data* 36 (1) (2007) 1–18, <http://dx.doi.org/10.1063/1.2360986>.
- [40] J.-P. Ryckaert, G. Ciccotti, H.J. Berendsen, Numerical integration of the Cartesian equations of motion of a system with constraints: molecular dynamics of n-alkanes, *J. Comput. Phys.* 23 (3) (1977) 327–341.
- [41] H.G. Petersen, Accuracy and efficiency of the particle mesh Ewald method, *J. Chem. Phys.* 103 (9) (1995) 3668–3679.
- [42] J.C. Phillips, R. Braun, W. Wang, J. Gumbart, E. Tajkhorshid, E. Villa, C. Chipot, R.D. Skeel, L. Kalé, K.A.T. Schulten, Scalable molecular dynamics with NAMD, *J. Comput. Chem.* 26 (16) (2005) 1781–1802.
- [43] E. Neria, S. Fischer, M. Karplus, Simulation of activation free energies in molecular systems, *J. Chem. Phys.* 105 (5) (1996) 1902–1921.
- [44] S. Borech, S. Ringhofer, P. Höchtel, O. Steinhauser, Towards a better description and understanding of biomolecular solvation, *Biophys. Chem.* 78 (1) (1999) 43–68.
- [45] S. Borech, P. Höchtel, O. Steinhauser, Studying the dielectric properties of a protein solution by computer simulation, *J. Phys. Chem. B* 104 (36) (2000) 8743–8752, <http://dx.doi.org/10.1021/jp0008905>.
- [46] V. Raicu, Y. Feldman, *Dielectric Relaxation in Biological Systems: Physical Principles, Methods, and Applications*, Oxford University Press, USA, 2015.
- [47] S.H. Koenig, Brownian motion of an ellipsoid. a correction to Perrin's results, *Biopolymers* 14 (11) (1975) 2421–2423.
- [48] P. Debye, Polar molecules, *J. Soc. Chem. Ind.* 48 (43) (1929) 1036–1037, <http://dx.doi.org/10.1002/jctb.5000484320>.
- [49] C.J.F. Böttcher, P. Bordewijk, The dipole correlation function, in: C.J.F. Böttcher, P. Bordewijk (Eds.), *Dielectrics in Time-dependent Fields*, 2nd ed., Vol. 2 of *Theory of Electric Polarization*, Elsevier, Amsterdam, 1978, pp. 169–284, <http://dx.doi.org/10.1016/B978-0-444-41579-0.50008-2> (Chapter XI).
- [50] Y. Feldman, V. Fedotov, Dielectric relaxation, rotational diffusion and the heat denaturation transition in aqueous solutions of RNASE A, *Chem. Phys. Lett.* 143 (3) (1988) 309–312, [http://dx.doi.org/10.1016/0009-2614\(88\)87386-X](http://dx.doi.org/10.1016/0009-2614(88)87386-X).
- [51] F.M. Richards, Areas, volumes, packing, and protein structure, *Annu. Rev. Biophys. Bioeng.* 6 (1) (1977) 151–176.
- [52] R.B. Marks, A multiline method of network analyzer calibration, *IEEE Trans. Microwave Theory Techn.* 39 (7) (1991) 1205–1215, <http://dx.doi.org/10.1109/22.85388>.
- [53] D.C. DeGroot, J.A. Jargon, R.B. Marks, Multiline TRL revealed, 60th ARFTG Conference Digest, Fall 2002 (2002) 131–155, <http://dx.doi.org/10.1109/ARFTG.2002.1218696>.
- [54] A. Rumiantssev, S.L. Sweeney, P.L. Corson, Comparison of on-wafer multiline TRL and LRM+ calibrations for RF CMOS applications, 2008 72nd ARFTG Microwave Measurement Symposium (2008) 132–136, <http://dx.doi.org/10.1109/ARFTG.2008.4804291>.
- [55] J. Roelvink, S. Trabelsi, S.O. Nelson, A planar transmission-line sensor for measuring the microwave permittivity of liquid and semisolid biological materials, *IEEE Trans. Instrum. Meas.* 62 (11) (2013) 2974–2982, <http://dx.doi.org/10.1109/TIM.2013.2265453>.
- [56] J. Roelvink, S. Trabelsi, S. Nelson, Determining complex permittivity from propagation constant measurements with planar transmission lines, *Meas. Sci. Technol.* 24 (10) (2013) 105001, <http://dx.doi.org/10.1088/0957-0233/24/10/105001>.
- [57] C.D. Abeyrathne, D.H. Huynh, T.T. Lee, T.C. Nguyen, B. Nasr, G. Chana, E. Skafidas, GFAP antibody detection using interdigital coplanar waveguide immunosensor, *IEEE Sensors J.* 16 (9) (2016) 2898–2905.
- [58] S. Borech, P. Höchtel, O. Steinhauser, Studying the dielectric properties of a protein solution by computer simulation, *J. Phys. Chem. B* 104 (36) (2000) 8743–8752.
- [59] S. Borech, M. Willensdorfer, O. Steinhauser, A molecular dynamics study of the dielectric properties of aqueous solutions of alanine and alanine dipeptide, *J. Chem. Phys.* 120 (7) (2004) 3333, <http://dx.doi.org/10.1063/1.1640996>.
- [60] A.T. Ayoub, M. Klobukowski, J. Tuszyński, Similarity-based virtual screening for microtubule stabilizers reveals novel antimitotic scaffold, *J. Mol. Graph. Modell.* 44 (2013) 188–196.

Dr. Daniel Havelka received the M.Sc. and Ph.D. degrees in Electrical engineering from the Czech Technical University in Prague, in 2010 and 2014, respectively. Since 2008, he has been member of the Bioelectrodynamics research team at the Institute of Photonics and Electronics, Czech Academy of Sciences, in Prague where he has been involved in design and development of computational models of microtubule vibration dynamics and electro-dynamics. Now he is focused on dielectric spectroscopy of micro-volume liquid samples.

Ondrej Krivosudský graduated from Czech Technical University in Prague in 2014, Czechia. Currently he is working toward his Ph.D. in Radioelectronics at the Faculty of Electrical Engineering, Czech Technical University in Prague, Czechia. His research interests involve the development of microwave micro-/nanosensors for sensing of electromagnetic properties of biosystems.

Jiří Průša is a Ph.D. student at the University of Chemistry and Technology Prague. He obtained his M.Sc. (2015) in Analytical Chemistry from same university. Since 2015, he is with the Bioelectrodynamics research team of the Institute of Photonics and Electronics, Czech Academy of Sciences. His main research interests are in methods of computer simulation of molecular systems.

Dr. Michal Cifra is head of Bioelectrodynamics research team (Institute of Photonics and Electronics, Czech Academy of Sciences). He obtained M.Sc. (2006) in Biomedical Engineering (University of Žilina, Slovakia) and Ph.D. (2009) in Radioelectronics (Czech Technical University in Prague, Czechia). Apart from ~1 year biophotonics research experience from Germany (RWTH, Aachen / IIB, Neuss), he also gained experience with high frequency bioelectronic interfaces (8 months, University of Chicago, USA). His research interests are in advanced high-frequency and microwave biochips, micro-/nanosensors and nanoscale and molecular electrodynamic phenomena in biosystems.

B | SUPPLEMENTARY DATA OF SECTION 4

This chapter include the supplementary data of Section 4.

Supplementary information for
Microwave absorption by nanoresonator
vibrations tuned with surface modification

Ondrej Krivosudský and Michal Cifra*

Institute of Photonics and Electronics, The Czech Academy of Sciences, Prague, Czechia

E-mail: cifra@ufe.cz

Phone: +420 266 773 454. Fax: +420 284 680 222

Velocity flow with slip condition

The general solution of a velocity field $u(r, t)$ around a nanoresonator (approximated by cylinder) immersed in the no-Newtonian (Maxwellian type) fluid with the standart no-slip condition is in a term of

$$u(r, t) = u(t)g(r) = u(t)C_2K_0\left(r\sqrt{\xi}\right) \quad (1)$$

where $u(t)$ is a velocity of the nanoresonator oscillations, K_0 is modified Bessel function of the second kind zeroth order and r is the radial distance. The last term ξ is equal to $\xi = \omega_r(i - \lambda\omega_r)/\nu$, where ν is a kinematic viscosity of the fluid, ω_r is the angular resonant frequency of the nanoresonator and λ is a relaxation time of the fluid. C_2 represent an integration constant which can be obtained from boundary conditions. We consider axially symmetric incompressible flow of a Maxwellian fluid around nanoresonator, with a linear Navier slip boundary condition applied on the nanoresonator wall. For the purpose of derivation, we assume that flow velocity is constant along entire length of nanoresonator. Slip condition can be then written in the following form:

$$u(R, t) = Ae^{i\omega t} + L_s \left. \frac{\partial u(r, t)}{\partial r} \right|_{r=R} \quad (2)$$

Where the term

$$L_s \left. \frac{\partial u(r, t)}{\partial r} \right|_{r=R} \quad (3)$$

is slip condition defined by Stokes with slip length (L_s). Tangential part of velocity is then no-zero on the surface of a nanoresonator. For the sake of simplicity we assume that the velocity is bound far from the nanoresonator $u(\infty, t) = 0$. By using property of modified Bessel function of the second kind and condition ($r = R$) at the nanoresonator surface

$$\frac{\partial K_0(r)}{\partial r} = -K_1(r) \quad (4)$$

we derive

$$\frac{\partial}{\partial r} K_0 \left(r\sqrt{\xi} \right) \Big|_{r=R} = -\sqrt{\xi} K_1 \left(R\sqrt{\xi} \right) \quad (5)$$

Together with boundary condition from 2, the integration constant C_2 is equal to

$$C_2 = \frac{1}{K_0 \left(R\sqrt{\xi} \right) + L_s \sqrt{\xi} K_1 \left(R\sqrt{\xi} \right)} \quad (6)$$

After substituting integration constant into 1, the axial velocity component $u(r, t)$ with slip condition is

$$u(r, t) = A e^{i\omega t} \frac{K_0 \left(r\sqrt{\xi} \right)}{K_0 \left(R\sqrt{\xi} \right) + L_s \sqrt{\xi} K_1 \left(R\sqrt{\xi} \right)} \quad (7)$$

We can see that if $L_s = 0$ then the velocity equation is the same as for the no-slip boundary condition.

Shear stress calculation

Non-Newtonian liquid behavior was modeled by using the Maxwell model of shear stress, which is relevant for small strains in a following form

$$\tau + \lambda \frac{\partial}{\partial t} \tau = -\mu \dot{\gamma} \quad (8)$$

where τ is a shear stress (i.e. axial force per unit surface) acting on nanoresonator surface, μ is a dynamic viscosity of water, $\dot{\gamma} = \frac{\partial u(r,t)}{\partial r} \Big|_{r=R}$ represents strain rate. In the special case when the relaxation time tends to zero, Eq. 8 reduces to well know linear relationship of Newtonian fluid. By rearranging we get

$$\frac{\partial}{\partial t} \tau + \frac{1}{\lambda} \tau = -\frac{\mu}{\lambda} \dot{\gamma} \quad (9)$$

This linear differential equation of first order could be solved by using integrating factor function in form

$$f(t) = e^{\frac{1}{\lambda} \int dt} = e^{\frac{t}{\lambda}} \quad (10)$$

By multiplying 10 with integrating factor and solving we obtain final form of shear stress as

$$e^{t/\lambda} \tau = - \int \frac{\mu}{\lambda} e^{t'/\lambda} \dot{\gamma}(t') dt' + C \quad (11)$$

with assumption that τ is finite at $t \rightarrow -\infty$

$$\tau = \int_0^t \left\{ \frac{\mu}{\lambda} e^{-(t-t')/\lambda} \right\} \dot{\gamma}(t') dt' \quad (12)$$

In this integral, was evaluated with time after one cycle ($2\pi/\omega_r$).

Scattering width of nanoresonator

Scattering width process can be evaluated (Γ_s) as equal to the inverse of the decay time of radiating dipole. First we express power P_R radiated by an oscillating electric dipole as

$$P_R = \frac{1}{4\pi\epsilon_0} \frac{p^2 \omega_r^4}{3c^3} \quad (13)$$

where c is velocity of electromagnetic wave in the given environment, and $p = qa$ is a dipole moment, which is described in terms of an vibration amplitude a and q is the nanoresonator surface charge involved in the coupling of vibration mode to the electromagnetic radiation.

Then we use the energy of the oscillator as

$$E_o = \frac{1}{2} m \omega_r^2 a^2 \quad (14)$$

where m is effective mass of the system. Scattering process Γ_s could be then described as

$$\Gamma_s = \frac{P_R}{E_o} = \frac{1}{4\pi\epsilon_0} \frac{p^2\omega_r^4}{3c^3} \frac{2}{m\omega_r^2 a^2} = \frac{1}{6} \frac{q^2\omega_r^2}{\pi\epsilon_0 mc^3} \quad (15)$$

where nanoresonator charge is $q = S q_s$ is derived from the effective charge density of the nanoresonator tip based on the surface area of nanoresonator ($S = \pi R^2$).

Microwave absorption by randomly oriented nanoresonators

The problem of microwave absorption of the randomly oriented nanoresonators is equal to problem of electromagnetic power absorbed by randomly oriented oscillating dipoles. For our case, axis of the dipole responsible for microwave absorption is identical with the long axis of the nanoresonator. In spherical coordinates, angular distribution density for random orientation of dipoles is proportional to $\sin\theta$, where θ is a polar angle between electric field vector \vec{E} and dipole moment vector \vec{p} . Furthermore, power absorbed by the dipole is proportional to $(\vec{p}\vec{E})^2$ so that the polar angular dependence is proportional to $\cos^2\theta$. If the $P_{resAligned}$ is power absorbed for resonators aligned in parallel with electric field vector, then we can write for power absorbed by random orientation of dipoles

$$P_{resRandom} = \int_0^{2\pi} d\phi \int_0^\pi P_{resAligned} \cos^2\theta \sin\theta d\theta \cdot \left(\int_0^{2\pi} d\phi \int_0^\pi \sin\theta d\theta \right)^{-1} \quad (16)$$

which could be approximated as $P_{resRandom} = \frac{P_{resAligned}}{3}$.

Microwave absorption by water

We assume plane electromagnetic wave with the direction of propagation perpendicular to the water film. Power absorbed by water film can be approximated as

$$P_{water} = P_0(1 - e^{-2\alpha z}) \quad (17)$$

where P_0 is incident power entering the water film of thickness z with attenuation coefficient of water environment α calculated as

$$\alpha(\omega) = \omega \sqrt{\left[\frac{\varepsilon' \mu}{2} \left(-1 + \sqrt{1 + \frac{\sigma_{ef}^2}{\omega^2 \varepsilon'^2}} \right) \right]} \quad (18)$$

where ε' is a real part of complex permittivity, and μ is the permeability of water. From a macroscopic point of view it is not possible for us to practically distinguish individual contributions to losses (dielectric, conductive) at the constant frequency. Therefore, we use an effective conductivity (σ_{ef}) which includes all conductivity losses:

$$\sigma_{ef} = \text{tg}(\delta) \omega \varepsilon'_r \quad (19)$$

with tangential loss factor $\text{tg}(\delta)$ defined as

$$\text{tg}(\delta) = \frac{\varepsilon''_r}{\varepsilon'_r} \quad (20)$$

where imaginary part of a relative complex permittivity $\varepsilon''_r(\omega)$ and real part of relative complex permittivity $\varepsilon'_r(\omega)$ of water were obtained from Debye model of a complex permittivity

$$\varepsilon^*(\omega) = \varepsilon'_r - j\varepsilon''_r = \varepsilon_\infty + \frac{\varepsilon_s - \varepsilon_\infty}{1 + j\omega\tau} \quad (21)$$

where $\varepsilon_\infty = 4.5$ is permittivity at near infrared wavelengths and $\varepsilon_s = 80$ is the static permittivity with relaxation time of water $\tau = 9.5$ ps. Total power absorbed in a sample given as power ratio of absorption of nanoresonators P_{res} was normalized to power absorbed in water film P_{water} using logarithmic scale as

$$P_{absorbed} = 10 \log_{10} \left(\frac{P_{water} + P_{res}}{P_{water}} \right) \quad (22)$$

C | SUPPLEMENTARY DATA OF SECTION 5

This chapter include the supplementary data of Section 5.

Supplementary information to: Resolving controversy of unusually high refractive index of tubulin

O. KRIVOSUDSKÝ, P. DRÁBER, M. CIFRA

March 1, 2017

1. REFRACTIVE INDEX INCREMENT

To reflect the precision of our measurement and to compare the dn/dc from theoretical predictions with experimental results, we also calculated and measured dn/dc of basic amino acids (L - tryptophan, L - cysteine, L - histidine and L - phenylalanine), result shown in Tab. 1.

Amino acid	M_a [g/mol]	R_a [Ref. per gram]	\bar{v}_p [ml/g]	Calculated dn/dc [ml/g]	Calculated \mp dn/dc [ml/g]	Experimental dn/dc [ml/g]
Tryptophan	204.23	0.297	0.74	0.277	0.276	0.256
Cysteine	121.15	0.238	0.63	0.206	0.205	0.183
Histidine	155.16	0.253	0.67	0.219	0.217	0.204
Phenylalanine	165.18	0.287	0.77	0.244	0.249	0.205

*Tab. 1: Predicted theoretical and experimental data of amino-acids. Data were calculated and measured at 589.3 nm wavelength at 25 °C. M_a - Molecular mass of amino-acid, R_a - refraction per gram of individual amino acid, amino acid specific volume \bar{v}_p . * Data were predicted at 589 nm for hypothetical polypeptide in water with 150 mM NaCl. \mp Data were calculated at 589 nm for amino acid buffer solution.*

Results indicate that amino acid dn/dc are independent on concentration. A least-square fit linear regression yields straight lines, and dn/dc did not deviate significantly from established theoretical values presented in Tab. 1.

2. THEORY & PH-CHARGE EFFECT ADDITIONAL INFORMATION

We calculated refractive index increment (dn/dc) and refractive index (n) of the tubulin isotypes as well as of the bovine serum albumin (BSA) (see Tab. 2 and Tab. 3).

At the physiological pH 7.2 the tubulin has typically highly negatively charged C-terminus tail and is overall negatively charged. Tubulin becomes neutral at pH 5.6.. We are aware that tubulin in buffer with pH 7 is negatively charged and surrounded by cations (magnesium and potassium (from

<i>Theory</i>					
Isotype	Gene name	ID	Length	dn/dc	n
		UniPortKB	(amino acids)	[g/ml]	[-]
$\alpha 1A$	<i>TUBA1A</i>	P02550	451	0.1872	1.6056
$\alpha 1B$	<i>TUBA1B</i>	Q2XVP4	451	0.1871	1.6054
$\alpha 4A$	<i>TUBA4B</i>	F2Z5S8	448	0.1873	1.6067
$\alpha 8$	<i>TUBA8</i>	I3LDR2	399	0.1868	1.6055
βI	<i>TUBB</i>	Q767L7	444	0.1877	1.6078
βII	<i>TUBB2B</i>	F2Z5B2	445	0.1878	1.6094
βIII	<i>TUBB3</i>	F1S6M7	450	0.1877	1.6089
βIVa	<i>TUBB4A</i>	F2Z5K5	444	0.1874	1.6080
βIVb	<i>TUBB4B</i>	F2Z571	445	0.1875	1.6085
βV	<i>TUBB6</i>	I3LBV1	427	0.1871	1.6073
βVI	<i>TUBB1</i>	A5GFX6	449	0.1872	1.6064

<i>Experiment</i>		
Tubulin		0.218 1.64 \pm 0.02
Serum albumin		0.179 1.59 \pm 0.02

Tab. 2: Overview of *Sus scrofa* tubulin isotypes and BSA. Calculated refractive index of tubulin and Bovine serum albumin based on theoretical model in compare with experimental results. Data were calculated and measured at 589.3 nm wavelength at 25°C.

KOH used to tune the pH)) and that the tubulin also interacts with surrounding water molecules. This could lead to variance of measured tubulin refractive index compared to hypothetical case of tubulin without any cations present. We analyzed tubulin under conditions similar to that *in vivo* (pH around 7) which led to refractive index $n = 1.64$.

The results of the theoretical calculation is also dependent on the model where we obtain amino acid composition from crystallography model or genomic sequence (Tab. 2 and Tab. 3). Our theoretical calculations of refractive index do not contain any explicit dependence on the charge since they are based purely only the amino acid composition. We also predicted tubulin refractive index based on genomic sequence which includes C-terminus.

To estimate magnitude of the effect of pH and hence tubulin charge and consequent electrostatic interactions, we can compare the consistence of our approach in case of tubulin to the case of BSA. Isoelectric point of BSA is around $pI = 5$ to 5.60 which is similar to pI of tubulin. All our experiments were performed at pH 7 because we wanted to be close to physiological pH. Refractive index of BSA in experiments was evaluated as $n_{BSA} = 1.59$ while our theoretical value yielded $n_{BSA} = 1.60$. Theoretical values are thus in good agreement with experiment hence we have reason to believe that

Theory

			Length (amino acids)	dn/dc [g/ml]	n [-]
Protein	α - tubulin chain				
ID RSCB protein database	1TUB : A	GI:3745821	440	0.1892	1.6059
Protein	β - tubulin chain				
ID RSCB protein database	1TUB : B	GI:3745822	427	0.1901	1.6087
Protein	Bovine serum albumin chains A,B				
ID RSCB protein database	4F5S : A,B	P02769	583	0.1876	1.6038

Experiment

Tubulin				0.218	1.64 ± 0.02
Serum albumin				0.179	1.59 ± 0.02

Tab. 3: Overview of *Sus scrofa tubulin* isotypes. Calculated refractive index of tubulin based on theoretical model in compare with experimental results. Data were calculated and measured at 589.3 nm wavelength at 25°C.

the effect of pH is rather negligible and may slightly affect only second decimal place of refractive index value.

3. METHODS

Tubulin was purchased from Cytoskeleton, Inc. (Tubulin > 99% pure, Cat.# T238P). It was dissolved and stored at 10 mg/ml concentration in buffer containing 80 mM PIPES pH 6.9, 2.0 mM MgCl₂, 0.5 mM EGTA and 1 mM GTP (G-PEM). L-tryptophan, L-cysteine, L-histidine, L-phenylalanine were supplied by P-lab, CZ. 1,4-Piperazinediethanesulfonic acid (PIPES, CAS 5625-37-6), Guanosine 5'-triphosphate sodium salt hydrate (GTP, CAS 36051-31-7), L-Asparagine, and Glycol ether diamine tetraacetic acid (EGTA, CAS 67-42-5) were purchased from Sigma. Magnesium chloride (MgCl₂, CAS 7791-18-6), Potassium hydroxide (KOH, CAS 1310-58-3) were supplied by PENTA. The proof of polymerization of tubulin to MT is provided by absorbance measurement at 350 nm - a standard method to assess polymerization. Additionally, we also quantified the amount of polymerized vs. unpolymerized tubulin.

3.1. TUBULIN POLYMERIZATION

We followed taxol facilitated tubulin polymerization protocol of Mitchison lab, with small modifications, as follows:

Tubulin (2 mg/ml) was polymerized in BRB 80 buffer (80 mM PIPES pH 6.9, 2.0 mM MgCl₂, 0.5 mM EGTA and 1 mM GTP (G-PEM)) with adding Taxol stepwise at 2, 20 and 200 μ M steps at 37°C.

- add 1/10 volume of 2 μ M taxol added (the final taxol concentration is 0.2 μ M); Incubated at 37°C for 5' minutes.
- 1/10 volume of 20 μ M taxol added (the final taxol concentration is 2 μ M); Incubated at 37°C for 5' minutes.
- 1/10 volume of 200 μ M taxol added (the final taxol concentration is 20 μ M); Incubate at 37°C for 50' minutes.

Refractive index right was measured right after this treatment just leaving sufficient time (few minutes) for the sample to assume the room temperature.

3.2. SPECTROPHOTOMETRY - TUBULIN POLYMERIZATION

The ability of tubulin to polymerize into microtubules was followed by observing an increase of optical density of a tubulin solution at OD₃₅₀ (see Figure 1) under experimental conditions defined above.

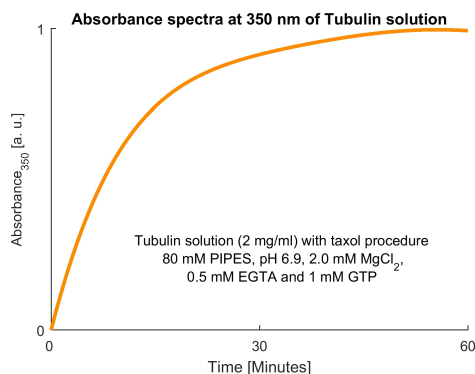


Fig. 1: Polymerization curve of tubulin solution determined by absorbance at 350 nm by Varian UV-VIS 4000 spectrometer at 37°C.

3.3. SPECTROPHOTOMETRY - PROTEIN CONCENTRATION

To reveal how much of the tubulin is unpolymerized once steady state was reached in the spectrophotometer, we removed an aliquot from sample (to determine total tubulin concentration, C_T). Then sample was centrifuged, 20,000 g for 15 min. Aliquot of supernatant was removed and soluble

dimer concentration was derived (C_D). The concentration of the polymer (C_p) was calculated, since $C_T = C_p + C_D$. The protein concentration was determined from following equation:

$$C = (A_{280} \times \text{mol.wt.}) / (\varepsilon_{280} \times l) \quad (1)$$

where A_{280} is absorbance at 280 nm after baseline correction, *mol.wt* is molar weight (110 kDa as molecular weight of tubulin was used), ε_{280} as a extinction coefficient of 1:TUB tubulin ($94660 \text{ M}^{-1} \text{ cm}^{-1}$) and pathlength $l = 1 \text{ mm}$ (Nanophotometer Pearl). Extinction coefficient was calculated with WxPASy ProtParam tool, assuming all pairs of cysteine residues are reduced.

We also performed correction for light scattering by multiplying the absorbance at 330 nm by 1.929 to get the light scattering contribution at 280 nm. Then subtracted the resulting values as measured at these wavelengths. This method assumes that the light scattering contribution varies as the inverse fourth power of the wavelength. Using this methods, we found that 0.14 mg/ml, *i.e.* only around 7%, of tubulin was unpolymerized in our microtubule sample.

4. SPECIFICATIONS OF DSR REFRACTOMETER

Refractive index

- Scale: 1.32- 1.70 nD at 589 nm.
- Accuracy 0.00005 at 25 °C for liquid samples.

Temperature control:

- Active temperature control: solid state Peltier - thermostabilization of the sample compartment.
- Operational temperature: +18 °C to +30 °C.
- Temperature control stability: ± 0.01 °C.
- Temperature measuring accuracy: ± 0.1 °C.

Optics and Hardware:

- Prism: Sapphire crystal.
- Measured wavelengths: 511.3, 589.3, 595.6, 623.4, 671.0, 770.0, 820.0, 880.0, 922.2 nm.
- Wavelength accuracy: ± 2 nm.

D | SUPPLEMENTARY DATA OF SECTION 6

This chapter include the supplementary data of Section 6.

Supplementary information for: On-chip microwave sensing of tubulin polymerization

Ondrej Krivosudský^a, Daniel Havelka^a, Djamel Eddine Chafai, Michal Cifra^b

Institute of Photonics and Electronics of the Czech Academy of Sciences, Prague, 18200, Czechia

^a*The authors contribute equally*

^b*Corresponding author, cifra@ufe.cz*

1. Temperature monitoring

2 We monitored temperature and humidity close to the specimen with Data
3 Logger (CEM DT-171) during both experiments. Mean temperature was
4 maintained around 23.1 °C in first set of experiments with relative humidity
5 around 37%. In the second set of experiments, similar values with tempera-
6 ture around 23.3 °C and 37% of relative humidity were accomplished.

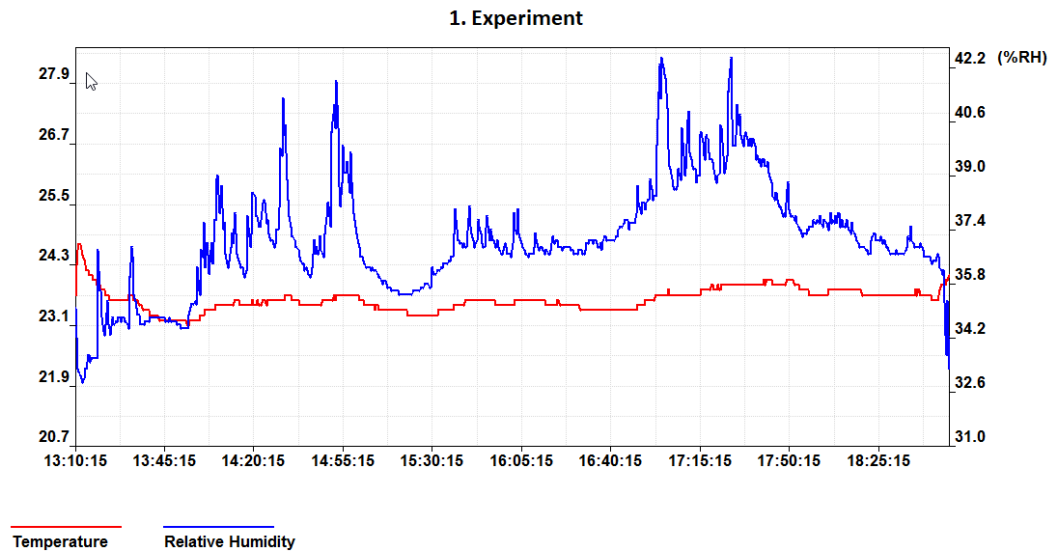


Figure S1: Temperature (red curve) and Relative humidity (blue curve) monitored in first experiment with Data Logger near to the specimen. Data were monitor during the whole measurement. The position of the thermometer was placed close to the chip (see Fig. 1 in the main text).

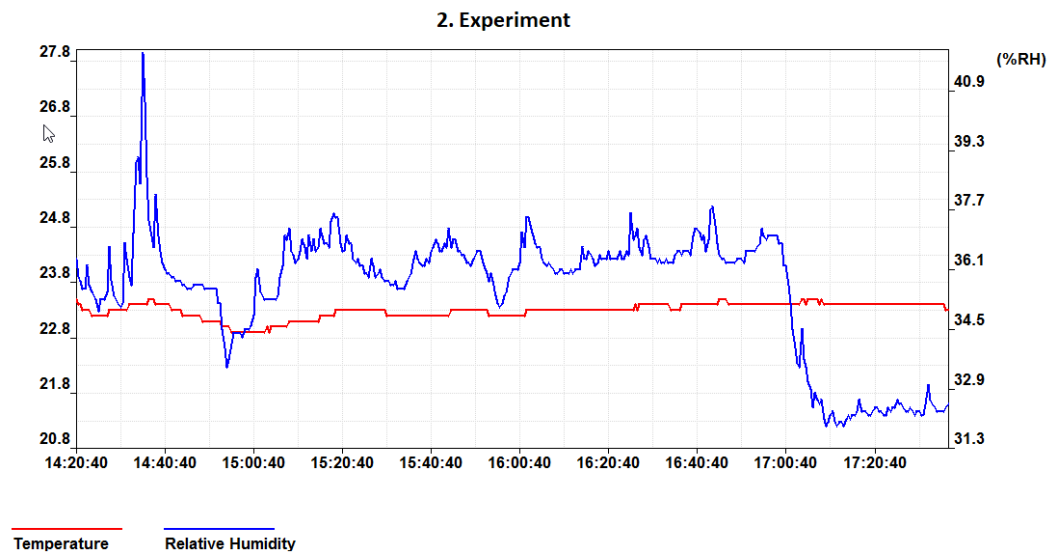


Figure S2: Temperature (red curve) and Relative humidity (blue curve) monitored in second experiment with Data Logger near to the specimen. Data were monitor during the whole measurement. The position of the thermometer was placed close to the chip (see Fig. 1 in the main text).

7 2. Material extraction

8 Data presented in this section are extracted value of complex permit-
9 tivity of quartz glass which was used as a wafer, surface impedance of the
10 metallization and dielectric spectra of the PDMS polymer.

11 2.1. Complex permittivity of quartz glass

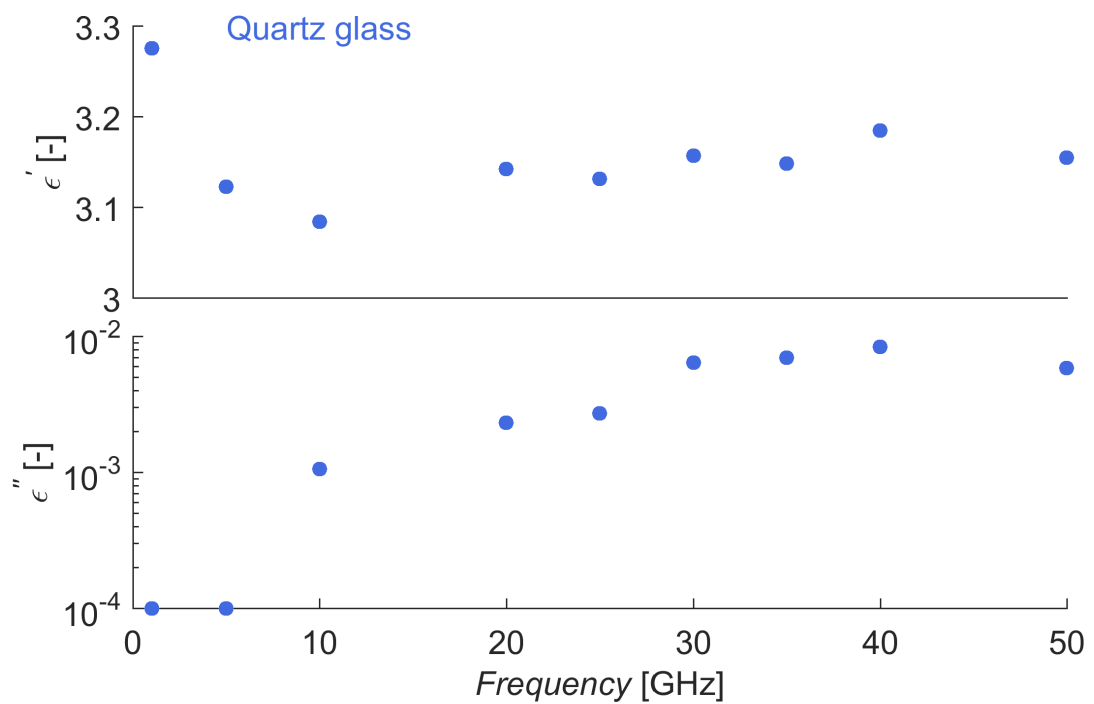


Figure S3: Real (Top) and Imaginary (Bottom) part of extracted complex permittivity of Quartz glass. Raw data obtained from CST Microwave Studio.

12 2.2. Surface impedance of metallization

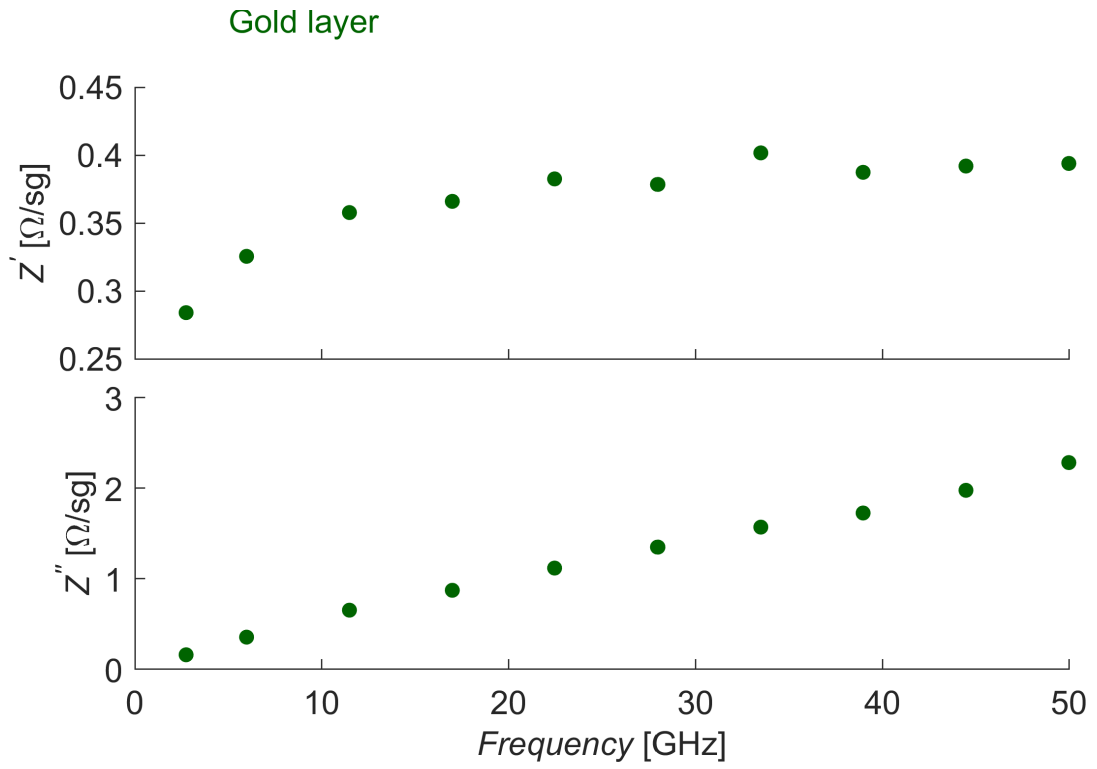


Figure S4: Real (Top) and Imaginary (Bottom) part of extracted surface impedance of 300 nm gold layer. Raw data obtained from CST Microwave Studio.

13 2.3. Complex permittivity of PDMS

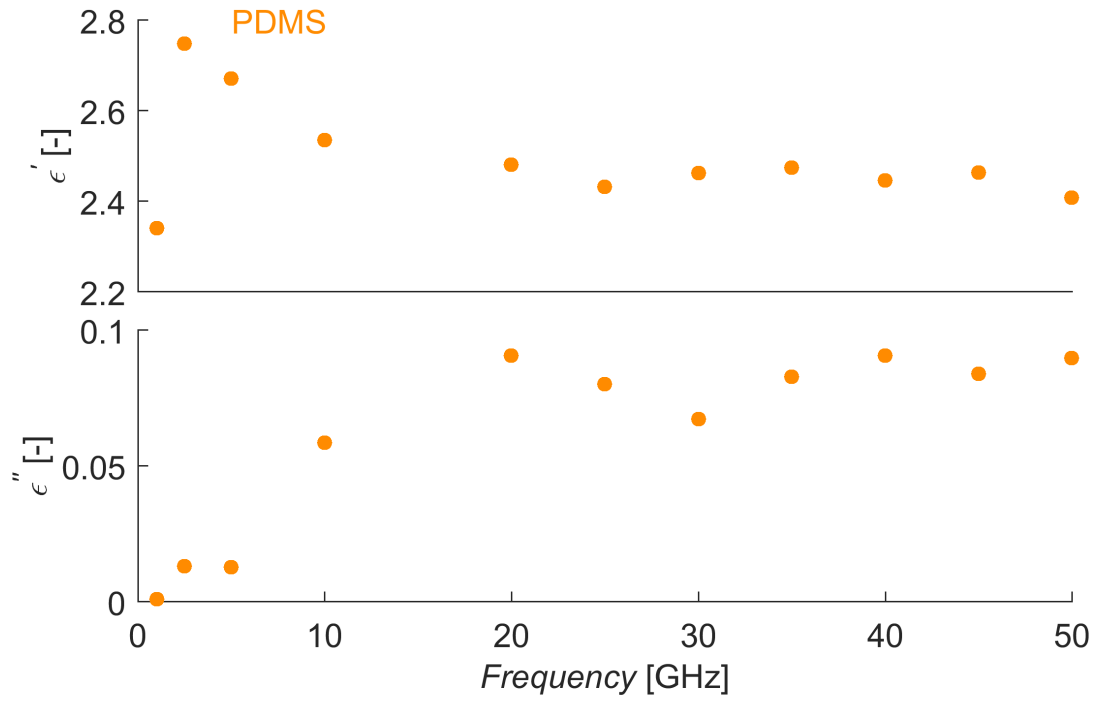


Figure S5: Real (Top) and Imaginary (Bottom) part of extracted complex permittivity of PDMS. Raw data obtained from CST Microwave Studio.

14 3. Calibration verification

15 Average least square error (ALSE) was calculated to assess distance agree-
16 ment between simulated and measured S-parameters quantitatively:

$$\text{ALSE} = \frac{1}{N^2} \sum_{i=1}^N \sum_{j=1}^N |S_{ij}^{\text{SIMULATED}} - S_{ij}^{\text{MEASURED}}|^2 \quad (1)$$

17 Note that equation employs linear scale while in the Fig. S6 ALSE is de-
18 picted in decibels. The ALSE figure demonstrates an excellent agreement
19 between simulated and measured S-parameters up to 40 GHz. Beyond this
20 frequency, the ALSE rises above -70 dB which still presents a good agree-
ment.

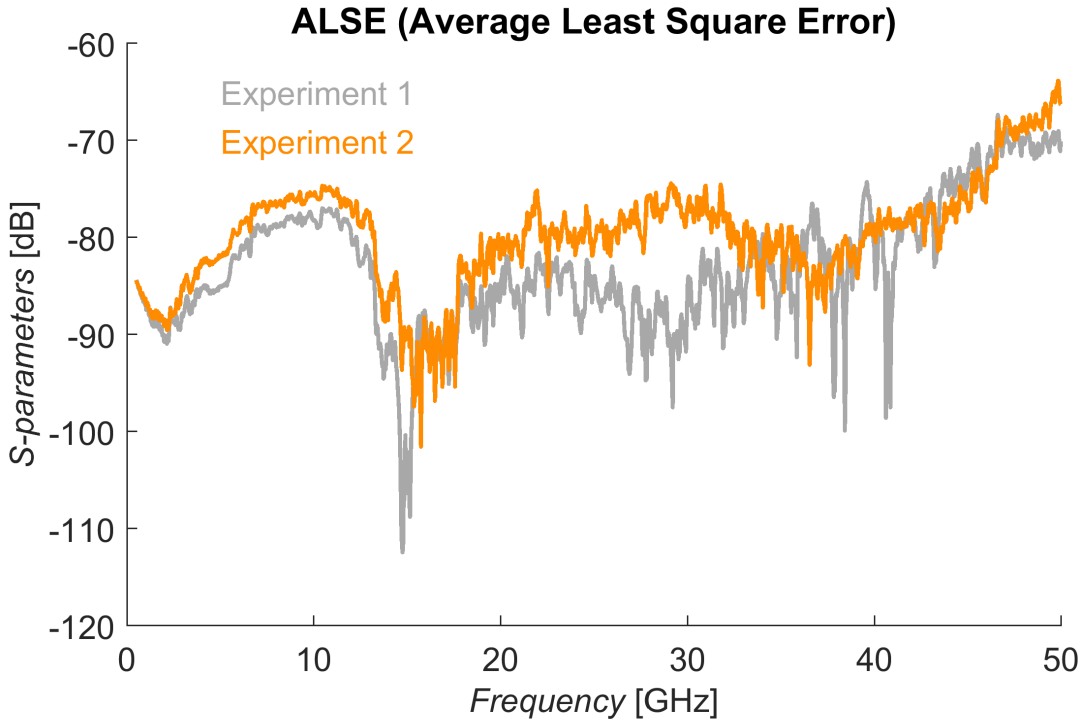


Figure S6: ALSE (Average Least Square Error) between simulated and measured data of dry chip with PDMS microchannel. Experiment 1 is depicted with Grey color, experiment 2 by Orange color.

22 Thru test, result calculated to determine the phase uncertainty are pre-
23 sented in following Fig. S7. Results determine the threshold value for material
24 extraction.

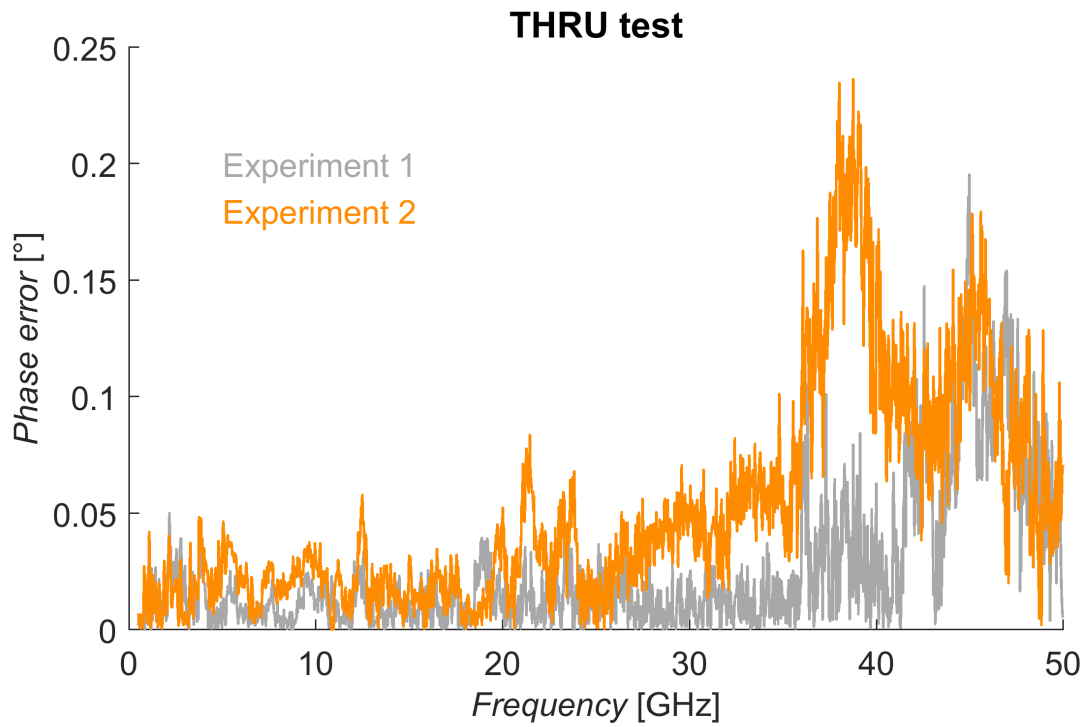


Figure S7: Thru test representing the phase error of the measurement in both experiments. Experiment 1 is depicted with Grey color, Experiment 2 by Orange color.

25 The Thru test figure demonstrates a maximum phase error equal to 0.2°
26 at around 40 GHz, which still represent an excellent robustness of the cali-
27 bration process.

28 **4. Variation of scattering parameters**

29 Reputability of measured S-parameters of our sensor. Measured reflection
30 and transmission coefficients of the sensor loaded with water, buffer, tubulin
31 and microtubule specimen. For each solution 2 independent specimens were
32 prepared and each specimen was measured 8 times to yield 16 S-parameter
33 measurements ($16 \times S_{11}$, $16 \times S_{22}$, $16 \times S_{21}$, and $16 \times S_{12}$).

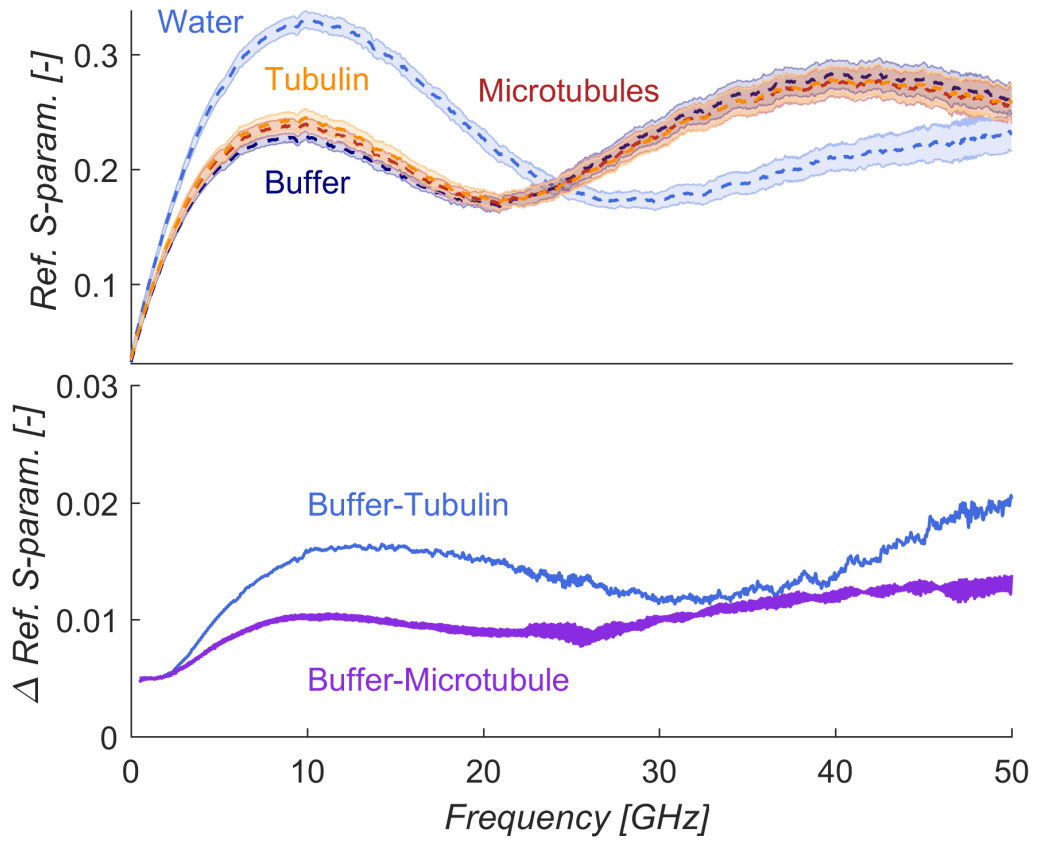


Figure S8: Top image: Average value (dashed line) and standard deviation of reflection was calculated from $16 \times S_{11}$ and $16 \times S_{22}$ (total $N=32$) values. Bottom image: Deviation of mean values between buffer and tubulin (blue), buffer and microtubule (violet).

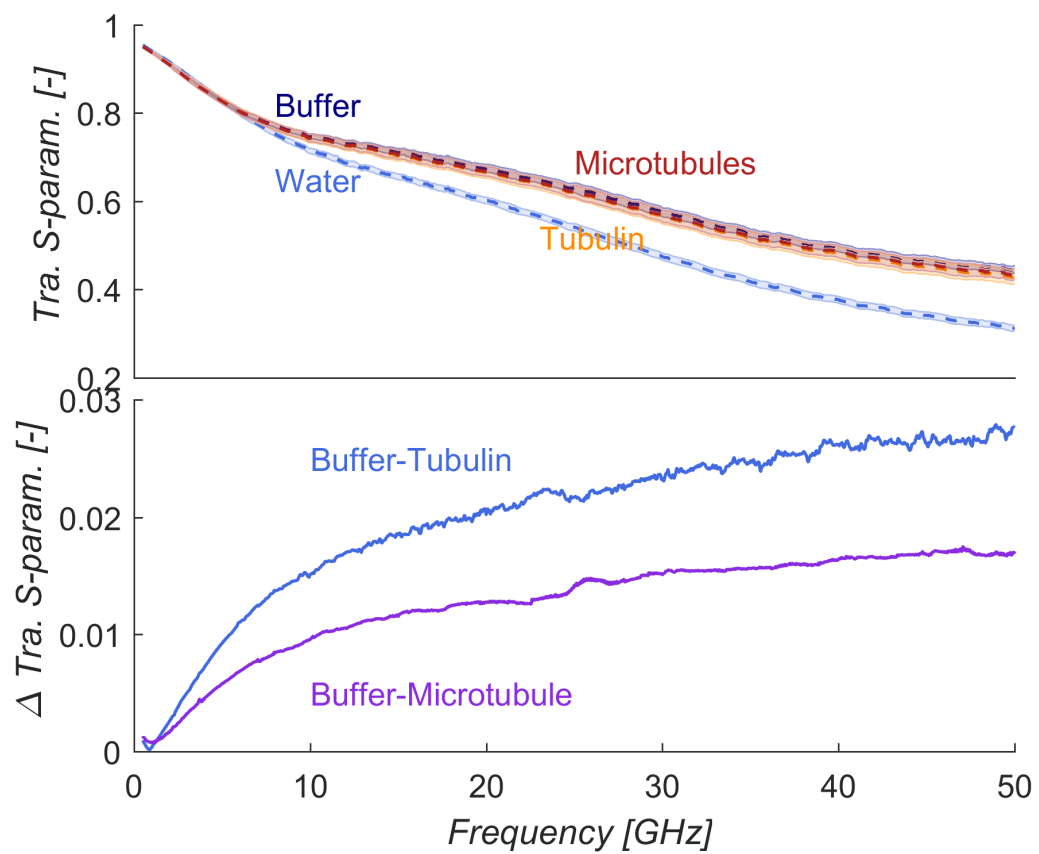


Figure S9: Top image: Average value (dashed line) and standard deviation of transmission was calculated from 16 x S_{12} and 16 x S_{21} (total N=32) values. Bottom image: Difference between mean values of buffer and tubulin (blue), buffer and microtubule (violet).

E | SUPPLEMENTARY DATA OF ARTICLE [A4]

This chapter include the supplementary data of Appendix A.

Supplementary data of the article: "Rational design of sensor for broadband dielectric spectroscopy of biomolecules"

Daniel Havelka, Ondrej Krivosudský, Jiří Průša, Michal Cifra^a

Institute of Photonics and Electronics, The Czech Academy of Sciences, Prague, 18200, Czechia

^acorresponding author, *cifra@ufe.cz*

1. Derivation of equations for analytical model

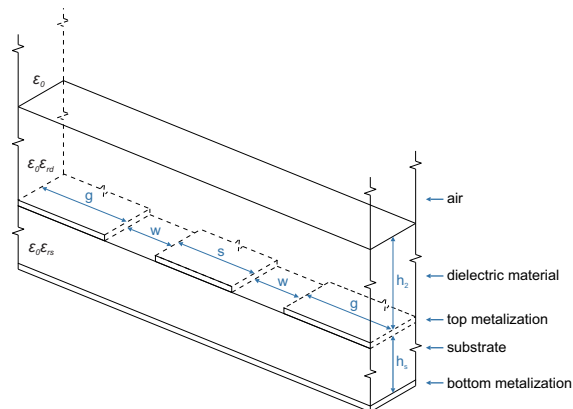


Figure S1: Schematic cross-sectional view of conductor-backed coplanar waveguide (CBCPW) with a top dielectric material.

2 We created a model consisting of two feeding segments of CBCPW with
3 air on the top and one sensing segment between them with permittivity ϵ_{r2}
4 on the top, see Fig. 2 A in the main text. For this we need (i) to derive total
5 capacitance (C_{CBCPW}) and characteristic impedance of a general segment

6 of CBCPW (Z_0), (ii) to calculate ABCD matrix of a general segment of
7 CBCPW, and (iii) to calculate ABCD matrix of three CBCPW segments
8 connected in cascade, convert ABCD matrix to S-parameters matrix, and
9 calculate sensitivity (ξ) to variation of the specimen permittivity.

10 1.1. Capacitance and characteristic impedance of CBCPW

11 Analytical calculation of total capacitance (C_{CBCPW}) and characteris-
12 tic impedance (Z_0) of the segment of CBCPW with a top dielectric mate-
13 rial was derived from models of "Conductor-Backed Coplanar Waveguide"
14 and "Conventional Coplanar Waveguide Sandwiched between Two Dielec-
15 tric Substrates" (Simons (2004), pages: 15, 24-25, and 88). This structure is
16 schematically illustrated in Fig. S1. Moduli of complete elliptic integrals are

$$a = s/2; \quad b = \frac{2w + s}{2}; \quad g \rightarrow \infty \quad (1)$$

17

$$k_0 = a/b; \quad k_2 = \frac{\sinh\left(\frac{\pi a}{2h_d}\right)}{\sinh\left(\frac{\pi b}{2h_d}\right)}; \quad k_3 = \frac{\tanh\left(\frac{\pi a}{2h_s}\right)}{\tanh\left(\frac{\pi b}{2h_s}\right)}; \quad \forall i, \quad k'_i = \sqrt{1 - k_i^2} \quad (2)$$

18 C_{air} is a partial capacitances of the coplanar waveguide in the absence of
19 all the dielectric layers (i.e. as if all dielectric material in the model including
20 substrate was air) and is defined as follows

$$C_{air} = 2\epsilon_0 \left(\frac{K(k_0)}{K(k'_0)} + \frac{K(k_3)}{K(k'_3)} \right) \quad (3)$$

21 where $K(k_0)$ is complete elliptic integral (Abramowitz (1965)) with modulus
22 k_0 . C_1 and C_2 are the partial capacitance of the coplanar waveguide with
23 only lower and upper dielectric layers, respectively, and can be considered
24 connected to C_{air} in parallel to form the total capacitance (C_{CBCPW}):

$$\begin{aligned} C_{CBCPW} &= C_{air} + C_1 + C_2 \\ &= C_{air} + 2\epsilon_0(\epsilon_{rs} - 1) \frac{K(k_3)}{K(k'_3)} + 2\epsilon_0(\epsilon_{rd} - 1) \frac{K(k_2)}{K(k'_2)} \\ &= 2\epsilon_0 \left(\frac{K(k_0)}{K(k'_0)} + \epsilon_{rs} \frac{K(k_3)}{K(k'_3)} + (\epsilon_{rd} - 1) \frac{K(k_2)}{K(k'_2)} \right) \end{aligned} \quad (4)$$

25 next calculation of effective dielectric constant (ϵ_{eff}) follows as

$$\epsilon_{eff} = \frac{C_{CBCPW}}{C_{air}} = \left(1 + \epsilon_{rs} \frac{K(k'_0) K(k_3)}{K(k_0) K(k'_3)} + (\epsilon_{rd} - 1) \frac{K(k'_0) K(k_2)}{K(k_0) K(k'_2)} \right) \left(1 + \frac{K(k'_0) K(k_3)}{K(k_0) K(k'_3)} \right)^{-1} \quad (5)$$

26 and finally we can calculate characteristic impedance (Z_0)

$$Z_0 = \frac{60\pi}{\sqrt{\epsilon_{eff}}} \left(\frac{K(k_0)}{K(k'_0)} + \frac{K(k_3)}{K(k'_3)} \right)^{-1} \quad (6)$$

27 where s , w , h_d , h_s , ϵ_{rd} , and ϵ_{rs} are described in Fig. S1, ϵ_0 is permittivity of
28 vacuum.

29 1.2. ABCD parameters of CBCPW segment

30 It was assumed that characteristic impedance of the transmission line
31 $Z_0 = \sqrt{(R + j\omega L)/(G + j\omega C)}$ has the parasitic resistance (R) and conduc-
32 tance (G) equal to zero. Inductance (L) and propagation constant (γ) is
33 calculated as

$$L = Z_0^2 C_{CBCPW}; \quad (7)$$

$$\gamma = \sqrt{(R + j\omega L)(G + j\omega C_{CBCPW})} = \sqrt{j^2 \omega^2 L C_{CBCPW}} \quad (8)$$

35 then ABCD matrix $[a]$ of the CBCPW segment is defined as

$$[a] = \begin{bmatrix} \cosh(\gamma l) & Z_0 \sinh(\gamma l) \\ \frac{1}{Z_0} \sinh(\gamma l) & \cosh(\gamma l) \end{bmatrix} = \begin{bmatrix} A & B \\ C & D \end{bmatrix} \quad (9)$$

36 where l is length of CBCPW segment.

37 1.3. Sensitivity of the model

38 Next, a model was created from two (feeding) segments of CBCPW with
39 air on the top and one sensing segment between them with a specimen with
40 the permittivity ϵ_{r2} on the top of the sensing segment, see Fig. 2 A in the
41 main text. ABCD matrix of model $[a_t]$ is calculated as

$$[a_t] = [a_1] [a_2] [a_1] = \begin{bmatrix} A_t & B_t \\ C_t & D_t \end{bmatrix} \quad (10)$$

42 where $[a_1]$ is ABCD matrix of feeding segments of CBCPW, $[a_2]$ is ABCD
43 matrix of sensing segment of CBCPW, ϵ_{rd} was set as air in case of $[a_1]$ and

44 as Debye model of water in case of $[a_2]$, see equation (13). Other parameters
 45 used in the section *Capacitance and characteristic impedance of CBCPW*
 46 are the same in case of $[a_1]$ and $[a_2]$. ABCD parameters are converted to
 47 S-parameters as (Visser (2012), Appendix E, page 246, table E.2)

$$S_{11} = \frac{A_t + B_t/Z_1 - C_t Z_1 - D_t}{A_t + B_t/Z_1 + C_t Z_1 + D_t}; \quad S_{21} = \frac{2}{A_t + B_t/Z_1 + C_t Z_1 + D_t} \quad (11)$$

48 where Z_1 is characteristic impedance of (feeding) CBCPW segment calcu-
 49 lated by equation (6), S_{11} and S_{21} are reflection and transmission coefficients
 50 of the model, respectively. Finally, we define the sensitivity as

$$\xi_{21} = \left| \frac{\Delta S_{21}}{\Delta \epsilon_{r2}} \right|; \quad \xi_{11} = \left| \frac{\Delta S_{11}}{\Delta \epsilon_{r2}} \right| \quad (12)$$

51 We used $\Delta \epsilon_{r2} = 5 + j5$.

52 Debye model of water

53 Debye model of water expressed in equation (13) was used for determi-
 54 nation of ϵ_{r2} in Fig. 2 A and for determination of initial values of extracted
 55 permittivity in optimization algorithm.

$$\epsilon_{r2} = \epsilon'_{r2} + j\epsilon''_{r2} = \epsilon(\infty) + \frac{\epsilon(0) - \epsilon(\infty)}{1 - j\omega\tau} - \frac{\sigma}{j\omega\epsilon_0} \quad (13)$$

56 where $\epsilon(\infty)$ is permittivity at high frequency, $\epsilon(0)$ is static (low frequency)
 57 permittivity, ϵ_0 is permittivity of vacuum, j is imaginary unit ($j^2 = -1$), ω is
 58 angular frequency, τ is relaxation time, and σ is DC (direct current) con-
 59 ductivity. Note that throughout the paper we use complex permittivity sign
 60 notation based on electric field harmonic time dependence given by $e^{-j\omega t}$.

61 Drawing of the chip and Beatty line

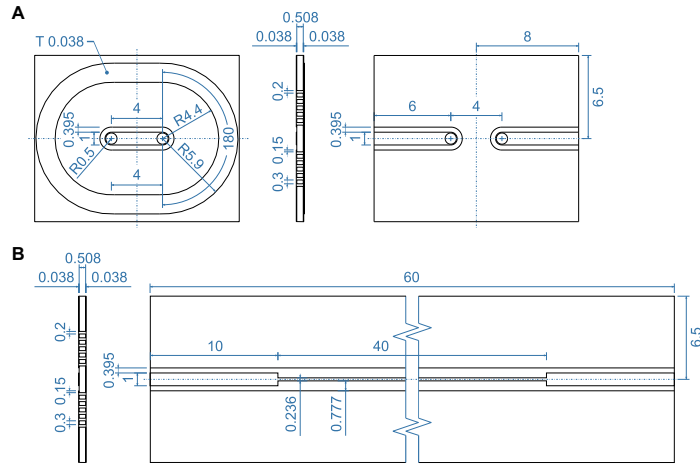


Figure S2: Drawing of our chip and Beatty line. A) Dimensions of our chip and B) Dimensions of Beatty line. Units mm

62 **Verification of the measurement method and the chip**

63 For the measurements, calibration kit and calibration procedure were first
 64 verified with "Beatty line" which is a type of precision mismatch formed by an
 65 impedance discontinuity. The Beatty line was fabricated as a $50\ \Omega$ CBCPW
 66 transmission line with 40 mm long section of $100\ \Omega$ impedance formed by a
 67 thinner central conductor $s = 236\ \mu\text{m}$ and $w = 777\ \mu\text{m}$. This enables evalua-
 68 tion of the calibration accuracy.

69 Transmission and reflection coefficients of this Beatty line are plotted in
 70 the Fig. S3 C. The dashed orange (reflection coefficients) and dashed blue
 71 curves (transmission coefficients) represent data obtained from simulations
 72 in CST Microwave Studio and the measured data (VNA Rohde&Schwarz®
 73 ZVA40) are in solid green (reflection coefficients) and solid red (transmis-
 74 sion coefficients) lines. Results of scattering parameters obtained from the
 75 simulation and measurement with dry chip are plotted in Fig. S3 A. Chip
 76 was tested by the measurement of ultrapure water ($\sigma = 0.05\ \mu\text{S}/\text{cm}$ @22 °C),
 77 250 μL specimen volume was injected by a laboratory micropipette. Trans-
 78 mission coefficients from simulation and measurement of our chip loaded
 79 with a water droplet are plotted in the Fig. S3 B. In CST Microwave Stu-
 80 dio, the water droplet was simulated using Debye model of water. Reflection
 81 coefficients demonstrate appropriate amount of power reflected ($S_{11} = -10$
 82 $\div -3\ \text{dB}$) to probe the permittivity of the water-like specimens. The losses
 83 heavily influence transmission coefficient S_{21} due to water absorption which
 84 causes a dip of S_{21} at around 20 GHz (Ellison (2007)). Average least square
 85 error (ALSE) was calculated to assess distance agreement between simulated
 86 and measured S-parameters quantitatively:

$$\text{ALSE} = \frac{1}{N^2} \sum_{i=1}^N \sum_{j=1}^N |S_{ij}^{\text{SIMULATED}} - S_{ij}^{\text{MEASURED}}|^2 \quad (14)$$

87 Note that equation employs linear scale while in the Fig. S3. D both S-
 88 parameters and ALSE are depicted in decibels. The ALSE figure demon-
 89 strates an excellent agreement between simulated and measured S-parameters
 90 up to 35 GHz. Beyond this frequency, the ALSE rises above -40 dB which
 91 still presents a good agreement.

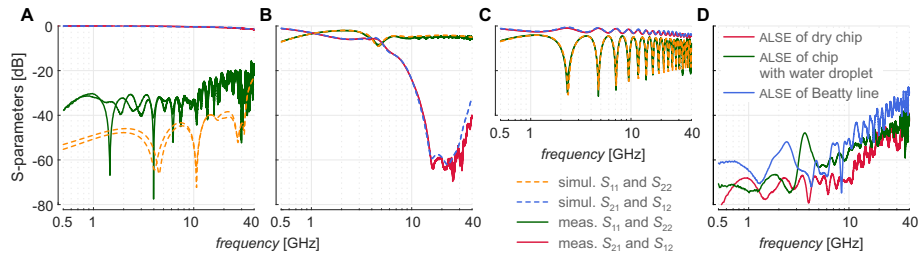


Figure S3: Simulated and measured S-parameters of the chip and independent verification structure are in a very good agreement. Measured (solid lines) and simulated (dashed lines) S-parameters of A) Dry chip. B) Chip with droplet of pure water. C) Beatty line. D) ALSE (Average Least Square Error) between simulated and measured data of dry chip (A), Chip with water droplet (B), and Beatty line (C).

92 Dry chip

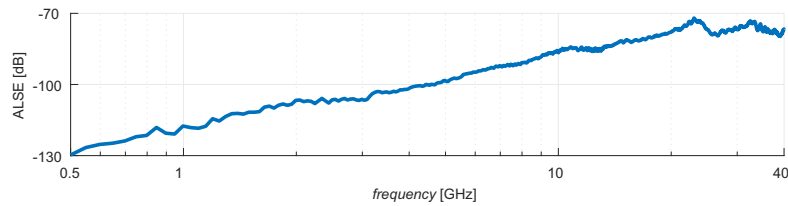


Figure S4: Average least square error (ALSE) was calculated to verify the quality of our cleaning procedure of the chip. Displayed ALSE represents a difference between S-parameters of a dry chip before and after the measurement of 14 amino acid samples (after cleaning). The ALSE is in the range from -100 dB to -70 dB across the measured frequency range. These values are < -60 dB (i.e. < 0.001 in linear scale) which is less than the standard deviation (experimental error) between measurements (see Figure S5 C-E). Therefore we can state that the cleaning procedure is sufficiently effective and any possible traces of samples left on the chip do not influence the subsequent measurements.

93 Reproducibility of S-parameter measurements with our chip

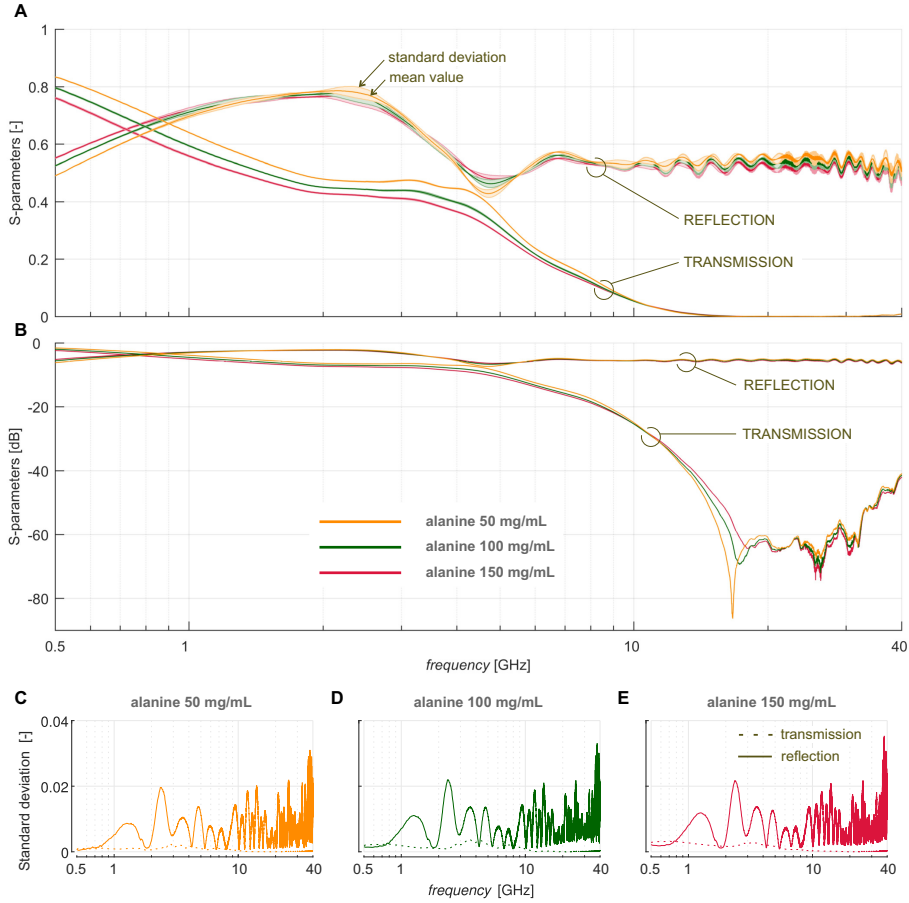


Figure S5: Reproducibility of measured S-parameters of our chip. Measured reflection (S_{11} , S_{22}) and transmission (S_{21} , S_{12}) coefficients of the chip loaded with alanine water solution specimen. For each concentration 3 independent specimens were prepared and each specimen was measured 3 times to yield 9 S-parameter measurements ($9 \times S_{11}$, $9 \times S_{22}$, $9 \times S_{21}$, and $9 \times S_{12}$). Average and standard deviation of reflection was calculated from $9 \times S_{11}$ and $9 \times S_{22}$ (total $N=18$) values. The standard deviation (SD) of transmission was calculated in a similar manner from S_{21} and S_{12} parameters. A) S-parameters of alanine 50, 100, and 150 mg/mL in a linear scale, B) S-parameters of alanine 50, 100, and 150 mg/mL in decibels. Solid thick lines are the calculated average the solid light lines (forming symmetric envelope) are depicting standard deviation data. For clarity, we plot SD data again in separate graphs: C) SD of alanine 50 mg/mL measurements, D) SD of alanine 100 mg/mL measurements, and E) SD of alanine 150 mg/mL measurements. In C), D), and E), the solid line corresponds to reflection SD data and the dashed line to transmission SD data.

94 Data from coaxial probe

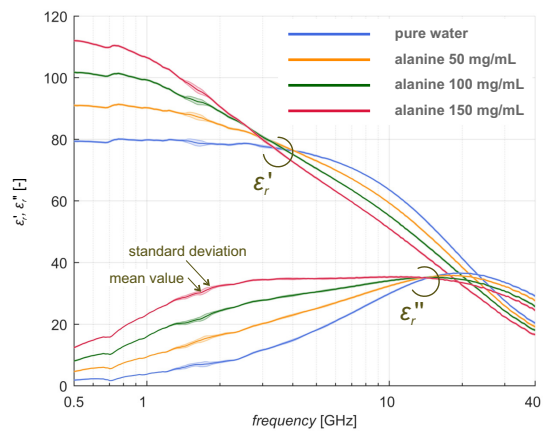


Figure S6: Experimental data obtained from coaxial probe measurement. For each concentration 3 independent specimens were prepared and each specimen was measured 3 times to yield the complex permittivity data.

95 **Contributions to susceptibility obtained from molecular dynamics**
 96 **simulations**

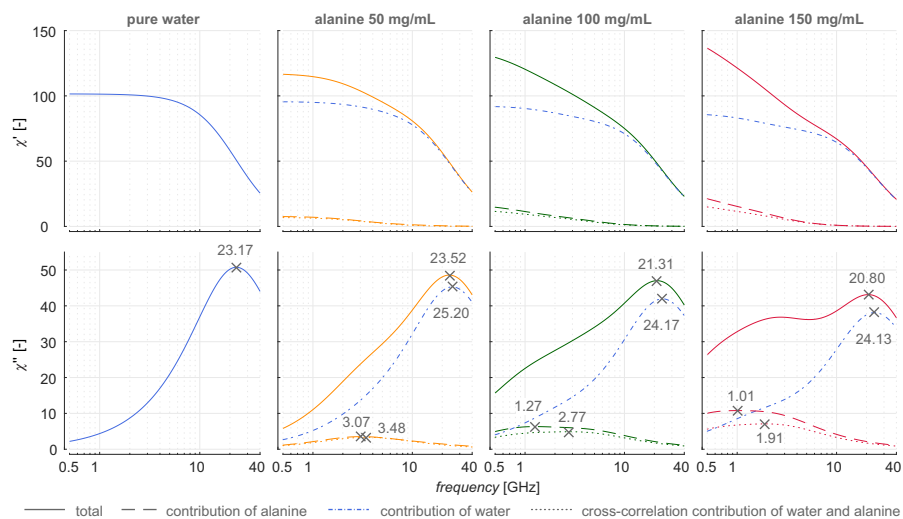


Figure S7: Contributions to susceptibility obtained from molecular dynamics simulations. Numbers denote frequencies of respective peaks. Note that $\chi(\omega) = \chi'(\omega) + j\chi''(\omega) = \epsilon(\omega) - 1$

97 **Fitting of the data obtained from our chip**

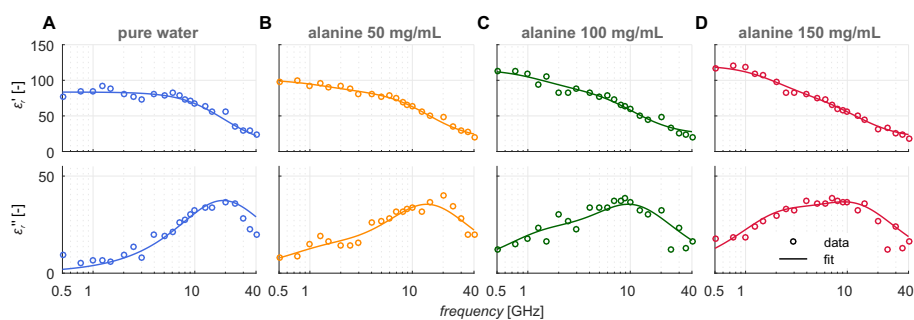


Figure S8: Experimental results obtained from our chip (circles) and their fit (line). The single Debye model was used for fitting of pure water data and the double Debye model was used for fitting of alanine 50 mg/mL, alanine 100 mg/mL, and alanine 150 mg/mL data. Points up to 20 GHz were used as an input to the data fitting. Obtained fitted function was plotted up to 40 GHz.

98 **Fitted data from our chip**

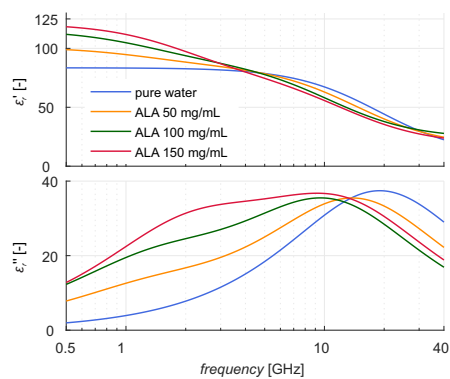


Figure S9: Experimental results from our chip after fitting. Alanine concentration dependent increase of imaginary part of permittivity (ϵ'') at around few GHz is a signature of alanine dipole rotational relaxation

99 **References**

- 100 Abramowitz, M., 1965. I. stegun handbook of mathematical functions. Na-
101 tional Bureau of Standards Applied Mathematics Series 55, 8.
- 102 Ellison, W. J., Mar. 2007. Permittivity of Pure Water, at Standard Atmo-
103 spheric Pressure, over the Frequency Range 0-25THz and the Temperature
104 Range 0-100 C. Journal of Physical and Chemical Reference Data 36 (1),
105 1-18.
106 URL <http://aip.scitation.org/doi/10.1063/1.2360986>
- 107 Simons, R. N., 2004. Coplanar waveguide circuits, components, and systems.
108 Vol. 165. John Wiley & Sons.
- 109 Visser, H. J., 2012. Antenna theory and applications. John Wiley & Sons.

Experience

2017 – 2019

| Intern
CST - Computer Simulation Technology GmbH
CST Branch Office, Prague, Czechia

2014 – 2018

| Ph.D. student
Institute of Photonics and Electronics
of the Czech Academy of Sciences
Prague, Czechia

Education

2014 – present

| Ph.D. in Radioelectronics
Czech Technical University in Prague
Prague, Czechia

2012 – 2014

| MSc. in Biomedical Engineering
Czech Technical University in Prague
Prague, Czechia

2008 – 2012

| BSc. in Physical Engineering
Czech Technical University in Prague
Prague, Czechia

Technical Skills

RF/Microwave engineering

| Dielectric measurement methods
| High-frequency measurements with VNA

Software skills

| Programming in MATLAB

Microfabrication

| Knowledge of photolithography methods
| Familiarity with thin-film deposition
| Hands-on experience in metrology techniques

Training

2018

cfaed Summer School

| Dresden Microelectronic Academy

2017

VNA Measurement Training

| CST Studio Suite, CST branch office, Czechia

2016

Microwave and Radio-frequency Training

| CST Studio Suite, CST branch office, Czechia

2015

Course of transmission electron microscopy in life sciences

| Institute of Molecular Genetics, CAS

Achievements

2015

| Conference Scholarship
Foundation of Josefa, Marie and Zdeňky Hlávkových

2014

| Dean's Prize for the outstanding diploma thesis

2014

| IEEE association prize for the outstanding diploma thesis (MTT/AP/ED/EMC chapter)

In Prague, 28. January 2019

.....
ING. ONDREJ KRIVOSUDSKÝ



AŽ DOSLOUŽÍM, CHCI DO SBĚRU!